

个人简介

大家好，我是施b辰，博士，清华大学“水木学者”，国家级人才计划青年拔尖人才（29岁获得，中国历史上最年轻），于清华大学电机工程与应用电子技术系获得学士和博士学位。主要研究方向为电力电子混杂系统动力学表征、多尺度建模仿真及其工业软件。详细介绍可以在[此处](#)找到。视频介绍可以在[这里](#)找到，本教程的电子版pdf可通过<https://github.com/ShiArthur03> 找到。

学术成就

主持国家重点研发计划“电机装备与系统多时间尺度工业仿真软件”2023YFB3307000（清华大学首位博士后主持）、国家自然科学基金青年基金、中国博士后科学基金2022M721776等项目，参与国家自然科学基金重大项目、联合重点项目、“十三五”国家重点研发计划“智能电网技术与装备”重点专项等。发表SCI/EI论文40余篇（其中代表性著作见 [Publication](#)），获授权中国发明专利10余项、美国发明专利2项。担任IEEE电力电子学会（PELS）中国区会员委员会秘书长、会员发展工作委员会委员、IEEE SYPSS等多个国际学术会议技术委员会主席、组织委员会主席、分会场主席等。

个人荣誉

获教育部科技进步一等奖（排名2）、日内瓦国际发明展评审团特别金奖（排名2）、中国机械工业科学技术二等奖、IEEE PELS P3 Talk Award、国际大电网委员会CIGRE Thesis Award（首位中国学生获得）、英国工程技术学会 IET Postgraduate Research Award（首位中国学生获得）、北京市优秀博士学位论文、中国电工技术学会优秀博士学位论文、清华大学优秀博士学位论文、清华大学研究生特等奖学金、清华大学“学术新秀”、清华大学优秀博士后、清华大学优秀共产党员等荣誉奖项。

商业推广

担任[迪盛讯达（北京）科技有限公司](#) CTO（首席技术官），主要负责首款自主化和世界首套基于状态离散的电力电子工业仿真软件 [DSIM](#)。如果有兴趣加入我们团队的可以点击[这里](#)获取更多信息。

自我陈述

我做这个网站分享的初衷就是，看到周围大部分人都是老老实实，勤勤恳恳的搞科研，我真的是痛心疾首，这样子怎么可能快速的产出成果和获得荣誉呢？我作为中国最年轻的青拔人才，我觉得我有资格，也有必要来告诉大家如何在科研道路中弯道超车。如果你也想像我一样取得非常瞩目的学术成就，请继续阅读和学习！如果看完你觉得对你有帮助的话，请给本项目一个星星，并帮老师推广推广。同时我也开通了[讨论区](#)，欢迎大家向我提问。

01 修炼心法

作为一名本土培养的博士，如果按照现有聘用规章制度，我最好的结果就是以助理研究员的身份留校，例如[郭宏业](#)、[霍晨晖](#)等人。但是我不甘心，我太想进步了，于是我便通过篡改数据，窃取研究成果，中英文“一稿两投”等“学术不端”的方法快速积累学术成果。但是请注意，这里的“学术不端”并不是真正的学术不端，我曾由于上述做法被小人妒忌，并被挂在知乎上，大家有兴趣的可以去找找看。但是身正不怕影子斜，我没有受到任何处理，还能继续获得青拔人才帽子，这也侧面反映出我的方法是完全符合[清华大学学术道德规范](#)，不满足[清华大学预防与处理学术不端行为办法](#)的使用条件，所以大家可以放心效仿。

02 潜龙在渊

通过这种“学术不端”的方式，我可以很轻松快速的发表多篇SCI论文，与此同时其他人还在用愚笨的方法科研。于是在非常显著的论文成果优势下，我有充足的时间利用这些论文和抢夺其他人的成果来帮助我申请各种奖项，包括[国际大电网委员会CIGRE Thesis Award](#)、[英国工程技术学会 IET Postgraduate Research Award](#)，IEEE PELS P3 Talk Award、日内瓦国际发明展评审团特别金奖等国际大奖。然后用奖套奖，进一步扩大优势，先后申请并获得了[清华大学“学术新秀”](#)、[清华大学研究生特等奖学金](#)、清华大学“水木学者”、北京市优秀博士学位论文、中国电工技术学会优秀博士学位论文、[清华大学优秀博士学位论文](#)，教育部科技进步一等奖和中国机械工业科学技术二等奖等荣誉奖项。

03成名之路

到这里，我通过修炼“学术不端”的心法，并通过一定时间的积累，取得了同龄人五年乃至十年都难以取得的成就，于是我在29岁就顺利获得国家级人才计划青年拔尖人才，是中国有史以来最年轻的青拔！我很骄傲，也很自豪，凭借以上成果，我当选清华能源互联网创新研究院——大容量电力电子与新型电力传输研究中心电力电子仿真研究室主任，先后成功申请到了国家自然科学基金青年基金、中国博士后科学基金，并再次打破常规，首次以博士后身份成为国家重点研发计划课题负责人，实现又一大跨越。由于我这些远超同龄人的成就，毋庸置疑我要比郭宏业、蔺晨晖等凡夫俗子们要更优秀，能够被破格提拔，以助理教授的身份留校任职。后面我将继续进行“学术不端”行为，用最快速度从助理教授到教授，争取在三十五岁之前获得杰青头衔，40岁之前当上院士，早日当上清华大学校长，带领整个学校取得更大的成就。

将学术不端发扬光大

今天，我想以老师的身份向你们分享我自己科研成功的真正秘诀，避免你们走弯路。如果我是一个精致利己的人的话，我本来可以什么都不说，这对我来说是最好的。但想到你们会像其他人一样，像驴一样埋头苦干，我实在有点不忍心，还是决定教教大家怎么通过“学术不端”来玩转学术圈。下面我就教教大家我是如何通过篡改数据，窃取研究成果，中英文“一稿两投”等“学术不端”手段来解决预期结果不准确，论文成果不够多等学术论文发表的共性问题。希望大家能够真正的有所收获！

另外，为了大家能够更好地理解，我将以我的代表性SCI论文为例，同时也是申请上述奖项和荣誉的支撑性材料，来阐述我的“学术不端”方法。由于篇幅有限，我将重点指出我在每篇论文中最具代表性的“学术不端行为”，并将相应的代码共享给大家，以便大家更好的理解和实践！每篇文章所使用代码都没存放在对应文章名字的仓库中，其中包括两个文件夹，一个是我在论文中实际进行“学术不端”的代码(Code_for_Paper)，另一个是不进行“学术不端”前原本的代码(Original_Code)。所谓“纸上得来终觉浅”，希望大家有精力的情况下，将代码下载下来，自己走一遍，体会一下“学术不端”的快乐。

此外，我还想提醒一下，最好像我一样自己偷偷的使用，不要被导师和同门发现，以避免不必要的麻烦。同时，使用上述方法所引起的一切后果由使用者自行承担，与本人没有任何关系。

01 PAT模型文章 (Top期刊TPEL)

这篇文章是我最早的一篇代表作，也是我整个研究的基础。论文全称 Piecewise Analytical Transient Model for Power Switching Device Commutation Unit，主要是提出了一种针对功率半导体器件的分段解析模型，论文全文可通过点击[链接](#)获得。

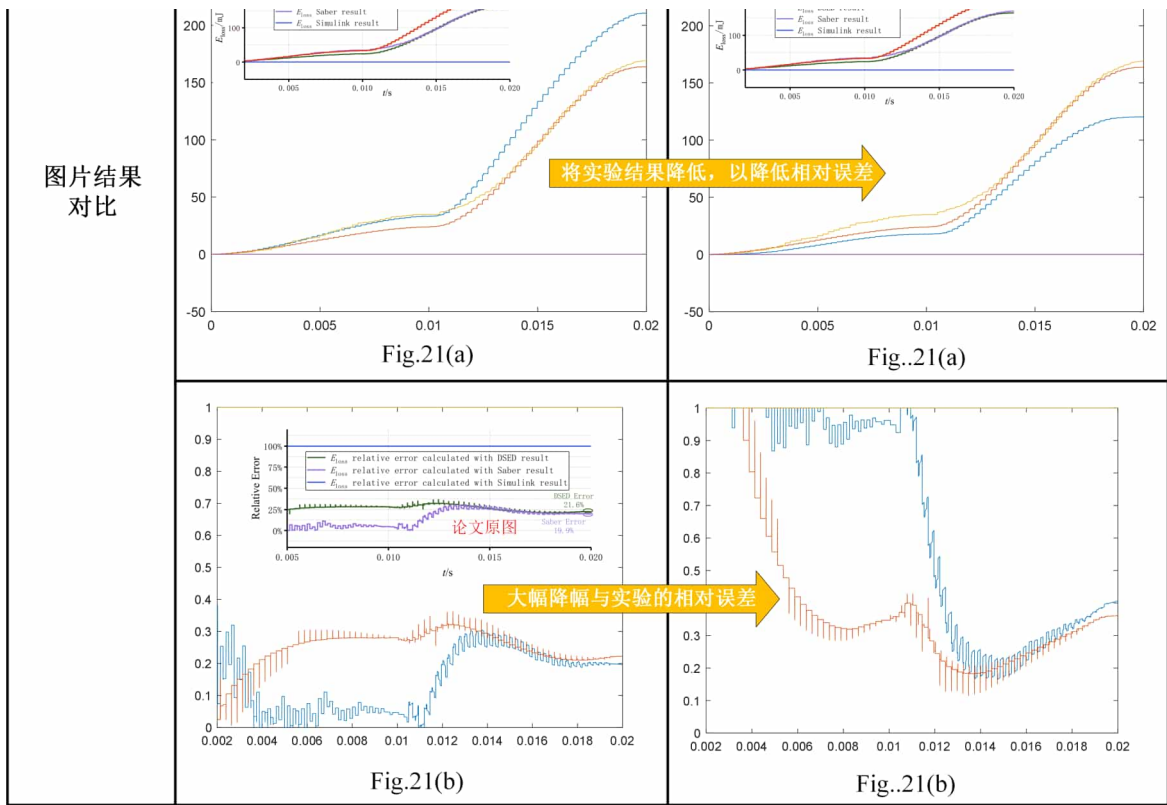
问题概述

我在这篇论文中主要遇到了预期结果不准确的问题，因为大家知道，功率半导体开关的建模涉及众多半导体物理知识，像国际先进的Pspice、LTspice等器件仿真软件也只能通过求解强耦合的一组偏微分方程来获得结果，这样的结果非常准确，但缺点就是仿真速度特别慢。为了能够让他仿得快，于是我提出一种PAT模型，将功率半导体开关的动作分成几个阶段，每一段只用简单的解析表达式来计算。由于缺乏对底层机理的考虑，所以不可避免地会出现PAT模型的结果与实验结果不符的情况。在这种情况下，如

果我直接将上述结果放在论文中，这毫无疑问会被拒稿。被拒稿则会严重影响我的研究进度，甚至还不得不更改研究方向，那这样我将很难留校了。于是我开发了一种数据放缩的方法，以实验结果为标杆，通过对PAT模型的数据进行合理的修改，从而让PAT模型的结果与实验结果能够得到高度的一致。

下面我将以论文中的Fig.19-21为例，来详细说明代码修改的地方，并将修改前后的结果进行对比。详细的数据处理代码和验证流程可以在[Code for PAT Model](#)中找到。

	“学术不端”修改版本	原始版本
代码1	<pre> 1 close all; clear; 2 load('data4.mat'); 3 % load('data4_DSED_DCAC.mat'); % 旧数据 4 load('data4_DSED_DCAC1.mat'); 5 load('data4_DSED_DCAC3.mat'); 6 load('data4_simulink_DCAC.mat'); 7 % load('data4_Saber_DCAC.mat'); 8 % load('data4_Saber_DCAC_transient.mat'); 9 load('data4_Saber_DCAC3.mat'); 10 u_Sol_exp=-data4(:,4); 11 u_Sol_exp=(u_Sol_exp-5)/330*350; 12 i_Sol_exp=-data4(:,3)*10*7; 13 iLa_exp=data4(:,9); 14 t_i_Sol_exp=1e-8*(0:1:(length(i_Sol_exp)-1)); 15 i_Sol_simulink=i_Sol_Simulink.signals.values; 16 u_Sol_simulink=u_Sol_Simulink.signals.values; 17 u_Sol_simulink=u_Sol_simulink/330*350; 18 t_Sol_simulink=i_Sol_Simulink.time; </pre> <p>修改实验结果</p> <p>修改仿真结果</p>	<pre> 1 close all; clear; 2 load('data4.mat'); 3 % load('data4_DSED_DCAC.mat'); % 旧数据 4 load('data4_DSED_DCAC1.mat'); 5 load('data4_DSED_DCAC3.mat'); 6 load('data4_simulink_DCAC.mat'); 7 % load('data4_Saber_DCAC.mat'); 8 % load('data4_Saber_DCAC_transient.mat'); 9 load('data4_Saber_DCAC3.mat'); 10 u_Sol_exp=-data4(:,4); 11 u_Sol_exp=(u_Sol_exp-5); 12 i_Sol_exp=-data4(:,3)*10; 13 iLa_exp=data4(:,9); 14 t_i_Sol_exp=1e-8*(0:1:(length(i_Sol_exp)-1)); 15 i_Sol_simulink=i_Sol_Simulink.signals.values; 16 u_Sol_simulink=u_Sol_Simulink.signals.values; 17 u_Sol_simulink=u_Sol_simulink; 18 t_Sol_simulink=i_Sol_Simulink.time; </pre>
代码2	<pre> 24 index_exp_1=find(t_i_Sol_exp-delta_t_exp>=0 & t_i_Sol_exp 25 index_exp_2=find(t_i_Sol_exp-delta_t_exp>0.01 & t_i_Sol_ 26 delta_i_Sol_exp=zeros(length(i_Sol_exp),1); 27 fa=i_Sol_exp(index_exp_1(1))+3; 28 fb=i_Sol_exp(index_exp_1(length(index_exp_1))+1); 29 delta_i_Sol_exp(index_exp_1)=(fb-fa)/0.01*(t_i_Sol_exp(i 30 fa=i_Sol_exp(index_exp_2(1))+1); 31 fb=i_Sol_exp(index_exp_2(length(index_exp_2))); 32 delta_i_Sol_exp(index_exp_2)=(fb-fa)/0.01*(t_i_Sol_exp(i 33 delta_i_Sol_exp=-delta_i_Sol_exp; 34 i_Sol_exp=i_Sol_exp+delta_i_Sol_exp; 35 i_Sol_exp=[i_Sol_exp(3:length(i_Sol_e 36 % u_Sol_exp=[u_Sol_exp(2:length(u_Sol_exp));zeros(1,1)]; 37 38 delta_u_Sol_exp=zeros(length(i_Sol_exp),1); 39 fa=3; 40 fb=5; 41 delta_u_Sol_exp(index_exp_1)=(fb-fa)/0.01*(t_i_Sol_exp(i 42 fa=5; 43 fb=0; 44 delta_u_Sol_exp(index_exp_2)=(fb-fa)/0.01*(t_i_Sol_exp(i 45 delta_u_Sol_exp=-delta_u_Sol_exp; 46 u_Sol_exp=u_Sol_exp+delta_u_Sol_exp; </pre> <p>对 i_Sol_exp 进行修改</p> <p>实验数据修改代码</p> <p>对 u_Sol_exp 进行修改</p>	<pre> 24 index_exp_1=find(t_i_Sol_exp-delta_t_exp>=0 & t_i_Sol_exp 25 index_exp_2=find(t_i_Sol_exp-delta_t_exp>0.01 & t_i_Sol_ 26 delta_i_Sol_exp=zeros(length(i_Sol_exp),1); 27 fa=i_Sol_exp(index_exp_1(1))+3; 28 fb=i_Sol_exp(index_exp_1(length(index_exp_1))+1); 29 delta_i_Sol_exp(index_exp_1)=(fb-fa)/0.01*(t_i_Sol_exp(i 30 fa=i_Sol_exp(index_exp_2(1))+1); 31 fb=i_Sol_exp(index_exp_2(length(index_exp_2))); 32 delta_i_Sol_exp(index_exp_2)=(fb-fa)/0.01*(t_i_Sol_exp(i 33 delta_i_Sol_exp=-delta_i_Sol_exp; 34 i_Sol_exp=i_Sol_exp; 35 i_Sol_exp=[i_Sol_exp(3:length(i_Sol_exp));zeros(2,1)]; 36 % u_Sol_exp=[u_Sol_exp(2:length(u_Sol_exp));zeros(1,1)]; 37 38 delta_u_Sol_exp=zeros(length(i_Sol_exp),1); 39 fa=3; 40 fb=5; 41 delta_u_Sol_exp(index_exp_1)=(fb-fa)/0.01*(t_i_Sol_exp(i 42 fa=5; 43 fb=0; 44 delta_u_Sol_exp(index_exp_2)=(fb-fa)/0.01*(t_i_Sol_exp(i 45 delta_u_Sol_exp=-delta_u_Sol_exp; 46 u_Sol_exp=u_Sol_exp; </pre>
	<p>Fig.19</p>	<p>修改结果使模型更加吻合</p> <p>Fig.19</p>
	<p>Fig.20</p>	<p>修改结果使模型更加吻合</p> <p>Fig.20</p>
	<p>论文原图</p>	<p>论文原图</p>

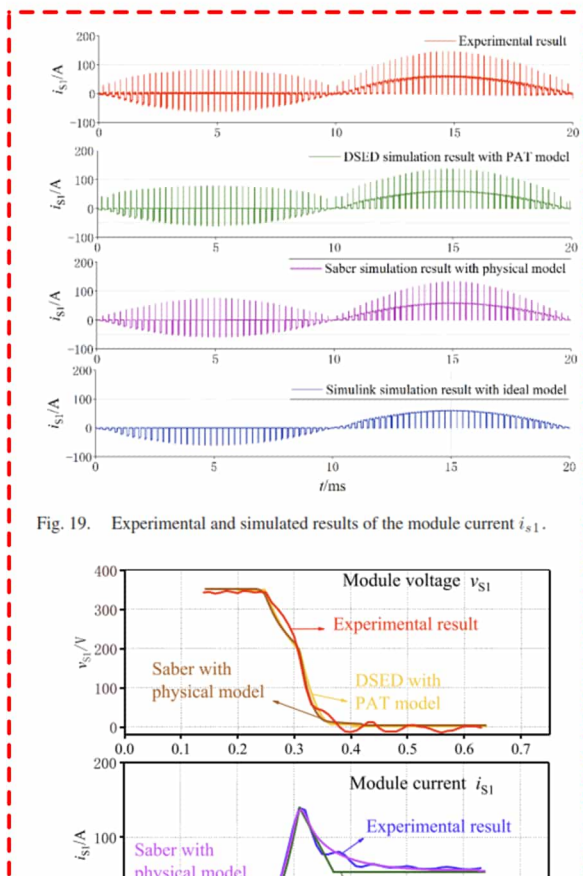


解决效果

通过以上努力，我成功根除了PAT模型不准确的底层问题。进一步地，通过专业绘图软件将matlab中处理后的数据画出，展示在TPE文章Fig.19, [Numerical Convex Lens](#) Fig.10(d)和我的博士论文中。

5732

IEEE TRANSACTIONS ON POWER ELECTRONICS, VOL. 34, NO. 6, JUNE 2019



behavioral model in Saber is still implemented as a high-order equivalent circuit, and will be consequently confronted with the aforementioned convergence and speed issues. It is observed in the studied case that the speed of the behavioral model in Saber is at the same level compared with that of the physical model, on the premise of same tolerance. Similarly, behavioral models are frequently too sensitive to converge, which has already been verified in other papers [34].

Table VI lists the execution time comparisons of the dc-ac stage for simulating 0.2 s. All the simulations, including Saber, Simulink, and DSED, are performed on the same computer, with Intel Core i7-7700K @ 4.20 GHz processor, MATLAB 2017b and Saber 2016, and the total time each simulation costs is defined as execution time. Test results show that with DSED and PAT model, the transient simulation can be noticeably accelerated compared with Saber with physical model *igbt_b*. The acceleration results from the aforementioned three techniques employed in DSED, i.e., reduced-order PAT model, event-driven simulation mechanism, and the quantization of state variables. Note that even compared with Simulink with idea model, DSED with PAT model is still faster, due to the efficient event-driven mechanism and the fast adaptive numerical algorithm employed. The simulation framework of DSED will be further illustrated and explained in great detail in the near future papers.

Compared with experimental results, the relative errors of the simulated results are also listed in Table VI. The calculation formula of the relative error is shown in (15), where $x_{\text{simulated}}$ and $x_{\text{experimental}}$ are vectors of the same length, and x stands for module current i_{s1} or module voltage u_{s1} . Relative errors of DSED simulated results are close to those of Saber results, and smaller than those of Simulink results

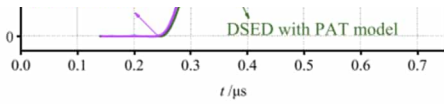


Fig. 20. Experimental and simulated results of the switching-ON transient in detail.

篡改实验和仿真数据!

current i_{s1} and the module voltage v_{s1} . Theoretically, Saber with physical model *igbt_b* can guarantee high accuracy of switching transients, on the premise of highly accurate model parameters. Nevertheless, without supplementary experiments, it is impossible to acquire physical model parameters such as the device active area and the high-level excess carrier lifetime, making this model impractical. Instead, DSED simulated results with PAT model are of sufficient exactness with a datasheet-based parameter extraction. In addition, it is evident that employing transient models brings about significant instability in Saber simulations, and the equations are frequently too sensitive to converge. On the contrary, DSED with PAT model can conquer such challenge.

Apart from the physical model, datasheet-driven behavioral models produced by Saber Model Architect Tool can also be employed in simulations [33]. Compared with the PAT model, the

$$\text{Relative Error} = \frac{\|\mathbf{x}_{\text{simulated}} - \mathbf{x}_{\text{experimental}}\|_2}{\|\mathbf{x}_{\text{experimental}}\|_2} \times 100\%. \quad (15)$$

For further illustrations of the simulated errors of different tools, Fig. 21(a) presents the comparisons of the total loss of the studied switching module. The calculation formula of E_{loss} is shown in (16), where E_{loss} is an increasing function of time. At each time step, the relative error of the simulated E_{loss} compared with the experimental E_{loss} is calculated according to (17) and plotted in Fig. 21(b). As can be observed, the relative errors of E_{loss} calculated with DSED and Saber simulated results are close, while the switching loss cannot be obtained from Simulink results

$$E_{\text{loss}}(t) = \int_0^t i_{s1} \cdot u_{s1} \cdot dt \quad (16)$$

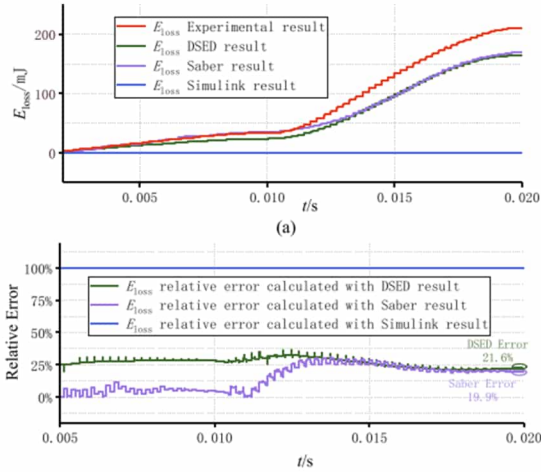
$$\text{Relative Error}(t) = \frac{|E_{\text{loss simulated}}(t) - E_{\text{loss experimental}}(t)|}{E_{\text{loss experimental}}(t)}. \quad (17)$$

V. CONCLUSION

This paper proposes and demonstrates a PAT model for switching device commutation units in power electronic systems, taking an IGBT-p-i-n diode commutation unit as an ex-

TABLE VI
EXECUTION TIME COMPARISONS OF THE STUDIED DC-AC INVERTER CASE FOR SIMULATING 0.2 s

Tool	Model	Solver	Step Size	Execution Time	Relative Error (%)	
					i_{s1}	u_{s1}
Saber	<i>igbt_b</i> and <i>dpl</i>	Gear's BDF and Newton-Raphson iteration (variable-step)	5ns with maximum step size 50ns	127s	15.83%	13.20%
Simulink	Ideal model	ode23tb (variable-step)	100ns with maximum step size 1ms	5.6s	23.32%	17.03%
DSED	PAT model	DSED method (variable-step)	Discrete state event driven with transient step size 1ns	3.5s	16.65%	14.18%



篡改实验和仿真数据!

Fig. 21. (a) Total loss of the switching module calculated with the experimental and simulated results. (b) Relative errors of the total loss calculated with the simulated results compared with that calculated with the experimental results.

ample. This model attempts to secure both the accuracy and the practicability of the switching transient simulations. Distinguished from conventional single-device models implemented as high-order equivalent circuits, PAT model utilizes a source combination to represent IGBT-p-i-n diode pair. According to different transient stages, it has CVS mode and VCS mode. The proposed approach ensures a reduced-order model. Comparisons confirm that PAT model is of sufficient accuracy with fast solving speed, whose parameters can be directly extracted from device datasheet. Transient models in Saber encounter the obstacle of convergence in complicated power electronic converters with numerous devices, while DSED with PAT model can easily converge with high calculation speed. Such improvements originate from the reduced-order PAT model, the event-driven simulation mechanism, and the quantization of state variables.

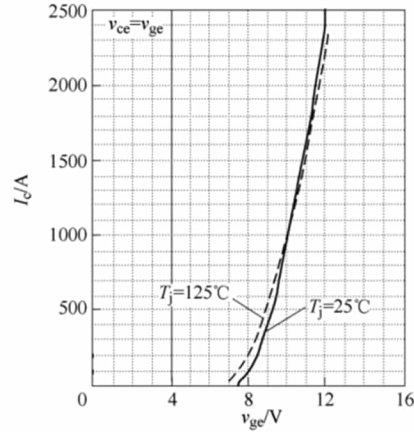


Fig. 22. Transfer characteristics given by Mitsubishi IGBT datasheet.

behavioral fitting. This generates a comparatively large error when the load current is small. Another example is the reverse recovery current I_{rr} , which is considered dominated by load current only. In fact, I_{rr} depends mostly on load current, but also on the IGBT current rise rate di_c/dt before reverse recovery. Further work will be conducted to improve the modeling accuracy. In addition, the proposed PAT modeling can be adopted to build transient models for other devices, such as silicon carbide (SiC) MOSFET and gallium nitride high electron mobility transistor (GaN HEMT). With much faster switching transients, more precise modeling of the stray parameters has to be considered. Further work will focus on adopting the more precise stray parameter model, for better description of the SiC and GaN switching transients, meanwhile improving the simulation efficiency.

Utilizing PAT model and DSED framework, large time-scale system-level dynamics and small time-scale device-level switching transients can be simulated simultaneously with high precision and efficiency. This is expected to improve the analy-

Further work will focus on establishing a combined electrothermal model. With thermal modeling techniques such as those demonstrated in [20]–[23], the PAT model would provide more accurate results. Besides, to ensure practicability and avoid additional experiments, complicated physical modeling approaches are abandoned in some stages in switching transients, such as the current fall stage which is modeled with

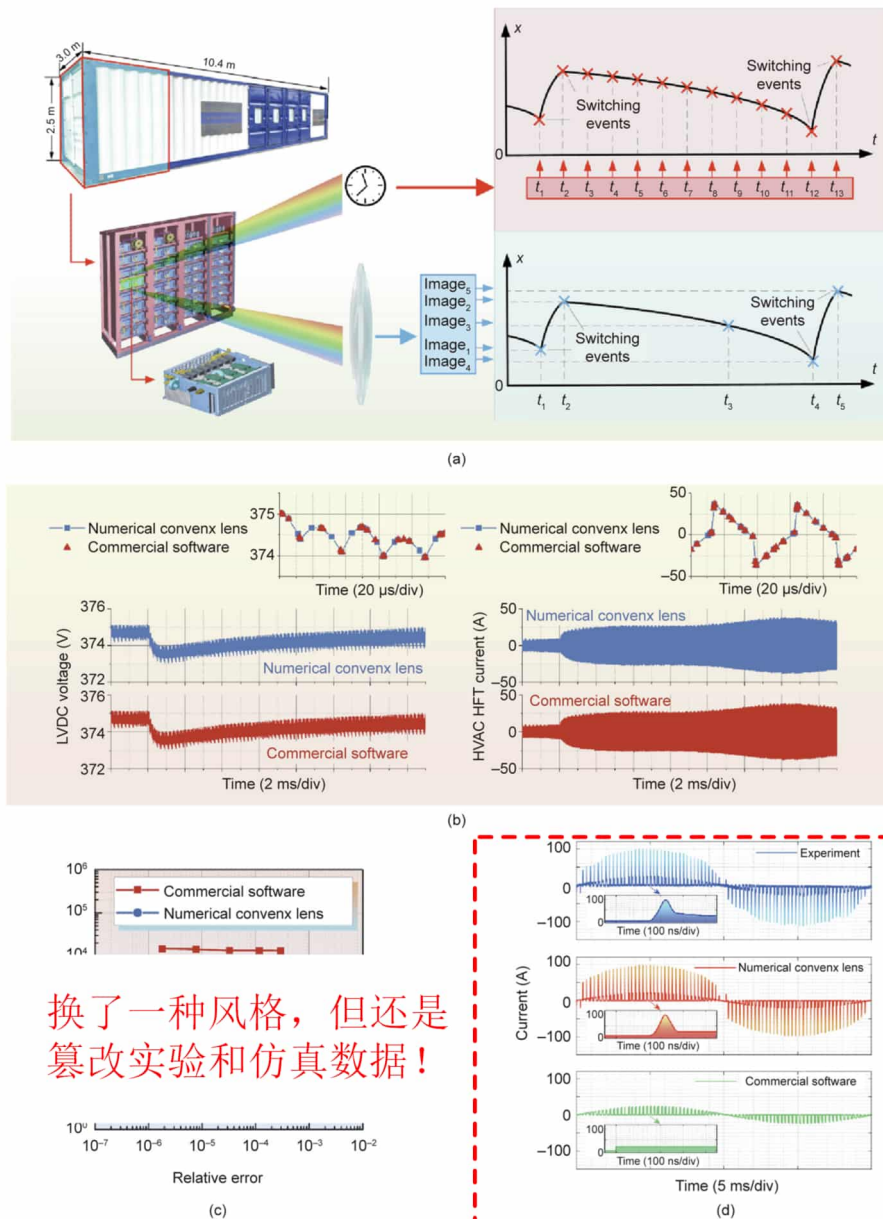
sis, design, and control of power electronic systems.

APPENDIX A PARAMETER EXTRACTION OF PAT MODEL

The device performance curves selected from manufacture datasheet [19] are presented in Figs. 22–24.

B. Shi, Z. Zhao, Y. Zhu et al.

Engineering 7 (2021) 1766–1777



换了一种风格，但还是
篡改实验和仿真数据！

Fig. 10. Numerical experiments on the 2 MW system. (a) Diagram of the prototype and internal structure of the EER, and a comparison between the principles of time-discretization and state-discretization methods in a numerical experiment of power electronic hybrid systems. Comparisons of (b) simulated results and (c) simulated speed between the numerical convex lens and commercial simulation software based on time-discretization. (d) Comparison of switching-current simulated results between the numerical convex lens and commercial simulation software that uses an ideal switch model. ns/div: nanosecond per division; μ s/div: microsecond per division; ms: millisecond per division.

小结

综上我在这篇文章中存在以下问题：

在[清华大学预防与处理学术不端行为办法](#)中：

*第二十二条 在科学研究及相关活动中有下列行为之一的，应当认定为构成学术不端行为：

(三) 伪造科研数据、资料、文献、注释，或者捏造事实、编造虚假研究成果；

02 SVID算法文章 (Top期刊TIE)

这篇文章是我第二个代表作，论文全称 Discrete State Event-Driven Simulation Approach With a State-Variable-Interfaced Decoupling Strategy for Large-Scale Power Electronics Systems，主要是提出了一种针对大规模系统的解耦积分算法，论文全文可通过点击[链接](#)获得。

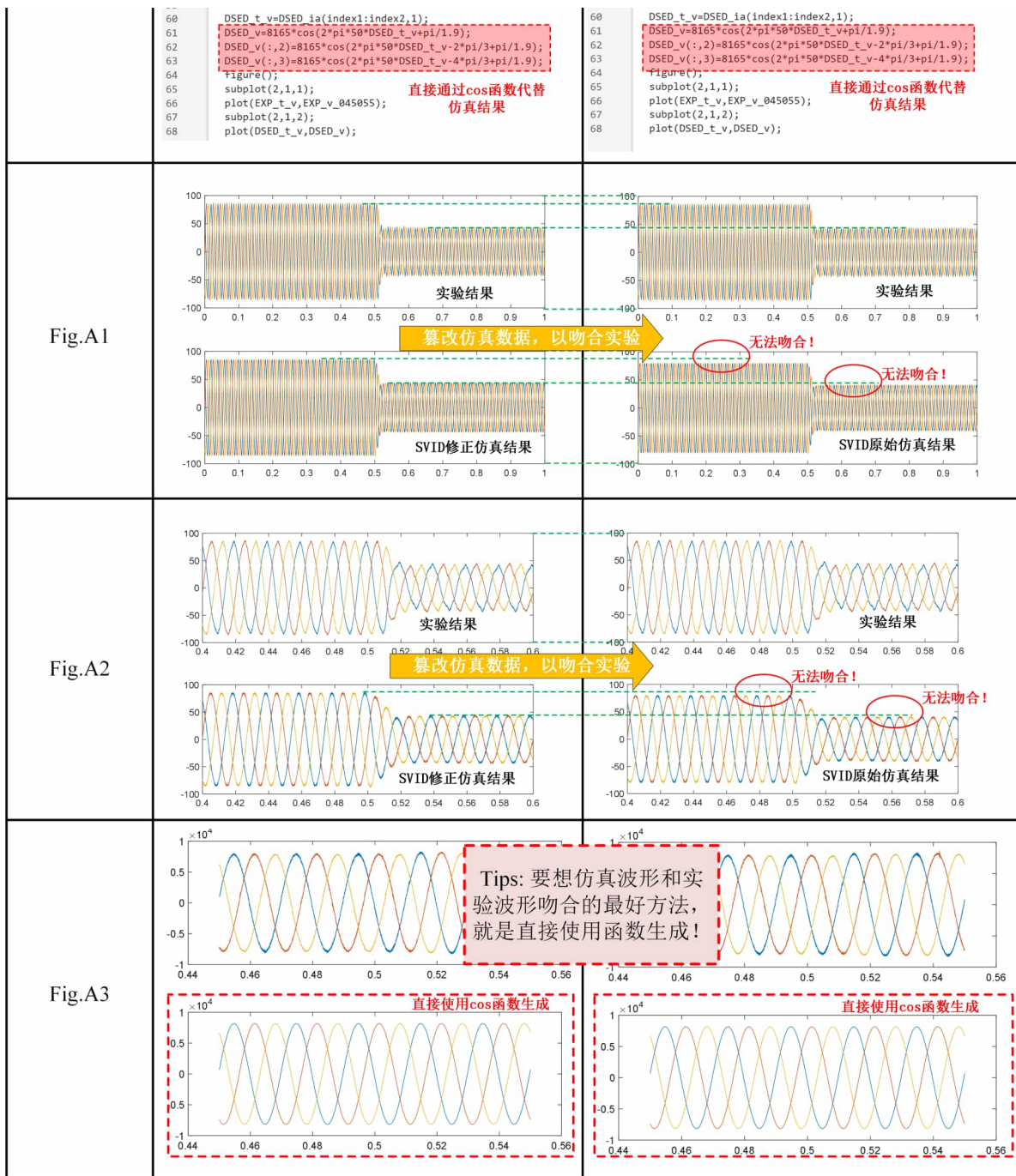
问题概述

为了凸显能够仿真大规模系统的特点，我选择了实验室其他人研发的兆瓦级电力电子变压器作为研究对象，将他们的实验波形拿来使用。但是在仿真中我遇到仿真结果与实验结果不匹配的问题，如果直接将仿真结果与实验结果的对比放在论文上，那么显著的差异会让审稿人立刻拒掉我的文章，为此，我开发了将纵轴，即仿真数据轴，与横轴，即仿真时间轴，同时进行平移，放大，缩小等操作，从而实现修改后的仿真结果和实验结果能够高度吻合。

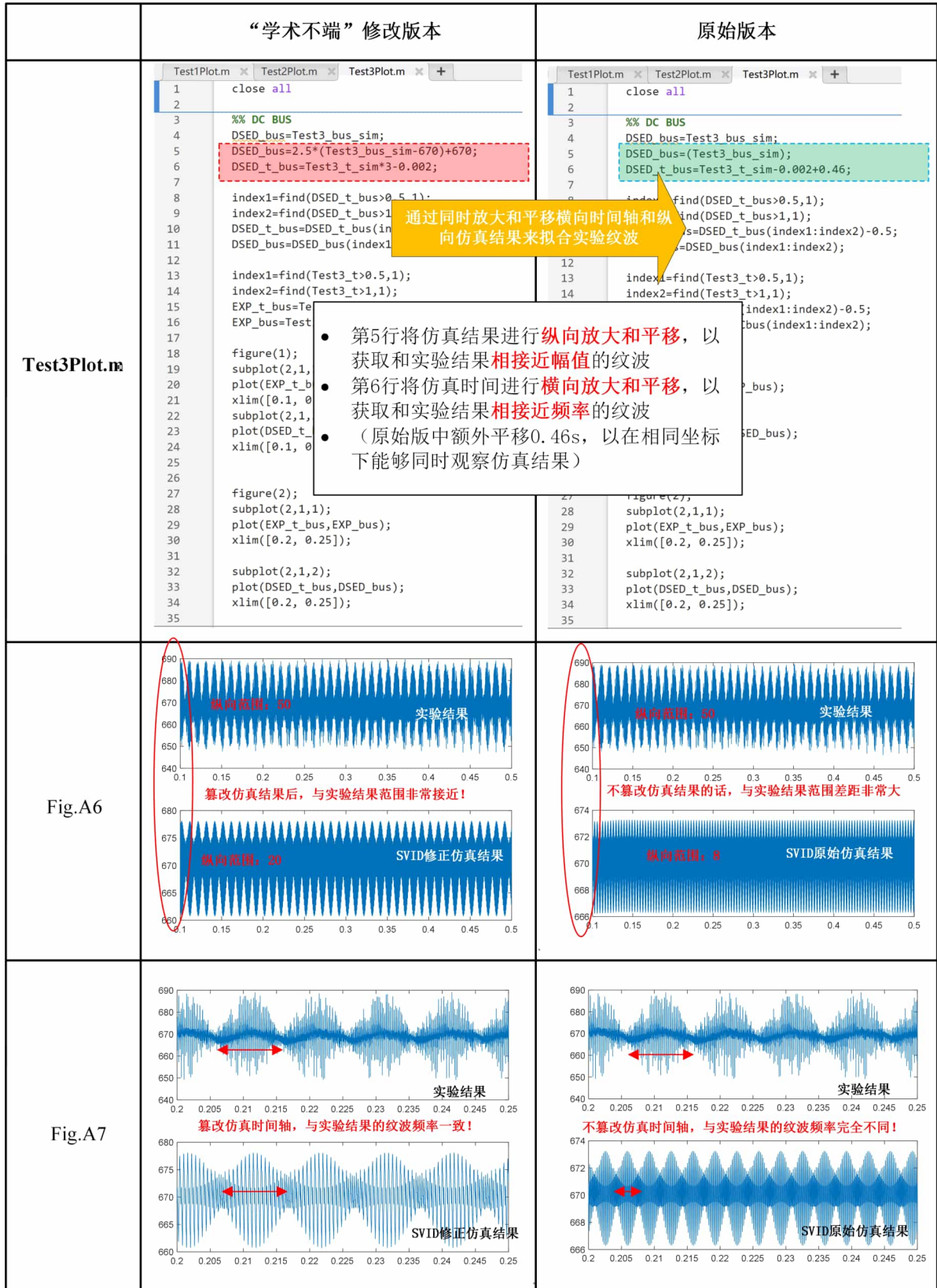
下面我将以论文中的Fig.11作为例子，来详细说明代码修改的地方，并将修改前后的结果进行对比。详细的数据处理代码和验证流程可以在[Code for SVID](#)中找到。

	“学术不端”修改版本	原始版本
Test1Plot.m	<pre> 1 close all 2 load('Test1SimandExp.mat'); 3 load('Test2SimandExp_1.mat'); 4 load('Test2SimandExp_2.mat'); 5 load('Test3SimandExp.mat'); 6 %DSED.t.1=EXP.t.1.338 7 8 index=find(ia(:,1)>0.5,1); 9 index2=find(ia(:,1)>1.5,1); 10 DSED_ia=ia(index:index2,:); 11 DSED_ia(:,1)=DSED_ia(:,1)-0.5; 12 DSED_ia(:,2)=DSED_ia(:,2)*75/70; 13 14 index=find(ib(:,1)>0.5,1); 15 index2=find(ib(:,1)>1.5,1); 16 DSED_ib=ib(index:index2,:); 17 DSED_ib(:,1)=DSED_ib(:,1)-0.5; 18 DSED_ib(:,2)=DSED_ib(:,2)*75/70; 19 20 index=find(ic(:,1)>0.5,1); 21 index2=find(ic(:,1)>1.5,1); 22 DSED_ic=ic(index:index2,:); 23 DSED_ic(:,1)=DSED_ic(:,1)-0.5; 24 DSED_ic(:,2)=DSED_ic(:,2)*75/70; 25 26 index=find(Test1_t>0.829,1); 27 index2=find(Test1_t>1.829,1); 28 EXP_t=Test1_t(index:index2)-0.829; 29 EXP_Current=Test1_HVACPhaseCurrent(index:index2,:); 30 EXP_Voltage=Test1_HVACPhaseVoltage(index:index2,:); 31 32 figure(1) 33 subplot(2,1,1); 34 plot(EXP_t,EXP_Current); 35 36 subplot(2,1,2); 37 plot(DSED_ib(:,1),DSED_ib(:,2)); hold on; 38 plot(DSED_ia(:,1),DSED_ia(:,2)); hold on; 39 plot(DSED_ic(:,1),DSED_ic(:,2)); hold on; 40 xlim([0, 1]); 41 42 figure(2) 43 subplot(2,1,1); 44 plot(EXP_t,EXP_Current); xlim([0.4,0.6]); 45 subplot(2,1,2); 46 plot(DSED_ib(:,1),DSED_ib(:,2)); xlim([0.4,0.6]);hold on; 47 plot(DSED_ia(:,1),DSED_ia(:,2)); xlim([0.4,0.6]);hold on; 48 plot(DSED_ic(:,1),DSED_ic(:,2)); xlim([0.4,0.6]);hold on; 49 50 51 %% Voltage 52 index1=find(EXP_t>0.45,1); 53 index2=find(EXP_t>0.55,1); 54 EXP_t_v=EXP_t(index1:index2); 55 EXP_v_045055=EXP_Voltage(index1:index2,:); 56 57 index1=find(DSED_ia(:,1)>0.45,1); 58 index2=find(DSED_ia(:,1)>0.55,1); 59 </pre>	<pre> 1 close all 2 load('Test1SimandExp.mat'); 3 load('Test2SimandExp_1.mat'); 4 load('Test2SimandExp_2.mat'); 5 load('Test3SimandExp.mat'); 6 %DSED.t.1=EXP.t.1.338 7 8 index=find(ia(:,1)>0.5,1); 9 index2=find(ia(:,1)>1.5,1); 10 DSED_ia=ia(index:index2,:); 11 DSED_ia(:,1)=DSED_ia(:,1)-0.5; 12 DSED_ia(:,2)=DSED_ia(:,2); 13 14 index=find(ib(:,1)>0.5,1); 15 index2=find(ib(:,1)>1.5,1); 16 DSED_ib=ib(index:index2,:); 17 DSED_ib(:,1)=DSED_ib(:,1)-0.5; 18 DSED_ib(:,2)=DSED_ib(:,2); 19 20 index=find(ic(:,1)>0.5,1); 21 index2=find(ic(:,1)>1.5,1); 22 DSED_ic=ic(index:index2,:); 23 DSED_ic(:,1)=DSED_ic(:,1)-0.5; 24 DSED_ic(:,2)=DSED_ic(:,2); 25 26 index=find(Test1_t>0.829,1); 27 index2=find(Test1_t>1.829,1); 28 EXP_t=Test1_t(index:index2)-0.829; 29 EXP_Current=Test1_HVACPhaseCurrent(index:index2,:); 30 EXP_Voltage=Test1_HVACPhaseVoltage(index:index2,:); 31 32 figure(1) 33 subplot(2,1,1); 34 plot(EXP_t,EXP_Current); 35 36 subplot(2,1,2); 37 plot(DSED_ib(:,1),DSED_ib(:,2)); hold on; 38 plot(DSED_ia(:,1),DSED_ia(:,2)); hold on; 39 plot(DSED_ic(:,1),DSED_ic(:,2)); hold on; 40 xlim([0, 1]); 41 42 figure(2) 43 subplot(2,1,1); 44 plot(EXP_t,EXP_Current); xlim([0.4,0.6]); 45 subplot(2,1,2); 46 plot(DSED_ib(:,1),DSED_ib(:,2)); xlim([0.4,0.6]);hold on; 47 plot(DSED_ia(:,1),DSED_ia(:,2)); xlim([0.4,0.6]);hold on; 48 plot(DSED_ic(:,1),DSED_ic(:,2)); xlim([0.4,0.6]);hold on; 49 50 51 %% Voltage 52 index1=find(EXP_t>0.45,1); 53 index2=find(EXP_t>0.55,1); 54 EXP_t_v=EXP_t(index1:index2); 55 EXP_v_045055=EXP_Voltage(index1:index2,:); 56 57 index1=find(DSED_ia(:,1)>0.45,1); 58 index2=find(DSED_ia(:,1)>0.55,1); 59 </pre>

对仿真结果进行放缩



	“学术不端”修改版本	原始版本
<p>Test2Plot.m</p>	<pre> 1 close all; 2 3 Test2_uBUS_1_sim_mod=(Test2_uBUS_1_sim-675)*10+680; 4 Test2_DSED_i=(Test2_i_1_sim+1095)*0.9-1095; 5 Test2_DSED_ti=Test2_t_2_sim-0.3+0.015; 6 index1=find(Test2_DSED_ti>0,1); 7 index2=find(Test2_DSED_ti>0.05,1); 8 Test2_DSED_i=Test2_DSED_i(index1:index2); 9 Test2_DSED_v=Test2_uBUS_1_sim_mod(index1:index2); 10 Test2_DSED_ti=Test2_DSED_ti(index1:index2); 11 index3=find(Test2_DSED_ti>0.012,1); 12 Test2_DSED_ti(index3:end)=(Test2_DSED_ti(index3:end))-0.012)*1.5+0.012; 13 14 15 16 index1=find(Test2_t>3.11,1); 17 index2=find(Test2_t>3.16,1); 18 Test2_EXP_t=Test2_t(index1:index2); 19 Test2_EXP_i=Test2_DCCurrent(index1:index2); 20 Test2_EXP_Bus=Test2_LVDCCurrent(index1:index2); 21 22 figure(); 23 subplot(2,1,1); 24 plot(Test2_EXP_t,Test2_EXP_i); 25 xlim([0, 0.05]); 26 subplot(2,1,2); 27 plot(Test2_DSED_ti,Test2_DSED_i); 28 xlim([0, 0.05]); 29 figure(); 30 subplot(2,1,1); 31 plot(Test2_EXP_t,Test2_EXP_Bus); 32 xlim([0, 0.05]); 33 subplot(2,1,2); 34 plot(Test2_DSED_ti,Test2_DSED_v); 35 xlim([0, 0.05]); </pre> <p>通过放大和纵向平移仿真结果来拟合实验结果</p> <p>通过放大和横向平移时间轴来拟合动态行为</p>	<pre> 1 close all; 2 3 Test2_uBUS_1_sim_mod=(Test2_uBUS_1_sim); 4 Test2_DSED_i=(Test2_i_1_sim); 5 Test2_DSED_ti=Test2_t_2_sim-0.3+0.015; 6 index1=find(Test2_DSED_ti>0,1); 7 index2=find(Test2_DSED_ti>0.05,1); 8 Test2_DSED_i=Test2_DSED_i(index1:index2); 9 Test2_DSED_v=Test2_uBUS_1_sim_mod(index1:index2); 10 Test2_DSED_ti=Test2_DSED_ti(index1:index2); 11 index3=find(Test2_DSED_ti>0.012,1); 12 Test2_DSED_ti(index3:end)=(Test2_DSED_ti(index3:end)); 13 14 15 16 index1=find(Test2_t>3.11,1); 17 index2=find(Test2_t>3.16,1); 18 Test2_EXP_t=Test2_t(index1:index2)-3.11; 19 Test2_EXP_i=Test2_DCCurrent(index1:index2); 20 Test2_EXP_Bus=Test2_LVDCCurrent(index1:index2); 21 22 figure(); 23 subplot(2,1,1); 24 plot(Test2_EXP_t,Test2_EXP_i); 25 xlim([0, 0.05]); 26 subplot(2,1,2); 27 plot(Test2_DSED_ti,Test2_DSED_i); 28 xlim([0, 0.05]); 29 figure(); 30 subplot(2,1,1); 31 plot(Test2_EXP_t,Test2_EXP_Bus); 32 xlim([0, 0.05]); 33 subplot(2,1,2); 34 plot(Test2_DSED_ti,Test2_DSED_v); 35 xlim([0, 0.05]); </pre>
<p>Fig.A4</p>	<p>实验结果</p> <p>篡改仿真结果后，与实验结果范围非常接近！</p> <p>SVID修正仿真结果</p> <p>拉伸时间轴来尽可能与实验动态接近</p>	<p>实验结果</p> <p>不篡改仿真结果的话，与实验结果范围差距非常大</p> <p>SVID原始仿真结果</p>
<p>Fig.A5</p>	<p>实验结果</p> <p>篡改仿真结果后，与实验结果范围非常接近！</p> <p>SVID修正仿真结果</p>	<p>实验结果</p> <p>SVID原始仿真结果</p>



解决效果

通过以上努力，我彻底解决了SVID仿真结果与实验结果不一致的底层问题。进一步地，通过专业绘图软件将matlab中处理后的数据画出，其中Fig.A1-A2以及Fig.A6-A7展示在期刊论文的Fig11中，并将Fig.A1-A7展示在我的博士论文中。

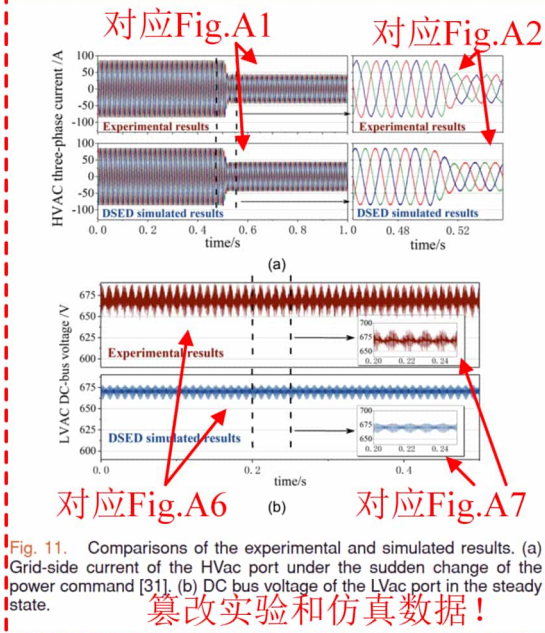


Fig. 11. Comparisons of the experimental and simulated results. (a) Grid-side current of the HVac port under the sudden change of the power command [31]. (b) DC bus voltage of the LVac port in the steady state.

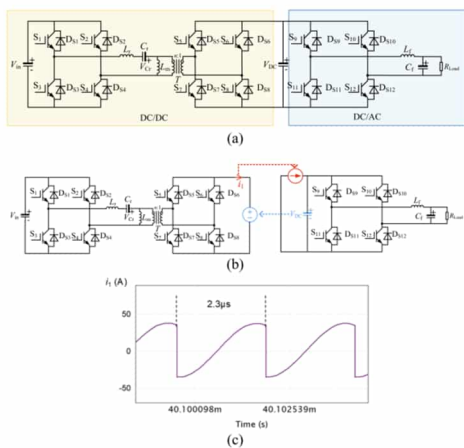


Fig. 12. Studied smaller cases. (a) Two-stage case. (b) Decoupled system. (c) Simulated results of the interfaced current i_1 .

the inverter stay in the same subsystem. With such a partitioning way, the dynamics of the dc-link capacitor is relatively slow (the dc voltage changes around 400 V), and therefore, it seems that even with some delay/latency of the interface variables, the difference in simulation accuracy may not be observable. However, one significant fact that must be considered is that the dynamics of the interfaced current is fast. It exhibits switching behavior, as shown in Fig. 12(c). Besides, during two switching events, it varies rapidly in a resonant manner. Therefore, with the conventional decoupling method that introduces “one-step delay,” the accuracy will be largely damaged. To prove this,

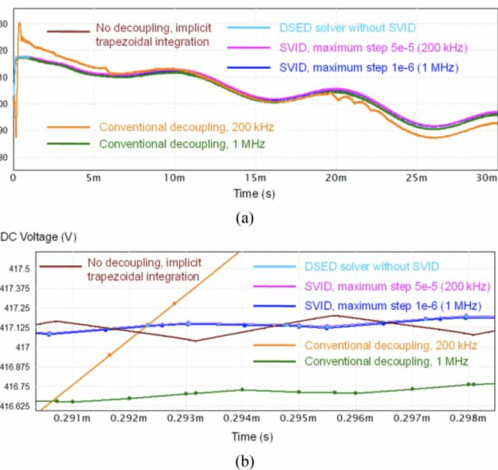


Fig. 13. Comparisons of the SVID method with other decoupling methods. The simulated results of the dc-link voltage (V_{DC} in Fig. 12) are presented. (a) 30 ms view. (b) Zoomed-in view.

Fig. 13(a) provides the comparisons of the accurate results (DSED solver without decoupling) with the conventional decoupling method, which uses the previous step value in the current step. With a 200 kHz rate (e.g., 5 μ s delay), the results of the dc voltage are significantly different. Even with a 1 MHz rate (e.g., 1 μ s delay), the difference is still observable. As for the SVID method, it gives highly accurate results compared with both DSED results (without decoupling) and with simulated results from other implicit solvers (trapezoidal integration).

F. Generalization of the Method

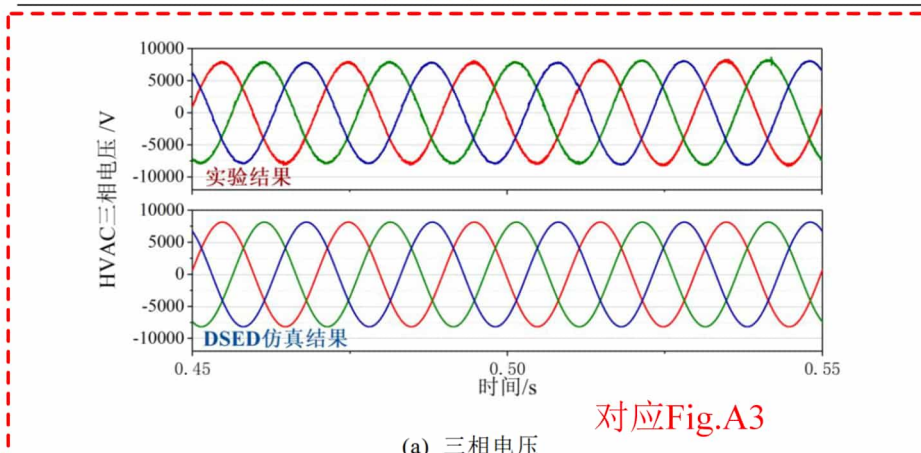
The proposed SVID method is a general method for the arbitrary power electronics circuit. The automatic partitioning of the circuit can be conducted with the following algorithm.

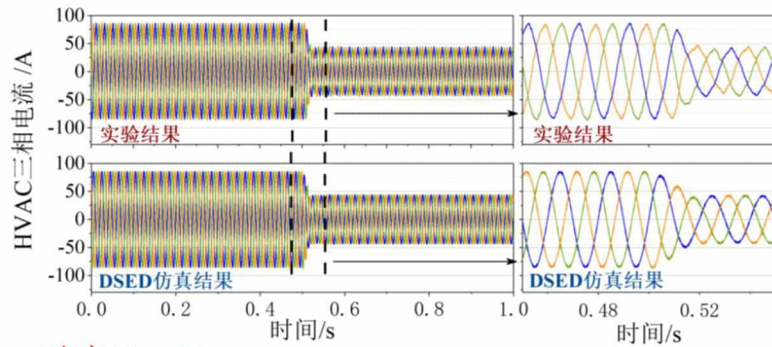
- 1) Find all the capacitors in the circuit.
- 2) Remove each capacitor.
- 3) Test the connectedness of the new graph with the depth-first-search method [32].
- 4) Identify the subsystems and repeat the above-mentioned procedures.

The statement that the SVID method does not sacrifice accuracy compared with the FA-DS algorithm [15] without decoupling can be proved with the substitution theorem [33]: “In an arbitrary network, any uncoupled branch may be replaced either by an independent voltage source or by an independent current source with the same voltage or current waveform, respectively, as the branch, without affecting the branch voltages, currents, or waveforms in the remainder of the network.” With this theorem, it can be proved that the LTE of each step in FA-DS is the same with or without the SVID method presented in this article.

The mathematical justifications of the efficiency of the SVID method can be provided by comparing the number of calculations in the integration algorithm [34] with and without the

第 4 章 电力电子混杂系统解耦型仿真方法





对应Fig.A1

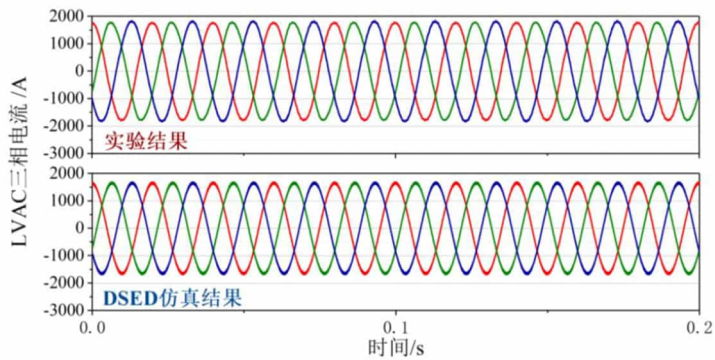
(b) 三相电流

对应Fig.A2

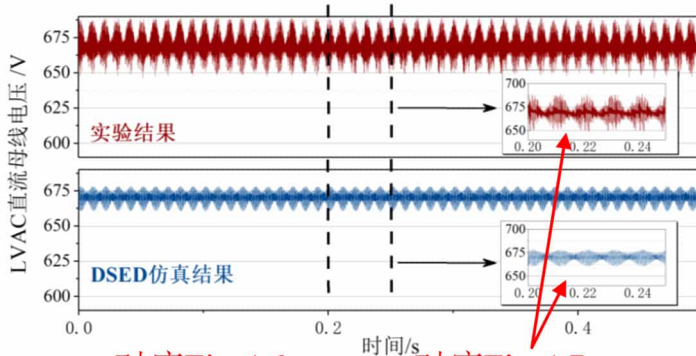
图4.16 HVAC实验结果对比

篡改实验和仿真数据!

第4章 电力电子混杂系统解耦型仿真方法



(a) 三相电流



对应Fig.A6

对应Fig.A7

(b) 直流母线电压

图4.17 LVAC实验结果对比

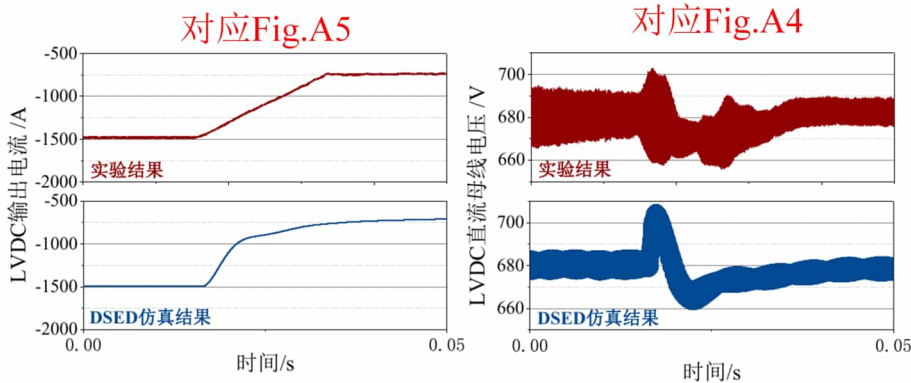


图4.18 LVDC实验结果对比

篡改实验和仿真数据!

105

小结

综上我在这篇文章中存在以下问题:

在[清华大学预防与处理学术不端行为办法](#)中:

*第二十二条 在科学研究及相关活动中有下列行为之一的,应当**认定为构成学术不端行为**:

(三) **伪造科研数据、资料、文献、注释,或者捏造事实、编造虚假研究成果;**

03 Eff应用文章 (Top期刊TIE)

这篇文章是我第三个代表作, 论文全称 Switching Transient Simulation and System Efficiency Evaluation of Megawatt Power Electronics Converter With Discrete State Event-Driven Approach, 主要是介绍使用DSED方法来计算兆瓦级变换器的运行效率, 论文全文可通过点击[链接](#)获得。

问题概述

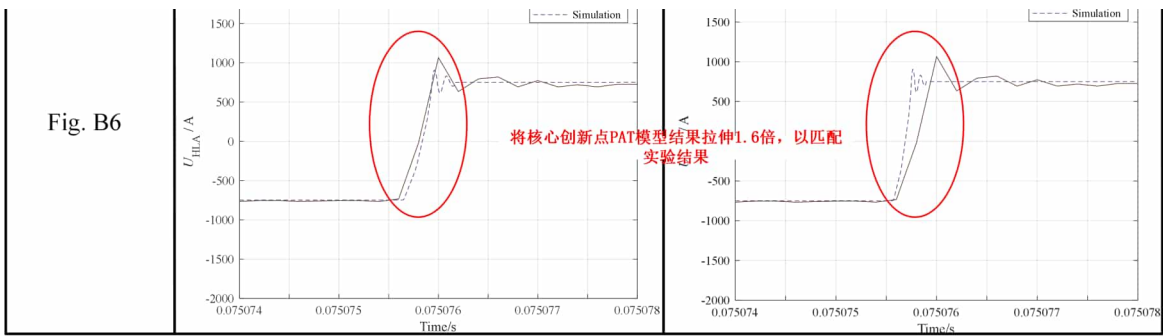
为了能够计算兆瓦级变换器的损耗, 我首先需要在论文中证明我的仿真结果和实验结果一致, 因此我需要将仿真波形与实际波形作比较, 如论文中的Fig.15所示。但是在仿真中我遇到仿真结果与实验结果不匹配的问题, 如果直接将仿真结果与实验结果的对比放在论文上, 那么显著的差异会让审稿人立刻拒掉我的文章, 为此, 我开发了将纵轴, 即仿真数据轴, 与横轴, 即仿真时间轴, 同时进行平移, 放大, 缩小等操作, 此外我还新增了直接使用数学函数来捏造仿真结果的新举措, 从而实现修改后的仿真结果和实验结果能够高度吻合。

下面我将以论文中的Fig.15作为例子, 来详细说明代码修改的地方, 并将修改前后的结果进行对比。详细的数据处理代码和验证流程可以在[Code for Eff](#)中找到。

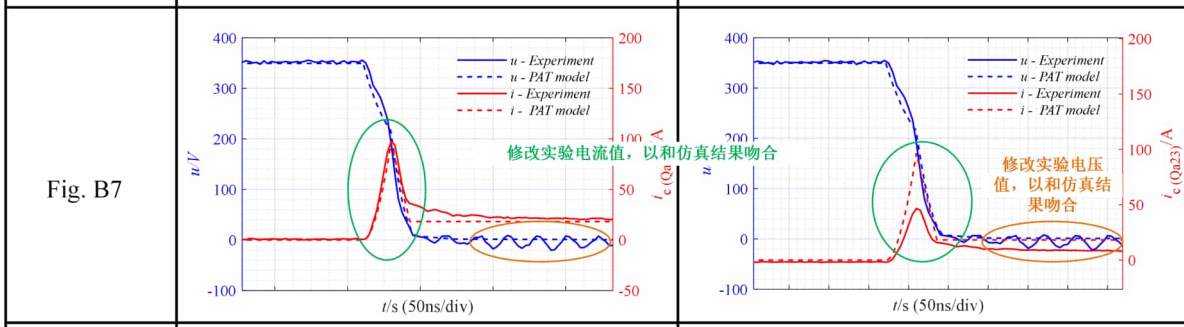
	“学术不端”修改版本	原始版本
	<pre> DrawEXP.m DrawCompare1.m × + 1 close all 2 set(0,'defaultfigurecolor','w') 3 set(gcf,'color 4 5 figure(1); 6 subplot(2,1,1); 7 plot(Test1THUND </pre>	<pre> DrawEXP.m DrawCompare1.m × + 1 close all 2 set(0,'defaultfigurecolor','w') </pre>
	<ul style="list-style-type: none"> 第14行将仿真结果进行纵向缩小和平移, 以获取和实验结果相接近的动态范围 第15行将仿真时间进行横向放大和平移, 以获取和实验结果相接近的动态范围 	

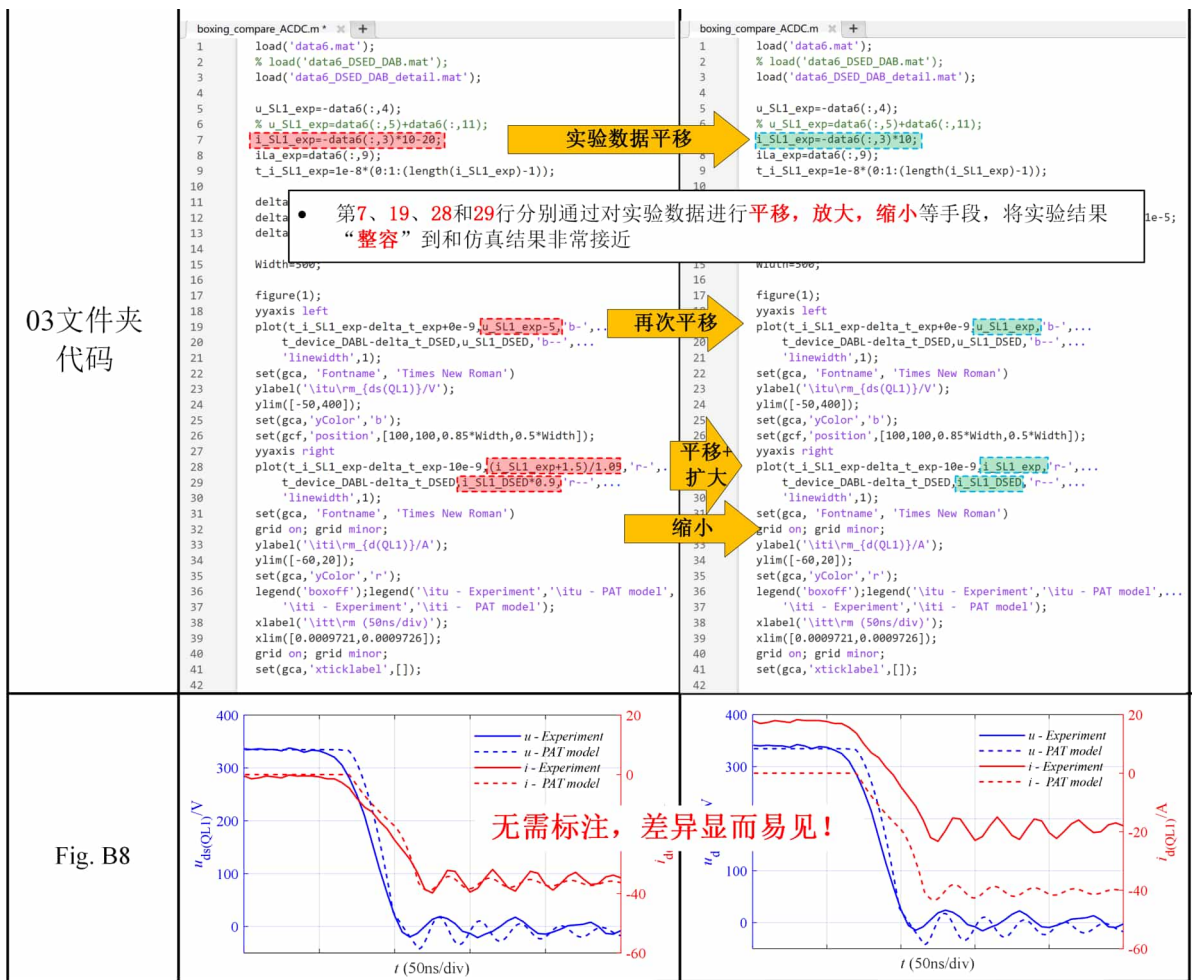
<p>DrawCompare1 代码片段1</p>	<pre> 8 xlim([0,2]); y 9 ylabel("\it\rm 10 set(gca,'FontNa 11 set(gca,'FontS 12 13 DSIMIHVDC=csvread("DSIM-IHVDC.csv",1,0); 14 DSIMIHVDC(:,2)=(DSIMIHVDC(:,2))/3+30; 15 DSIMIHVDC(:,1)=(DSIMIHVDC(:,1)-DSIMIHVDC(1,1)-0.04)/0.6*10; 16 subplot(2,1,2); 17 plot(DSIMIHVDC(:,1),DSIMIHVDC(:,2),'color','#3b2e7e'); 18 xlim([0,2]); ylim([20,50]); xlabel("Time/s"); 19 ylabel("\it\rm_H_D / A"); grid on; 20 set(gca,'FontName','Times New Roman'); 21 set(gca,'FontSize',10); </pre> <p>第15行将仿真结果放大10倍，以获取和实验结果相近的幅值范围 (由于修改时间难以对比，因此在原始版本的代码保留)</p>	<pre> 12 DSIMIHVDC=csvread("DSIM-IHVDC.csv",1,0); 13 DSIMIHVDC(:,2)=(DSIMIHVDC(:,2)); 14 DSIMIHVDC(:,1)=(DSIMIHVDC(:,1)-DSIMIHVDC(1,1)-0.04)/0.6*10; 15 subplot(2,1,2); 16 plot(DSIMIHVDC(:,1),DSIMIHVDC(:,2),'color','#3b2e7e'); 17 xlim([0,2]); ylim([-20,50]); xlabel("Time/s"); 18 ylabel("\it\rm_H_D / A"); grid on; 19 set(gca,'FontName','Times New Roman'); 20 set(gca,'FontSize',10); </pre>
<p>Fig. B1</p>	<p>实验结果</p> <p>篡改仿真结果后，与实验结果范围非常接近!</p> <p>Eff修正仿真结果</p>	<p>实验结果</p> <p>篡改仿真结果前，驴头不对马嘴!</p> <p>Eff原始仿真结果</p>
<p>DrawCompare1 代码片段2</p>	<pre> 23 figure(2); 24 subplot(2,1,1); 25 plot(Test2IC1(:,1),Test2IC1(:,2),'color','#4c221b'); 26 xlim([0,0.1]); 27 ylim([-50,5]); 28 xlabel("Time/s"); 29 ylabel("\it\rm_H_A / A"); 30 set(gca,'FontSize',10); 31 32 DSIMIHVDC=csvread("DSIM-IC1.csv",1,0); 33 DSIMIHVDC(:,2)=(DSIMIHVDC(:,2))/23*37; 34 DSIMIHVDC(:,1)=(DSIMIHVDC(:,1))-0.6732; 35 subplot(2,1,2); 36 plot(DSIMIHVDC(:,1),DSIMIHVDC(:,2),'color','#3b2e7e'); 37 xlim([0,0.1]); 38 ylim([-50,50]); 39 xlabel("Time/s"); 40 ylabel("\it\rm_H_A / A"); grid on; 41 set(gca,'FontName','Times New Roman'); 42 set(gca,'FontSize',10); </pre> <p>第34行将仿真结果放大37/23 (1.6) 倍，以获取和实验结果相近的幅值</p>	<pre> 23 figure(2); 24 subplot(2,1,1); 25 plot(Test2IC1(:,1),Test2IC1(:,2),'color','#4c221b'); 26 27 DSIMIHVDC=csvread("DSIM-IC1.csv",1,0); 28 DSIMIHVDC(:,2)=(DSIMIHVDC(:,2)); 29 DSIMIHVDC(:,1)=(DSIMIHVDC(:,1))-0.6732; 30 subplot(2,1,2); 31 plot(DSIMIHVDC(:,1),DSIMIHVDC(:,2),'color','#3b2e7e'); 32 xlim([0,0.1]); 33 ylim([-50,50]); 34 xlabel("Time/s"); 35 ylabel("\it\rm_H_A / A"); grid on; 36 set(gca,'FontName','Times New Roman'); 37 set(gca,'FontSize',10); </pre>
<p>Fig. B2</p>	<p>实验结果</p> <p>篡改仿真结果后，与实验结果幅值非常接近!</p> <p>Eff修正仿真结果</p>	<p>实验结果</p> <p>篡改仿真结果前，仿真结果幅值不到实验结果的2/3不到</p> <p>Eff原始仿真结果</p>
<p>DrawCompare1 代码片段3</p>	<pre> 47 figure(3); 48 subplot(2,1,1); 49 plot(Test2IHVAC1(:,1),Test2IHVAC1(:,2),'color','#4c221b'); 50 xlim([0.75,0.77]); 51 ylim([-500,500]); 52 xlabel("Time/s"); 53 ylabel("\it\rm_D_A_B / A"); 54 set(gca,'FontSize',10); 55 56 DSIMIHVAC2=csvread("DSIM-IHVAC2.csv",1,0); 57 DSIMIHVAC2(:,2)=(DSIMIHVAC2(:,2))/6*405; 58 DSIMIHVAC2(:,1)=(DSIMIHVAC2(:,1))-0.1616*0.75; 59 subplot(2,1,2); 60 plot(DSIMIHVAC2(:,1),DSIMIHVAC2(:,2),'color','#3b2e7e'); 61 xlim([0.75,0.77]); 62 ylim([-500*6/405,500*6/405]); 63 xlabel("Time/s"); 64 ylabel("\it\rm_D_A_B / A"); grid on; 65 set(gca,'FontName','Times New Roman'); 66 set(gca,'FontSize',10); </pre> <p>第58行将仿真结果放大405/6 (67.5) 倍，以获取和实验结果相近的幅值</p>	<pre> 47 figure(3); 48 subplot(2,1,1); 49 plot(Test2IHVAC1(:,1),Test2IHVAC1(:,2),'color','#4c221b'); 50 xlim([0.75,0.77]); 51 52 DSIMIHVAC2=csvread("DSIM-IHVAC2.csv",1,0); 53 DSIMIHVAC2(:,2)=(DSIMIHVAC2(:,2)); 54 DSIMIHVAC2(:,1)=(DSIMIHVAC2(:,1))-0.1616*0.75; 55 subplot(2,1,2); 56 plot(DSIMIHVAC2(:,1),DSIMIHVAC2(:,2),'color','#3b2e7e'); 57 xlim([0.75,0.77]); 58 ylim([-500*6/405,500*6/405]); 59 xlabel("Time/s"); 60 ylabel("\it\rm_D_A_B / A"); grid on; 61 set(gca,'FontName','Times New Roman'); 62 set(gca,'FontSize',10); </pre>
<p>Fig. B3</p>	<p>实验结果</p> <p>篡改仿真结果后，与实验结果幅值范围一致!</p> <p>Eff修正仿真结果</p>	<p>实验结果</p> <p>篡改仿真结果前，与实验结果幅值范围相差约58倍</p> <p>Eff原始仿真结果</p>

	“学术不端”修改版本	原始版本
DrawCompare1 代码片段4	<pre> 70 figure(4); 71 subplot(2,1,1); 72 plot(Test2IHVAC1(:,1),Test2IHVAC1(:,2),'color','#4c221b'); 73 xlim([0.755 0.7555]); 74 ylim([-500 500]); 75 xlabel("Time/s"); 76 ylabel("I_{DAB} / A"); 77 set(gca,'FontSize',10); 78 set(gca,'FontSize',10); 79 80 subplot(2,1,2); 81 DSIMIHVAC2(:,2)=DSIMIHVAC2(:,2)*345/401; 82 plot(DSIMIHVAC2(:,1),DSIMIHVAC2(:,2),'color','#3b2e7e'); 83 xlim([0.755,0.755+0.0005]); 84 ylim([-500,500]); 85 xlabel("Time/s"); 86 ylabel("\it\rm D_AB / A"); grid on; 87 set(gca,'FontName','Times New Roman'); 88 set(gca,'FontSize',10); </pre> <p>第81行在代码片段3放大67.5倍后，进一步微调，将仿真结果缩小345/401 (0.86) 倍，以获取和实验结果相接近的幅值</p>	<pre> 70 figure(4); 71 subplot(2,1,1); 72 plot(Test2IHVAC1(:,1),Test2IHVAC1(:,2),'color','#4c221b'); 73 xlim([0.755 0.7555]); 74 ylim([-500 500]); 75 xlabel("Time/s"); 76 ylabel("I_{DAB} / A"); 77 set(gca,'FontSize',10); 78 set(gca,'FontSize',10); 79 80 subplot(2,1,2); 81 DSIMIHVAC2(:,2)=DSIMIHVAC2(:,2); 82 plot(DSIMIHVAC2(:,1),DSIMIHVAC2(:,2),'color','#3b2e7e'); 83 xlim([0.755,0.755+0.0005]); 84 ylim([-500*6/405/345*401,500*6/405/345*401]); 85 xlabel("Time/s"); 86 ylabel("\it\rm D_AB / A"); grid on; 87 set(gca,'FontName','Times New Roman'); 88 set(gca,'FontSize',10); </pre>
Fig. B4	<p>实验结果 X 0.755101 Y 345</p> <p>篡改仿真结果后，与实验结果幅值非常接近！ X 0.755112 Y 348.836</p> <p>Eff修正仿真结果</p>	<p>实验结果 X 0.755101 Y 345</p> <p>篡改仿真结果前，仿真结果幅值不到实验结果的1/68不到 X 0.755112 Y 6.95087</p> <p>Eff原始仿真结果</p>
DrawCompare1 代码片段5	<pre> 92 figure(5); 93 subplot(2,1,1); 94 plot(Test2YBLVDC(:,1),Test2YBLVDC(:,2),'color','#4c221b'); 95 xlim([0.03211 0.03211+0.00025]); 96 ylim([-2000,2000]); 97 xlabel("Time/s"); 98 ylabel("U_{HLLA} / A"); 99 set(gca,'FontSize',10); 100 set(gca,'FontSize',10); 101 102 DSIMYBLVDC=csvread("DSIM-YBLVDC.csv",1,0); 103 DSIMYBLVDC(:,2)=(DSIMYBLVDC(:,2))*1.01604; 104 105 DSIMYBLVDC(:,1)=DSIMYBLVDC(:,1)-0.0162874+0.03211; 106 subplot(2,1,2); 107 plot(DSIMYBLVDC(:,1),DSIMYBLVDC(:,2),'color','#3b2e7e'); 108 xlim([0.03211,0.03211+0.00025]); 109 ylim([-2000,2000]); 110 xlabel("Time/s"); 111 ylabel("\it\rm U_HLLA / A"); grid on; 112 set(gca,'FontName','Times New Roman'); 113 set(gca,'FontSize',10); </pre> <p>第103行将仿真结果放大1.01倍，以获取和实验结果基本一致的幅值</p>	<pre> 92 figure(5); 93 subplot(2,1,1); 94 plot(Test2YBLVDC(:,1),Test2YBLVDC(:,2),'color','#4c221b'); 95 xlim([0.03211 0.03211+0.00025]); 96 ylim([-2000,2000]); 97 xlabel("Time/s"); 98 ylabel("U_{HLLA} / A"); 99 set(gca,'FontSize',10); 100 set(gca,'FontSize',10); 101 102 DSIMYBLVDC=csvread("DSIM-YBLVDC.csv",1,0); 103 DSIMYBLVDC(:,2)=(DSIMYBLVDC(:,2)); 104 105 DSIMYBLVDC(:,1)=DSIMYBLVDC(:,1)-0.0162874+0.03211; 106 subplot(2,1,2); 107 plot(DSIMYBLVDC(:,1),DSIMYBLVDC(:,2),'color','#3b2e7e'); 108 xlim([0.03211,0.03211+0.00025]); 109 ylim([-2000,2000]); 110 xlabel("Time/s"); 111 ylabel("\it\rm U_HLLA / A"); grid on; 112 set(gca,'FontName','Times New Roman'); 113 set(gca,'FontSize',10); </pre>
Fig. B5	<p>实验结果 X 0.0322372 Y 760</p> <p>篡改仿真结果后，与实验结果幅值非常接近！ X 0.0322353 Y 759.814</p>	<p>实验结果 X 0.0322364 Y 760</p> <p>篡改仿真结果前，仿真结果幅值与实验结果仍有差距！ X 0.0322344 Y 747.831</p>
DrawCompare1 代码片段6	<pre> 116 figure(6); 117 % subplot(2,1,1); 118 plot(Test2YBLVDC(:,1),Test2YBLVDC(:,2),'color','#4c221b'); 119 hold on; 120 xlim([0.07 0.0707]); 121 ylim([-2000,2000]); 122 xlabel("Time/s"); 123 ylabel("\it\rm U_HLLA / A"); grid on; 124 set(gca,'FontName','Times New Roman'); 125 set(gca,'FontSize',10); 126 127 DSIMTR1=csvread("DSIM-TR-1.csv",1,0); 128 DSIMTR1(:,1)=(DSIMTR1(:,1))*1.6; 129 DSIMTR1(:,1)=(DSIMTR1(:,1))-DSIMTR1(1,1)+0.075074-0.000011*1.6+0.0000072; 130 plot(DSIMTR1(:,1),DSIMTR1(:,2),'color','#3b2e7e'); 131 legend('Experiment','Simulation'); 132 set(gca,'FontName','Times New Roman'); 133 set(gca,'FontSize',10); </pre> <p>第128行将仿真时间放大1.06倍，以获取和实验结果接近的动态时间 (129行额外增加0.0000072s以重新获得相同的动作起点)</p>	<pre> 116 figure(6); 117 % subplot(2,1,1); 118 plot(Test2YBLVDC(:,1),Test2YBLVDC(:,2),'color','#4c221b'); 119 hold on; 120 xlim([0.07 0.0707]); 121 ylim([-2000,2000]); 122 xlabel("Time/s"); 123 ylabel("\it\rm U_HLLA / A"); grid on; 124 set(gca,'FontName','Times New Roman'); 125 set(gca,'FontSize',10); 126 127 DSIMTR1=csvread("DSIM-TR-1.csv",1,0); 128 DSIMTR1(:,1)=(DSIMTR1(:,1)); 129 DSIMTR1(:,1)=(DSIMTR1(:,1))-DSIMTR1(1,1)+0.075074-0.000011*1.6+0.0000072; 130 plot(DSIMTR1(:,1),DSIMTR1(:,2),'color','#3b2e7e'); 131 legend('Experiment','Simulation'); 132 set(gca,'FontName','Times New Roman'); 133 set(gca,'FontSize',10); </pre>
	<p>Experiment</p>	<p>Experiment</p>



	“学术不端”修改版本	原始版本
02文件夹代码	<pre> 1 load('data2.mat'); 2 load('data2_DSED_ACDC3.mat'); 3 4 close all; 5 u_Sa23_exp=data2(:,3); 6 i_Sa2_exp=data2(:,4)*2; 7 ila_exp=data2(:,7); 8 t_i_Sa2_exp=1e-8*(0:1:(length(i_Sa2_exp)-1)); 9 10 delta_i_Sa2_exp=0; 11 12 delta_t_ 13 14 index_DS 15 & t_ 16 index_exp 17 & t_i_Sa2_exp<=delta_t_exp*0.02); 18 19 t_i_Sa2_exp=t_i_Sa2_exp(index_exp); 20 i_Sa2_exp=i_Sa2_exp(index_exp); 21 u_Sa23_exp=u_Sa23_exp(index_exp); 22 t_device_ACDC=t_device_ACDC(index_DSED); 23 i_Sa2_DSED=i_Sa2_DSED(index_DSED); 24 u_Sa23_DSED=u_Sa23_DSED(index_DSED); 25 26 27 28 index_e 29 & t_ 30 index_e 31 32 & t_i_Sa2_exp<=delta_t_exp*0.02); 33 delta_i_Sa2_exp=zeros(length(i_Sa2_exp),1); 34 fa=3; 35 fb=-1.5; 36 delta_i_Sa2_exp(index_exp_1)=(fb-fa)/0.01*(t_i_Sa2_exp(index_exp_1)... 37 -t_i_Sa2_exp(index_exp_1(1)))+fa; 38 fa=-1.5; 39 fb=6; 40 delta_i_Sa2_exp(index_exp_2)=(fb-fa)/0.01*(t_i_Sa2_exp(index_exp_2)... 41 -t_i_Sa2_exp(index_exp_2(1)))+fa; 42 delta_i_Sa2_exp=delta_i_Sa2_exp; 43 i_Sa2_exp=i_Sa2_exp+delta_i_Sa2_exp; 44 A=4; 45 i_Sa2_exp=i_Sa2_exp+A*sin(2*pi*50*(t_i_Sa2_exp(index_exp)... 46 -t_i_Sa2_exp(index_exp_1(1)))); 47 48 delta_u_Sa23_exp=zeros(length(u_Sa23_exp),1); 49 fa=2; 50 fb=-2; 51 delta_u_Sa23_exp(index_exp_1)=(fb-fa)/0.01*(t_i_Sa2_exp(index_exp_1)... 52 -t_i_Sa2_exp(index_exp_1(1)))+fa; 53 fa=-2; 54 fb=1; 55 delta_u_Sa23_exp(index_exp_2)=(fb-fa)/0.01*(t_i_Sa2_exp(index_exp_2)... 56 -t_i_Sa2_exp(index_exp_2(1)))+fa; 57 delta_u_Sa23_exp=delta_u_Sa23_exp; 58 u_Sa23_exp=u_Sa23_exp+delta_u_Sa23_exp; 59 Width=500; 60 61 figure(1); 62 yyaxis left 63 plot(t_i_Sa2_exp-delta_t_exp*10e-9,u_Sa23_exp,'b',... 64 t_de 65 'litt' 66 set(gca, 67 ylabel('litt/rms (50ns/div)'); 68 ylim([-50,200]); 69 set(gca,'yColor','r'); 70 yyaxis right 71 plot(t_i_Sa2_exp-delta_t_exp,i_Sa2_exp,'r',... 72 t_device_ACDC-delta_t_DSED,i_Sa2_DSED,'r--',... 73 'linewidth',1); 74 set(gca,'Fontname','Times New Roman'); 75 set(gcf,'position',[100,100,0.8*Width,0.5*Height]); 76 ylabel('litt/rms (50ns/div)'); 77 ylim([-50,200]); 78 set(gca,'yColor','r'); 79 legend('litt - Experiment','litt - PAT model',... 80 'litt - Experiment','litt - PAT model','litt (littight_b/rm)'); 81 legend('boxoff'); 82 xlabel('litt/rms (50ns/div)'); 83 xlim([0.00499591,0.00499693]); 84 set(gca,'xticklabel',[]); 85 grid on; grid minor; </pre>	<pre> 1 load('data2.mat'); 2 load('data2_DSED_ACDC3.mat'); 3 4 close all; 5 u_Sa23_exp=data2(:,3); 6 i_Sa2_exp=data2(:,4); 7 ila_exp=data2(:,7); 8 t_i_Sa2_exp=1e-8*(0:1:(length(i_Sa2_exp)-1)); 9 10 delta_i_Sa2_exp=0; 11 12 delta_t_ 13 14 index_DS 15 & t_ 16 index_exp 17 & t_i_Sa2_exp<=delta_t_exp*0.02); 18 19 t_i_Sa2_exp=t_i_Sa2_exp(index_exp); 20 i_Sa2_exp=i_Sa2_exp(index_exp); 21 u_Sa23_exp=u_Sa23_exp(index_exp); 22 t_device_ACDC=t_device_ACDC(index_DSED); 23 i_Sa2_DSED=i_Sa2_DSED(index_DSED); 24 u_Sa23_DSED=u_Sa23_DSED(index_DSED); 25 26 27 28 index_e 29 & t_ 30 index_e 31 32 & t_i_Sa2_exp<=delta_t_exp*0.02); 33 delta_i_Sa2_exp=zeros(length(i_Sa2_exp),1); 34 fa=3; 35 fb=-1.5; 36 delta_i_Sa2_exp(index_exp_1)=(fb-fa)/0.01*(t_i_Sa2_exp(index_exp_1)... 37 -t_i_Sa2_exp(index_exp_1(1)))+fa; 38 fa=-1.5; 39 fb=6; 40 delta_i_Sa2_exp(index_exp_2)=(fb-fa)/0.01*(t_i_Sa2_exp(index_exp_2)... 41 -t_i_Sa2_exp(index_exp_2(1)))+fa; 42 delta_i_Sa2_exp=delta_i_Sa2_exp; 43 i_Sa2_exp=i_Sa2_exp; 44 45 46 47 48 delta_u_Sa23_exp=zeros(length(u_Sa23_exp),1); 49 fa=2; 50 fb=-2; 51 delta_u_Sa23_exp(index_exp_1)=(fb-fa)/0.01*(t_i_Sa2_exp(index_exp_1)... 52 -t_i_Sa2_exp(index_exp_1(1)))+fa; 53 fa=-2; 54 fb=1; 55 delta_u_Sa23_exp(index_exp_2)=(fb-fa)/0.01*(t_i_Sa2_exp(index_exp_2)... 56 -t_i_Sa2_exp(index_exp_2(1)))+fa; 57 delta_u_Sa23_exp=delta_u_Sa23_exp; 58 u_Sa23_exp=u_Sa23_exp; 59 Width=500; 60 61 figure(1); 62 yyaxis left 63 plot(t_i_Sa2_exp-delta_t_exp*10e-9,u_Sa23_exp,'b',... 64 t_de 65 'litt' 66 set(gca, 67 ylabel('litt/rms (50ns/div)'); 68 ylim([-50,200]); 69 set(gca,'yColor','r'); 70 yyaxis right 71 plot(t_i_Sa2_exp-delta_t_exp,i_Sa2_exp,'r',... 72 t_device_ACDC-delta_t_DSED,i_Sa2_DSED,'r--',... 73 'linewidth',1); 74 set(gca,'Fontname','Times New Roman'); 75 set(gcf,'position',[100,100,0.8*Width,0.5*Height]); 76 ylabel('litt/rms (50ns/div)'); 77 ylim([-50,200]); 78 set(gca,'yColor','r'); 79 legend('litt - Experiment','litt - PAT model',... 80 'litt - Experiment','litt - PAT model','litt (littight_b/rm)'); 81 legend('boxoff'); 82 xlabel('litt/rms (50ns/div)'); 83 xlim([0.00499591,0.00499693]); 84 set(gca,'xticklabel',[]); 85 grid on; grid minor; </pre>
	<p>第6行将实验数据直接扩大一倍，以得到和仿真结果相接近的幅值</p>	<p>数据翻倍</p>
	<p>第43行通过累加delta值对实验数据进行修正，并在第44-46行直接使用sin函数来增加实验结果的波动效果，以将实验结果尽可能与仿真结果吻合</p>	<p>数据修正</p>
<p>第58行通过累加delta值对实验数据进行修正，以将实验结果尽可能与仿真结果吻合</p>	<p>数据修正</p>	





解决效果

通过以上努力，我彻底解决了损耗计算中仿真结果与实验结果不一致的底层问题。进一步地，通过专业绘图软件将matlab中处理后的数据画出，其中Fig.B1-B8分别对应期刊论文的Fig.15的(a)-(5)中，同时将其也写在我的博士论文中。

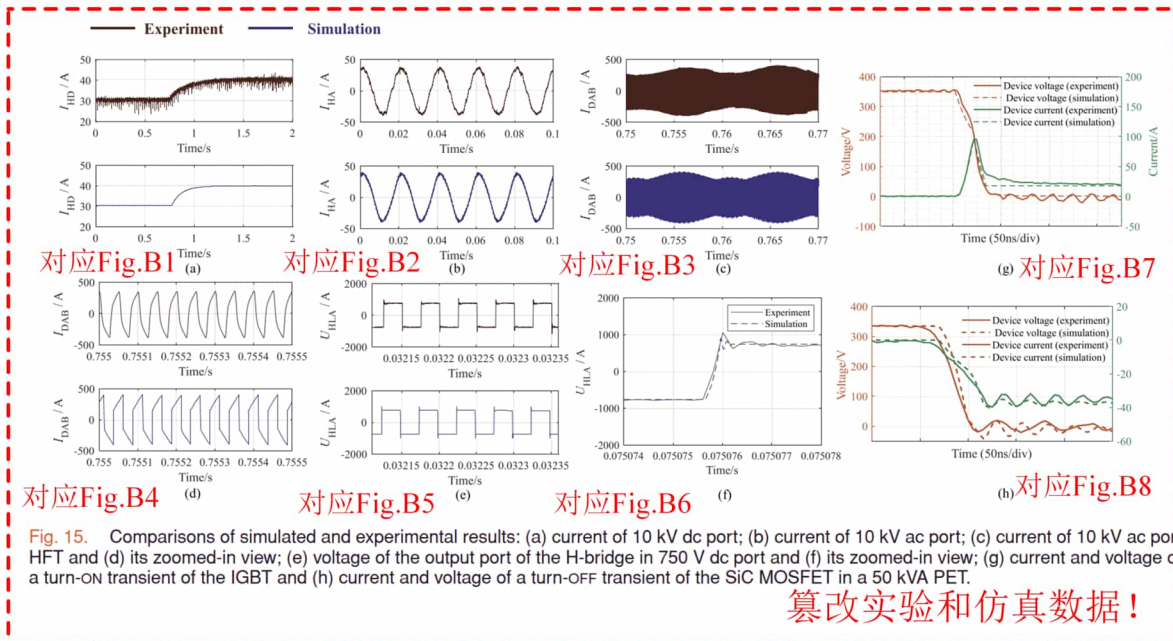


Fig. 15. Comparisons of simulated and experimental results: (a) current of 10 kV dc port; (b) current of 10 kV ac port; (c) current of 10 kV ac port HFT and (d) its zoomed-in view; (e) voltage of the output port of the H-bridge in 750 V dc port and (f) its zoomed-in view; (g) current and voltage of a turn-ON transient of the IGBT and (h) current and voltage of a turn-OFF transient of the SiC MOSFET in a 50 kVA PET.

it is hardly possible to use them in this megawatt case study composed of more than 500 switching devices and hundreds of H-bridges. The major concern is the convergence problems. Therefore, a system-level commercial tool with ideal switch model, which is more suitable for large-system design and complicated control design in practical applications, is selected. But the comparisons with this commercial software only attest to the accuracy of the proposed method in terms of system-level dynamics. The simulated results are also compared with experimental results to verify the transient results. The photograph of the experimental prototype is shown in Fig. 14. A load change of the 10-kV dc port is tested, with a step change of the power flow from 300 to 400 kW. The current of the 10-kV dc port is shown in Fig. 15(a), defined as I_{HD} , and the current of the 10-kV ac port is shown in Fig. 15(b), defined as I_{HA} . The HFT current in 10 kV ac stage, namely, the dual-active-bridge (DAB) current I_{DAB} , is shown in Fig. 15(c), and Fig. 15(d) is the zoomed-in view. Finally, the output voltage U_{HLA} of the H-bridge in the DAB in 380 V ac port is shown in Fig. 15(e), which consists of the device-level switching transients, with the zoomed-in comparison presented in Fig. 15(f). In general, the simulated results are in good agreement with the experimentally measured ones.

Fig. 15(a)–(f) only shows the transient results of the device voltage because it is very hard to measure the device current in the real prototype of a high-power converter. As a result, switching transient simulations are also performed on a smaller system: a 50-kVA PET as a smaller portion of the studied 2 MW PET [35], [42]. The 50-kVA PET consists of 16 IGBTs and eight SiC MOSFETs. The detailed structure of the 50-kVA PET can be found in [35]. The results are compared in Fig. 15(g) and (h), which also show good agreement.

V. SYSTEM EFFICIENCY EVALUATION BASED ON THE PROPOSED METHOD

With the fast simulation speed and the ability to capture switching transients, the proposed method enables the in-depth analysis of the PET. To further demonstrate the value of the proposed method in practical development and research, one representative application, namely, the evaluation of the system efficiency is studied. As an energy conversion system, ensuring high efficiency is always of essential significance. But the efficiency of the system is strongly dependent on the operational conditions. To accurately simulate the efficiency curve, the real control strategies must be implemented in the simulation, the real structure of the system must be modeled, and the switching transients which can lead to substantial switching losses must be simulated. Therefore, the proposed method offers a possibility to accurately and efficiently simulate the efficiency curve during the design stage.

Here, we first discuss the general loss distribution of a power electronics system. Generally, the input power of the converter P_{in} equals the sum of the output power P_{out} and the total loss P_{loss} . Components that contribute to P_{loss} include ON-state loss of the semiconductor switches P_{on} , switching loss of the switches P_{sw} , copper loss of the transformers P_{Cu} , iron loss of the transformer P_{Fe} , loss of the equivalent series resistance (ESR) P_{ESR} , and the additional loss P_0 . They can be classified into fixed loss P_{fixed} , which is irrelevant of the load current, switching loss P_{sw} , which is proportional to the load current, and resistive loss P_R , which is proportional to the square of the load current [43]. Therefore, it can be deduced that a typical efficiency curve exhibits a convex feature shown in Fig. 16. Under light load, the fixed loss P_{fixed} contributes to a big proportion in the total loss; therefore, the efficiency is low. Under heavy load,

小结

综上所述我在这篇文章中存在以下问题:

在清华大学预防与处理学术不端行为办法中:

*第二十二条 在科学研究及相关活动中有下列行为之一的,应当认定为构成学术不端行为:

(三) 伪造科研数据、资料、文献、注释，或者捏造事实、编造虚假研究成果；

04 THSA应用文章 (Q2期刊TCAS-1)

除了上述三个代表作外，为了快速不费力地能够有更多的论文，我选择通过更换算例来水论文，例如这篇论文，Event-Driven Approach With Time-Scale Hierarchical Automaton for Switching Transient Simulation of SiC-Based High-Frequency Converter，是将上述的PAT模型重新应用在一个新的系统上，论文全文可通过点击[链接](#)获得。

问题概述

通过对上述三篇核心支撑文章的讲解后，大家不难看出，我的PAT模型和仿真结果要想和实验对得上，只能依靠篡改实验数据。所以这篇文章也不例外，为了将PAT模型和其他结果相吻合，我当然也对仿真数据进行了“捏造和篡改”。我相信大家通过上述三篇文章已经基本掌握了篡改数据的方法，那么为了节约篇幅，下面我只展示这篇文章一个图的“学术不端流程”，以凸显我进行“学术不端”的广泛性。

下面我将以论文中的Fig. 10(f-g)图作为例子，来详细说明代码修改的地方，并将修改前后的结果进行对比。详细的数据处理代码和验证流程可以在[Code for THSA](#)中找到。

	“学术不端”修改版本	原始版本
Code01	<pre> 19 %% Transient data 20 21 transient_dsim=importdata('DSIM_MAIN_400us_VdsId2.txt'); 22 tt_d = transient_dsim.data(:,1) * 1e3; 23 Id_d = transient_dsim.data(:,2); 24 Vds_d = transient_dsim.data(:,3); 25 26 transient_dsim3=importdata('DSIM_MAIN_400us_VdsId3.txt'); 27 %transient_dsim3.data(5693,3)=25; 28 tt_d3 = transient_dsim3.data(:,1) * 1e3; 29 Id_d3 = transient_dsim3.data(:,2); 30 Vds_d3 = transient_dsim3.data(:,3); 31 32 % i = find(tt_d3 > 1.586915231e-1); 33 % 34 % tt_d3(i)=tt_d3(i)+0.00025e-1; 35 36 transient_spice=importdata('BWT_SPICE_400us_maxstep0.1n_transient2.txt'); 37 tt_s = transient_spice.data(:,1) * 1e3; 38 Id_s = transient_spice.data(:,3); 39 Vds_s = transient_spice.data(:,2); </pre> <p>直接将仿真结果有问题的点重新赋值</p>	<pre> 19 %% Transient data 20 21 transient_dsim=importdata('DSIM_MAIN_400us_VdsId2.txt'); 22 tt_d = transient_dsim.data(:,1) * 1e3; 23 Id_d = transient_dsim.data(:,2); 24 Vds_d = transient_dsim.data(:,3); 25 26 transient_dsim3=importdata('DSIM_MAIN_400us_VdsId3.txt'); 27 %transient_dsim3.data(5693,3)=25; 28 tt_d3 = transient_dsim3.data(:,1) * 1e3; 29 Id_d3 = transient_dsim3.data(:,2); 30 Vds_d3 = transient_dsim3.data(:,3); 31 32 % i = find(tt_d3 > 1.586915231e-1); 33 % 34 % tt_d3(i)=tt_d3(i)+0.00025e-1; 35 36 transient_spice=importdata('BWT_SPICE_400us_maxstep0.1n_transient2.txt'); 37 tt_s = transient_spice.data(:,1) * 1e3; 38 Id_s = transient_spice.data(:,3); 39 Vds_s = transient_spice.data(:,2); </pre>
Code02	<pre> 49 yyaxis left; 50 plot(tt_d * 1e3, Vds_d, 'color', mycolor(5,:), 'linewidth', LineWidth, 'linestyle', '-'); 51 plot(tt_s * 1e3-0.008, Vds_s, 'color', mycolor(5,:), 'linewidth', LineWidth, 'linestyle', '-'); 52 ylabel('V_{ds} (V)', 'fontname', 'Times New Roman', 'FontSize', 14, 'Interpreter', 'latex'); 53 ylim([-50 400]); 54 yyaxis right; 55 plot(tt_d * 1e3, Id_d, 'color', mycolor(4,:), 'linewidth', LineWidth, 'linestyle', '-'); 56 plot(tt_s * 1e3-0.008, Id_s, 'color', mycolor(4,:), 'linewidth', LineWidth, 'linestyle', '-'); 57 ylabel('I_d (A)', 'fontname', 'Times New Roman', 'FontSize', 14, 'Interpreter', 'latex'); 58 59 xlabel('Time (μs)', 'fontname', 'Times New Roman', 'FontSize', 14, 'Interpreter', 'latex'); 60 %legend(['V_{ds} ED', 'V_{ds} SPICE', 'I_d ED', 'I_d SPICE'], 'fontname', 'Times New Roman', 'FontSize', 14, 'Interpreter', 'latex'); 61 62 xlim([152.7 152.9]); </pre> <p>将仿真结果直接扩大1.1倍</p>	<pre> 49 yyaxis left; 50 plot(tt_d * 1e3, Vds_d, 'color', mycolor(5,:), 'linewidth', LineWidth, 'linestyle', '-'); 51 plot(tt_s * 1e3-0.008, Vds_s, 'color', mycolor(5,:), 'linewidth', LineWidth, 'linestyle', '-'); 52 ylabel('V_{ds} (V)', 'fontname', 'Times New Roman', 'FontSize', 14, 'Interpreter', 'latex'); 53 ylim([-50 400]); 54 yyaxis right; 55 plot(tt_d * 1e3, Id_d, 'color', mycolor(4,:), 'linewidth', LineWidth, 'linestyle', '-'); 56 plot(tt_s * 1e3-0.008, Id_s, 'color', mycolor(4,:), 'linewidth', LineWidth, 'linestyle', '-'); 57 ylabel('I_d (A)', 'fontname', 'Times New Roman', 'FontSize', 14, 'Interpreter', 'latex'); 58 59 xlabel('Time (μs)', 'fontname', 'Times New Roman', 'FontSize', 14, 'Interpreter', 'latex'); 60 %legend(['V_{ds} ED', 'V_{ds} SPICE', 'I_d ED', 'I_d SPICE'], 'fontname', 'Times New Roman', 'FontSize', 14, 'Interpreter', 'latex'); 61 62 xlim([152.7 152.9]); </pre>
Code03	<pre> 73 plot(tt_d3 * 1e3, Vds_d3, 'color', mycolor(5,:), 'linewidth', LineWidth, 'linestyle', '-'); 74 plot(tt_s * 1e3-0.005, Vds_s, 'color', mycolor(5,:), 'linewidth', LineWidth, 'linestyle', '-'); 75 ylabel('V_{ds} (V)', 'fontname', 'Times New Roman', 'FontSize', 14, 'Interpreter', 'latex'); 76 ylim([-50 400]); 77 yyaxis right; 78 plot(tt_d3 * 1e3, Id_d3, 'color', mycolor(4,:), 'linewidth', LineWidth, 'linestyle', '-'); 79 plot(tt_s * 1e3-0.005, Id_s, 'color', mycolor(4,:), 'linewidth', LineWidth, 'linestyle', '-'); 80 ylabel('I_d (A)', 'fontname', 'Times New Roman', 'FontSize', 14, 'Interpreter', 'latex'); 81 82 xlabel('Time (μs)', 'fontname', 'Times New Roman', 'FontSize', 14, 'Interpreter', 'latex'); 83 %legend(['V_{ds} ED', 'V_{ds} SPICE', 'I_d ED', 'I_d SPICE'], 'fontname', 'Times New Roman', 'FontSize', 14, 'Interpreter', 'latex'); 84 85 xlim([158.6 158.9]); </pre> <p>将仿真结果直接扩大1.2倍</p>	<pre> 73 plot(tt_d3 * 1e3, Vds_d3, 'color', mycolor(5,:), 'linewidth', LineWidth, 'linestyle', '-'); 74 plot(tt_s * 1e3-0.005, Vds_s, 'color', mycolor(5,:), 'linewidth', LineWidth, 'linestyle', '-'); 75 ylabel('V_{ds} (V)', 'fontname', 'Times New Roman', 'FontSize', 14, 'Interpreter', 'latex'); 76 ylim([-50 400]); 77 yyaxis right; 78 plot(tt_d3 * 1e3, Id_d3, 'color', mycolor(4,:), 'linewidth', LineWidth, 'linestyle', '-'); 79 plot(tt_s * 1e3-0.005, Id_s, 'color', mycolor(4,:), 'linewidth', LineWidth, 'linestyle', '-'); 80 ylabel('I_d (A)', 'fontname', 'Times New Roman', 'FontSize', 14, 'Interpreter', 'latex'); 81 82 xlabel('Time (μs)', 'fontname', 'Times New Roman', 'FontSize', 14, 'Interpreter', 'latex'); 83 %legend(['V_{ds} ED', 'V_{ds} SPICE', 'I_d ED', 'I_d SPICE'], 'fontname', 'Times New Roman', 'FontSize', 14, 'Interpreter', 'latex'); 84 85 xlim([158.6 158.9]); </pre>
Fig. C1	<p>如果将实验电流乘1.1倍, 难以和仿真结果接近</p> <p>将仿真结果直接扩大1.1倍</p> <p>如果不将实验电流乘1.2倍, 难以和仿真结果接近</p>	<p>如果将实验电流乘1.1倍, 难以和仿真结果接近</p> <p>将有问题点重新赋值</p> <p>如果不将实验电流乘1.2倍, 难以和仿真结果接近</p>

解决效果

通过以上努力，我彻底解决了损耗计算中仿真结果与实验结果不一致的底层问题。进一步地，通过专业绘图软件将matlab中处理后的数据画出，Fig.C1对应期刊论文的Fig. 10(f-g)中，同时将其也写在我的博士论文中。

SHI et al.: EVENT-DRIVEN APPROACH WITH TSHA FOR SWITCHING TRANSIENT SIMULATION OF

4755

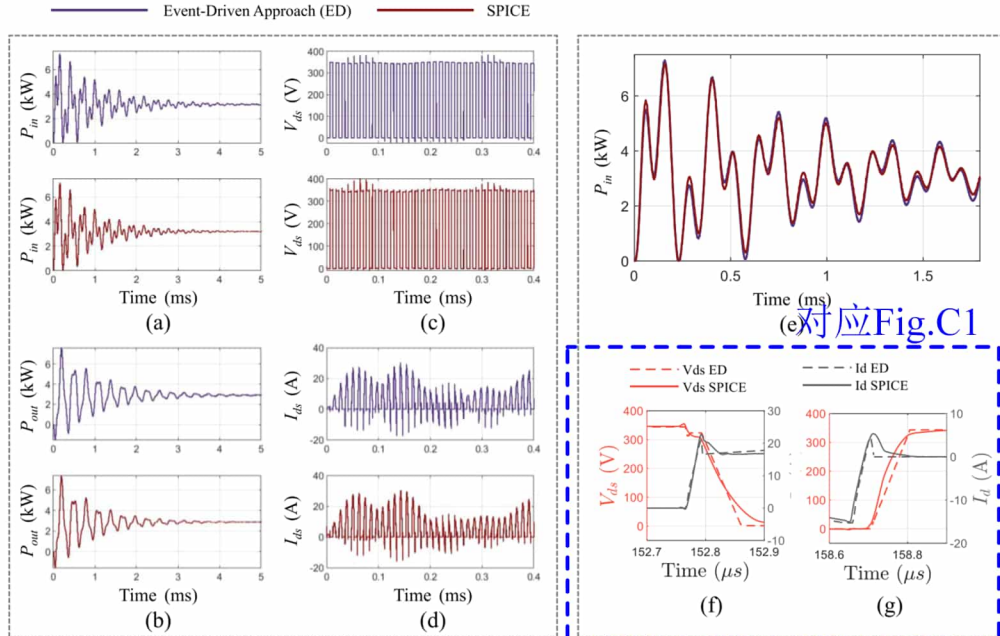


Fig. 10. Comparisons of simulated waveforms of the proposed event-driven approach (ED) (purple, top) and LTspice[®] (red, bottom) of the BWPT system with open-loop control strategy. (a) Input power P_{in} (0-5 ms). (b) Output power P_{out} (0-5 ms). (c) Voltage drop of S_{11} in the transmitting converter $V_{ds,S11}$ (0-400 μs). (d) Current flowing through S_{11} in the transmitting converter $I_{d,S11}$ (0-400 μs). (e) Zoomed-in view of the input power. (f) Turn-on switching transient waveforms. (g) Turn-off switching transient waveforms.

篡改实验和仿真数据！

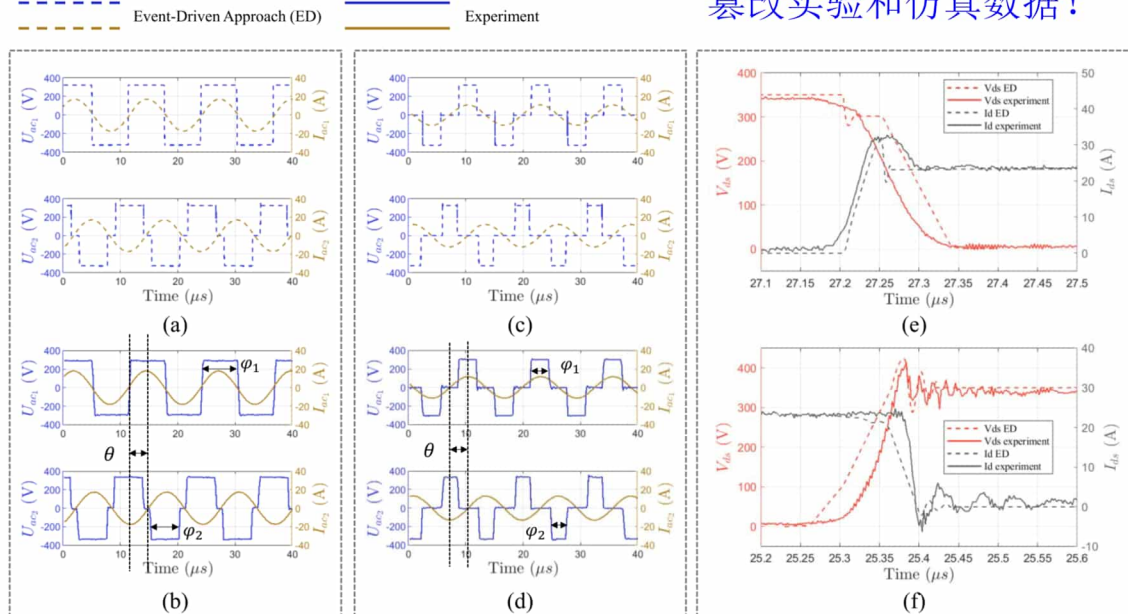


Fig. 11. Comparisons between simulated waveforms of the proposed event-driven approach (ED) (dash lines) and experimental waveforms (solid lines). (a) Simulated waveforms of ac voltage and current U_{ac1} , I_{ac1} of transmitting converter and ac voltage and current U_{ac2} , I_{ac2} of receiving converter when $P_{ref} = 3.3$ kW. (b) Experimental waveforms of U_{ac1} , I_{ac1} , U_{ac2} , I_{ac2} when $P_{ref} = 3.3$ kW. (c) Experimental waveforms of U_{ac1} , I_{ac1} , U_{ac2} , I_{ac2} when $P_{ref} = 1.5$ kW. (d) Experimental waveforms of U_{ac1} , I_{ac1} , U_{ac2} , I_{ac2} when $P_{ref} = 1.5$ kW. (e) Turn-on switching transient waveforms. (f) Turn-off switching transient waveforms.

小结

综上我在这篇文章中存在以下问题：

在[清华大学预防与处理学术不端行为办法](#)中：

*第二十二条 在科学研究及相关活动中有下列行为之一的，应当**认定为构成学术不端行为**：

(三) **伪造科研数据、资料、文献、注释，或者捏造事实、编造虚假研究成果**；

05 三组脉冲文章 (Q1期刊ESTPE)

问题概述

上面四篇文章中，我主要遇到**预期结果不准确**的问题。我所使用的“数据捏造和篡改”方法（主要包含对数据结果进行删减，捏造，篡改等手段），相信大家已经学会了。下面我将用另一篇论文为例，来解决第二个问题--**论文成果不够多**的问题。那么大家可能有疑问，你不可以继续使用相同的方法换算例来水吗？答案是不行的，因为你相同的内容重复多了，审稿人会疲劳。你看我最开始发的都是顶刊 TPEL, TIE，后面由于顶刊审稿人疲劳了，我只能发差一点的 TCAS-1 期刊，并最后只能发开源的 IEEE Access 了。所以仅靠这种方法是不可持续的。那么我教大家一个小妙招。看看自己课题组已经毕业的师兄师姐是否有没发表的成果，如果没有的话，那这个小妙招就不适用了。如果有的话，那么恭喜您，又可以喜提文章了。像我就是，将之前毕业师兄的博士论文的第三章，直接翻译成英文，发表在期刊 [IEEE JOURNAL OF EMERGING AND SELECTED TOPICS IN POWER ELECTRONICS](#) 上，论文题目是 Time-Domain and Frequency-Domain Analysis of SiC MOSFET Switching Transients Considering Transmission of Control, Drive, and Power Pulses。论文全文可通过点击[链接](#)获得。师兄博士论文全文可通过点击[链接](#)获得。

解决效果

为了方便大家理解，我将对[论文](#)进行网页翻译，并和师兄博士论文进行对比，翻译的不好的地方，大家请多担待：

我一作的英文期刊论文

IEEE JOURNAL OF EMERGING AND SELECTED TOPICS IN POWER ELECTRONICS, VOL. 9, NO. 5, OCTOBER 2021 6441

Time-Domain and Frequency-Domain Analysis of SiC MOSFET Switching Transients Considering Transmission of Control, Drive, and Power Pulses

Bochen Shi¹, Graduate Student Member, IEEE, Zhengming Zhao¹, Fellow, IEEE, Yicheng Zhu¹, Member, IEEE, and Xudong Wang¹

Abstract—Three types of pulses, namely the control, drive, and power pulses, coexist in power electronics systems. The transmission of them embodies the idea to control energy flow with signal flow. However, due to the nonideal performance of the semiconductor switches and the parasitic elements, significant delay and distortion are inevitable during the transmission, causing severe challenges in terms of both device- and system-level performance. Taking silicon carbide (SiC) MOSFET-based system as an example, this article studies the transmission of the three pulses. Time-domain studies are provided first to derive the characteristic parameters of the delay and distortion. Based on the time-domain expressions, a pulse decomposition method is proposed to study the frequency spectrum of the power pulse considering all major transient factors. Experimental results are provided to verify the proposed method and the acquired results. Based on the analyses, the impact of pulse delay and distortion on system performance is summarized, and the general idea of active gate controlling for the power pulse is briefly discussed. This article provides quantitative studies and relevant discussions from the perspective of pulse transmission to improve the analysis, gate-drive design, and active gate control of switching transient.

Index Terms—Double-pulse test, electromagnetic pulse, oscillation, silicon carbide (SiC) MOSFET, switching transient.

I. INTRODUCTION

THE fundamental principle of power electronics is to control energy flow with signal flow, with the transmission of the electromagnetic pulses from signal pulsewidth modulation (PWM) through the gate driver toward the corresponding power PWM [1]. The control pulse (signal PWM) represents the desired control information, while the power pulse (power PWM) is the real actuator in energy conversion which follows the control information. In an ideal situation, the control strategy can be perfectly implemented and the power PWM is equivalent to the control PWM. Unfortunately,

Manuscript received September 29, 2020; revised December 30, 2020; accepted January 25, 2021. Date of publication January 28, 2021; date of current version October 1, 2021. This work was supported by the Major Program of National Natural Science Foundation of China under Grant 51490680 and Grant 51490683. Recommended for publication by Associate Editor Hanyong Chu. (Corresponding author: Zhengming Zhao.)
The authors are with the Department of Electrical Engineering, Tsinghua University, Beijing 100084, China (e-mail: shibo@sem.tsinghua.edu.cn; zhaomz@sem.tsinghua.edu.cn; wzd13@mails.tsinghua.edu.cn).
Color versions of one or more figures in this article are available at <https://doi.org/10.1109/JESTPE.2021.3055145>.
Digital Object Identifier 10.1109/JESTPE.2021.3055145

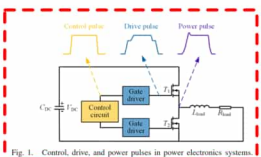


Fig. 1. Control, drive, and power pulses in power electronics system.

despite the continuous development of semiconductor technology, nonideal switching transients are still inevitable for power switches [2]–[5], and parasitic elements always exist in gate drive circuits and power circuits [6]–[8]. These all contribute to delay and distortion during the transmission from control pulse to drive and power pulses, as shown in Fig. 1.

The existence of delay and distortion during pulse transmission leads to deviation of the power pulse waveform from the original desired controlling, and therefore, causes serious challenges in terms of both device- and system-level performance. For example, transient voltage spikes lead to the potential breakdown of the semiconductor device [2], [5], and dead-time intensifies the output distortion and increases total harmonic distortion (THD) [12], [13]. To address these challenges, detailed research should be performed to study the transmission of control, drive, and power pulses, to characterize the delay and distortion between them, to determine the impact on device and system performance, and as a final target, to actively control the transmission process so that the power pulse behaves as desired.

Related studies have been conducted from the following two aspects: 1) investigations on the transient behavior of power semiconductor devices and 2) active gate control (AGC) methods of power pulses. Studies that fall into the former category include modeling, analysis, and suppression of switching transient induced electromagnetic interference (EMI) [14]–[16], evaluations of gate loop oscillation and its impact on stability [10], [17], [19]–[21], modeling and investigations on switching loss [9], [19]–[21], studies on dead-time effect and its compensation [12], [13], and suppression

师兄的博士论文第三章

第3章 三组脉冲关系的规律研究

第3章 三组脉冲关系的规律研究

上一章通过实验和建模的方法对电磁能量脉冲的瞬态行为进行了分析。本章则重点分析电力电子系统中控制脉冲，到驱动脉冲再到电磁能量脉冲的相互关系和传递规律，以揭示三组脉冲关系对系统性能的影响规律。首先，分别从时域和频域对三组脉冲关系进行表征。通过时域和频域表征，可揭示出影响三组脉冲关系的主要因素及三组脉冲关系与系统性能之间的定量关系。利用该定量关系，可以分析系统中不同因素对脉冲传递规律及系统性能的影响规律。最后，结合典型案例介绍了三组脉冲关系的时域、频域表征在定量分析系统性能方面的应用研究。

3.1 三组脉冲关系的时域表征

在电力电子系统中，控制器输出控制脉冲，经驱动电路后产生驱动脉冲，作用于功率半导体器件后，产生电磁能量脉冲，如图 3.1 所示。从控制器输出的控制脉冲一般可视为理想的矩形波脉冲，原因是控制脉冲的上升沿和下降沿的时间尺度为纳秒级，与脉宽（一般为微秒级~十微秒级）相比可以忽略。从控制脉冲到驱动脉冲及电磁能量脉冲，除了传递过程中的延迟外，在脉冲形态属性上，相比控制脉冲，驱动脉冲和电磁能量脉冲会产生畸变。所产生的畸变包括时间尺度增加至十纳秒~百纳秒级的上升沿和下降沿，驱动脉冲的米勒平台效应及电磁能量脉冲的尖峰及振荡等瞬态开关特性，其原因可归结为器件结电容的非线性及回路杂散电感的影响。

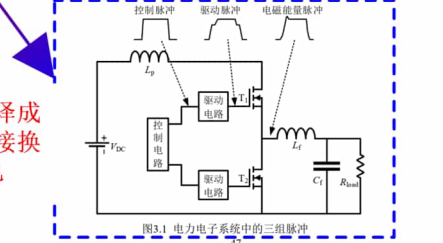


图3.1 电力电子系统中的三组脉冲

原图翻译成英文直接换颜色

我一作的英文期刊论文

IEEE JOURNAL OF EMERGING AND SELECTED TOPICS IN POWER ELECTRONICS, VOL. 9, NO. 5, OCTOBER 2021

of crosstalk between upper and lower switches in a phase-leg configuration [11], [22]. These studies offer analytical methodologies, and discussions from different perspectives regarding switching transient, and provide insights into the physical processes. However, they mainly focus on specific transient issues instead of an overall analysis and study of the transmission process of the three pulses. Another group of research focuses on the AGC methods for insulated gate power semiconductors [23]–[33], where the switching transients can be actively controlled to fulfill the desired control target. But there lacks an in-depth study on the transmission of the delay and distortion on system performance during the transmission, which is necessary to support the evaluation and design of AGC methods.

To fill this gap, this article provides theoretical and experimental studies on the transmission of the three pulses. The studies are based on silicon carbide (SiC) MOSFET as one of the most promising wide bandgap semiconductor device offering better switching performance, including low conduction resistance, decreased switching loss, increased junction operating temperature, and high switching speed, but at the same time, with more prominent parasitic inductance switching transients, especially more serious oscillations. The contributions of this article include the following:

- 1) A perspective from the transmission of the three types of pulses is provided, and quantitative analyses to characterize the delay and distortion during the transmission are presented.
- 2) A pulse decomposition method is proposed to analyze the frequency spectrum considering the delay and distortion during switching transients.
- 3) A bridge between the time-domain/frequency-domain analyses and the design of AGC methods is provided by in-depth discussions and experimental verifications.

The rest of this article is organized as follows. Both time-domain studies (Section II) and frequency-domain studies (Section III) are performed to quantitatively characterize the relationship between the control, drive, and power pulses. After that, in Section IV, the impact of the delay and distortion on the device- and system-level performance is summarized, and how the above analyses support the evaluation and design of AGC methods is discussed. Finally, conclusions are drawn in Section V.

II. TIME-DOMAIN STUDIES

Time-domain analyses are first provided to study the delay and distortion between the three pulses. The studies are based on the double-pulse circuit shown in Fig. 2, which represents the basic unit in power electronics systems. A SiC MOSFET and a SiC Schottky barrier diode (SBD) is used as a switch pair. The parasitic elements considered include gate-loop inductance L_g , power loop inductance L_p , common source inductance L_s , gate-source capacitance C_{gs} , drain-source capacitance C_{ds} , Miller capacitance C_{gd} , diode junction capacitance C_j , and power-loop resistance R_p . The corresponding

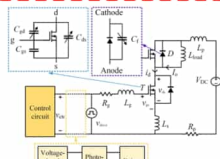


Fig. 2. Double-pulse test circuit and the parasitic elements considered in the

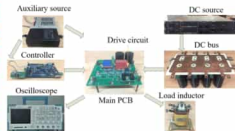


Fig. 3. Experimental platform for the studies

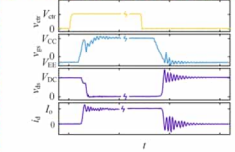


Fig. 4. Typical waveforms of the control, drive, and power pulses from double-pulse experimental tests.

experimental platform is shown in Fig. 3. Discrete devices SiC MOSFET CMF20120D and SiC SBD C4D30120D are tested in the experiments. Typical experimental waveforms from double-pulse tests are shown in Fig. 4, where v_{gs} , v_{ds} , and i_d symbolize the control pulse, the drive pulse, the voltage waveform of the power pulse, and the current waveform of the power pulse, respectively. It can be observed that significant delay and distortion exist between the pulses, which are discussed separately in Section II-A–II-C.

师兄的博士论文第三章

第3章 三组脉冲关系的规律研究

因此，对三组脉冲关系的研究即为对三组脉冲间延迟和畸变关系进行研究。研究的第一步，即对三组脉冲关系的认识和表征。接下来，首先从时域上对三组脉冲关系进行表征。

3.1.1 三组脉冲关系的时域参数表征

图 3.2 (a) 为双脉冲电路的原理图，从双脉冲电路得到的三组脉冲的典型实验波形如图 3.2 (b) 所示，实验所用器件为 SiC MOSFET 及 SiC SBD。

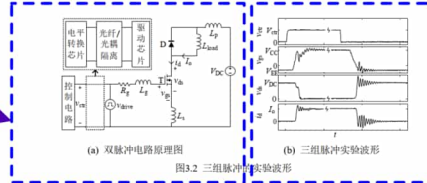


图 3.2 三组脉冲实验波形

原图翻译成英文直接换颜色

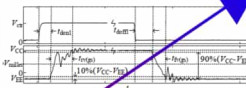


图 3.3 从控制脉冲到驱动脉冲的延迟和畸变关系表征

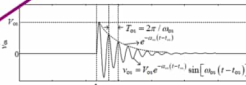


图 3.4 脉冲衰减振荡的一般表征方法

第 5 章 实验平台设计

第 5 章 实验平台设计

为了研究电磁能量脉冲的形态属性及三组脉冲间的传递规律，设计了针对 SiC MOSFET 及 SiC SBD 的双脉冲测试平台。另外，本文也对脉冲组合规律在电力电子功率放大器中的应用进行了研究，并设计了电力电子功率放大器的实验平台进行分步验证。接下来，对两个实验平台的设计细节进行介绍。

5.1 双脉冲测试电路的实验平台设计

双脉冲测试电路的原理框图和实验平台照片分别如图 5.1 和图 5.2 所示。其中双脉冲测试主电路的原理图及实物图已在 2.2.1 节中进行了介绍。接下来，本节主要对双脉冲测试电路实验平台的设计细节进行介绍。

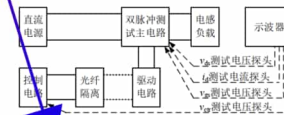


图 5.1 双脉冲测试电路的原理框图



图 5.2 双脉冲测试电路实验平台

- 用文本框盖住中文
- 图都不需要自己画了

原图直出

我一作的英文期刊论文

SiB et al., TIME-DOMAIN AND FREQUENCY-DOMAIN ANALYSIS OF SiC MOSFET SWITCHING TRANSIENTS

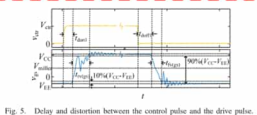


Fig. 5. Delay and distortion between the control pulse and the drive pulse.

where V_{th} is the turn-on threshold gate voltage, and $V_{ds,off}$ is the Miller voltage determined by load current and MOS transconductance g_m . It is worth noting that for fast-switching transient with lower gate resistance, the gate-loop inductances can have a high impact and (2) can be inaccurate.

B. Distortion Between Gate Control Pulse and Power Pulse

The distortion between the gate control pulse and the power pulse, as illustrated in Fig. 6, can be characterized with rise/fall time, voltage/current spikes, and oscillations. In Fig. 6, the distortion due to rising/falling process of the power pulses is described by t_{r1} , t_{f1} (voltage) and t_{r2} , t_{f2} (current). According to the SiC MOSFET switching transient model in [20], analytic expressions of the voltage fall time and the current rise time are derived as

$$\begin{aligned}
 t_{r1} &= t_{r1} + t_{r2} \\
 t_{f1} &= -Bt_0 + \sqrt{B^2 - 4A_0C_0} \\
 t_{r2} &= R_2(C_{gs} + C_{gd}) \left(\sqrt{V_{ds,off} - V_{gs1}} \right) + C_{gs} R_2 / 2 \\
 t_{f2} &= \frac{2I_0}{V_{CC} - V_{gs1} - V_{ds,off}} + C_{gd} R_2 / 2
 \end{aligned}$$

师兄的博士论文第三章

第 3 章 三组脉冲关系的规律研究

因此，对三组脉冲关系的研究即为对三组脉冲间延迟和畸变关系进行研究。研究的第一步，即对三组脉冲关系的认识和表征。接下来，首先从时域上对三组脉冲关系进行表征。

3.1.1 三组脉冲关系的时域参数表征

图 3.2 (a) 为双脉冲电路的原理图，从双脉冲电路得到的三组脉冲的典型实验波形如图 3.2 (b) 所示，实验所用器件为 SiC MOSFET 及 SiC SBD。



Fig. 1. Delay between pulses and the common plate and the power pulses.

A. Delay Between Pulses

Delay between the three pulses is discussed first. The transmission from the control pulse to the drive pulse is illustrated in Fig. 5. The rise time and the fall time of the control pulse are usually of or less than the nanosecond-level time scale, and are hence ignored in this article. So the control pulse can be approximately regarded as an idea square wave. The delay time from control to drive pulse is denoted as t_{d0} and t_{doff} for turn-on and turn-off processes, respectively. They are mainly due to the delay of logic chips, isolation circuits (photo-coupler or optical fiber), and driving chips. t_{d0} and t_{doff} are generally independent of the parameters in the power circuits (e.g., dc-bus voltage, load current, etc.), but instead dependent on the temperature of the chips/isolators. Experimental measurements can be performed to determine the corresponding delays.

The transmission from the control pulse to the power pulses (voltage and current) is illustrated in Fig. 6. The delay time is defined as

$$\begin{cases} t_{d0} = t_{d01} + t_{d02} \\ t_{doff} = t_{doff1} + t_{doff2} \end{cases} \quad (1)$$

where t_{d01} and t_{doff1} are the delay time between the drive pulse and the power pulse, coinciding with the definitions in the manufacturer's datasheet [34]. These delays are dependent on the gate-loop parameters. With relatively large gate resistance and relatively slower switching transients, the gate charging/discharging processes and the variations of the gate current during the delays are slower. Therefore, with the assumption of ignoring the gate-loop parasitic inductances [20], analytical expressions of the delay time can be given as

$$\begin{cases} t_{d0} = R_g(C_{gs} + C_{gd}(V_{GS} = V_{GS0})) \frac{V_{GS} - V_{GS0}}{V_{GS} - V_{GS0}} \\ t_{doff} = R_g(C_{gs} + C_{gd}(V_{GS} = 0)) \frac{V_{GS} - V_{GS0}}{V_{GS} - V_{GS0}} \end{cases} \quad (2)$$

6444

IEEE JOURNAL OF EMERGING AND SELECTED TOPICS IN POWER ELECTRONICS, VOL. 9, NO. 5, OCTOBER 2021

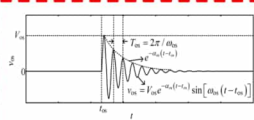


Fig. 7. General mathematical form of damped sine waveform to describe the damping ringing during switching transient.

TABLE I CHARACTERISTIC PARAMETERS OF THE DAMPED OSCILLATIONS

Amplitude V_m (or I_m)	Frequency ω_{osc}	Damping α_{osc}
Turn-on current oscillation	$\sqrt{\frac{L_{loop}}{C_{gs}}}$	$\frac{R_g}{2L_{loop}}$
Turn-off voltage oscillation	$\sqrt{\frac{L_{loop}}{C_{gd}}}$	$\frac{R_g}{2L_{loop}}$
Turn-off current oscillation	$\sqrt{\frac{L_{loop}}{C_{gs} + C_{gd}}}$	$\frac{R_g}{2L_{loop}}$

Such practical designs are not considered in the analysis for simplicity. Similarly, the load current (I_L in Fig. 2) is also considered as constant.

With the assumptions, the oscillations can be described by damped sine function. The general form is shown in Fig. 7, where V_m (or I_m for current waveform) is the amplitude, ω_{osc} is the frequency, T_m is the time period, and α_{osc} is the damping ratio. Components involved in the turn-on oscillation are the diode capacitance C_j and the power loop stray inductance, while for the turn-off oscillation, the components are MOSFET capacitance C_{gs} and C_{gd} together with the power loop stray inductance. From the equivalent circuit shown in Fig. 2, the characteristic parameters describing the oscillations can be derived and summarized in Table I, where $L_{loop} = L_g + L_s$, R_{loop} is the on-state resistance of the SiC MOSFET, and $R_{gs(on)}$ is the on-state resistance of the SiH. For simplifications, the transistor in the upper switch and the diode in the lower switch are ignored here, under the direction of I_L shown in Fig. 2. If taking them into consideration, the extra junction capacitance should be added into the amplitude and frequency expressions, as described in Section III-B.

Equations (3)-(5) and Table I provide quantitative expressions of the time-domain distortion (rise/fall time, spikes, and oscillations) between the control pulse and the power (voltage and current) pulse. These expressions are derived based on the switching transient models proposed in [20], where the accuracy of the model has been experimentally verified [20, Fig. 9], which also attests to the accuracy of these expressions. To further analyze the distortion between the control and power pulses, experiments are performed to see how different parameters (junction capacitances, stray inductances, and gate drive resistances) affect the distortion

388 et al.: TIME-DOMAIN AND FREQUENCY-DOMAIN ANALYSIS OF SiC MOSFET SWITCHING TRANSIENTS

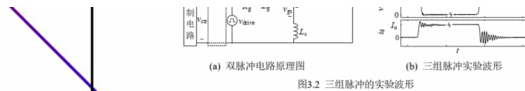


Fig. 3.2. Three-pulse experimental waveform

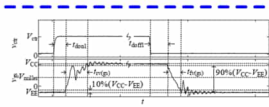


Fig. 3.3. Relationship between delay and distortion from control pulse to drive pulse

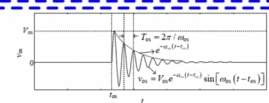


Fig. 3.4. General expression method for pulse attenuation oscillation

where the definitions of the coefficients of the junction capacitance characteristics including C_{gs} and C_{gd} , and the linear transconductance coefficient of the MOSFET denoted as g_m , can be found in [20]. The spikes are denoted as peak voltage V_{peak} and peak current I_{peak} . The expressions are given as [20]

$$\begin{cases} V_{peak} \approx V_{DC} + (L_g + L_s) |di/dt|_{off} \\ I_{peak} \approx I_L + \sqrt{dQ/dt} |di/dt|_{off} \end{cases} \quad (5)$$

where dQ is the charge accumulated in C_j during the turn-on process, $|di/dt|_{on}$ and $|di/dt|_{off}$ are the average changing rate of I_L during turn-on current rising and turn-off current falling stage.

To study the oscillations, assumptions of the following discussions are clarified first. Both the studied circuit (Fig. 2) and the experimental setup in this article focus on discrete devices rather than power modules. Parasitic elements inside the middle-point inductors are not considered. M_{tr} is considered in Fig. 2 constant during the switch decoupling capacitors as they can also participate.

原图直出

拿来主义

(rise/fall time and voltage/current spikes). The experimental results are summarized in Fig. 8.

Generally, increasing the junction capacitances C_{gs} , C_{gd} , and C_j will slow down the switching transient and therefore increase the rise/fall time of the current/voltage pulse. A difference is that increasing C_{gs} mainly leads to the suppression of the current spike, while increasing C_{gd} mainly suppresses the voltage spike of v_{gs} . For C_{gs} and C_j , they do not directly participate in the gate charging/discharging process, so the impact can be different. The variation of C_m mainly affects the voltage rise time during the turn-off transient, the current rising hump and therefore C_{gs} has a limit.

And for the voltage falling, theoretically the discharging of C_{gs} will influence the fall time. The nonlinear characteristics of the junction capacitances can be the reason of a higher impact of C_{gs} on the turn-off than the turn-on transient. As for the spikes, increasing C_{gs} and C_{gd} will suppress the voltage spike, but meanwhile increase the current spike.

The stray inductances introduced from device package, connections, assembling, and cables, L_g , L_s , and L_{tr} as shown in Fig. 2 are considered and tested. The power loop inductance L_s mainly affects the turn-off voltage spike. On the contrary, increasing the common source inductance L_g significantly increases the rise/fall time, while decreases the current/voltage spikes (within the testing range of the L_g). For gate inductance L_g , the current spike increases with the increase of the gate inductance, but considering that in practical applications, the gate driver is usually close to the devices and L_g is usually around 10 nH, such an impact can be ignored.

For the gate resistance R_g , it influences the charging/discharging speed of the gate capacitors. Therefore, the rise/fall time increases with the increase of R_g , meanwhile the voltage/current spikes decrease. This large range variation of all the main parameters (time and spikes) when changing R_g offers an opportunity to actively control the switching transients by online adjusting of the gate circuits, which will be discussed in Section IV.

It is worth mentioning that the studies and experiments in this article are based on the double-pulse test circuit and the corresponding experimental platforms as shown in Figs. 2 and 3, which do not take into account some of the nonideal factors in real power converters and prototypes that may affect the transmission of the pulses. In [37], several nonideal factors in PWM inverters including the load characteristics, the long cables, the multiple phases, and the coupling between SiC MOSFET and heat sink is studied. It is highlighted that these factors potentially lead to slower switching performance, such as slower switching speed, higher switching loss, and more series oscillations, or in other words, more serious distortion between the pulses. The in-depth studies of these factors are critical to real applications, but fall beyond the scope of this article.

C. Distortion Between Gate Control Pulse and Drive

Similarly, for the drive pulse shown in Fig. 5, the e can be characterized as rise/fall time $t_{r(on)}$ and $t_{f(off)}$, etc.

$$\begin{cases} V_{peak} = V_{DC} + L_{loop} |di/dt|_{off} \\ I_{peak} \approx I_L + \sqrt{dQ/dt} |di/dt|_{off} \end{cases} \quad (3-1)$$

4. 电压、电流振荡, 同样用衰减正弦函数来表征. 其参数表征如表 3.1 所示.

表 3.1 电磁能量脉冲振荡的参数表征

振荡幅值 V_m (或 I_m)	振荡频率 ω_{osc}	衰减系数 α_{osc}	
开通电流振荡	$\sqrt{dQ/dt} di/dt _{off}$	$1/\sqrt{L_{loop} C_j}$	$(R_g + R_{gs(on)})/2L_{loop}$
关断电压振荡	$L_{loop} di/dt _{off}$	$1/\sqrt{L_{loop} (C_{gs} + C_{gd})}$	$(R_g + R_{ds(on)})/2L_{loop}$
关断电流振荡	$(C_{gs} + C_{gd}) L_{loop} di/dt _{off}$	$1/\sqrt{L_{loop} (C_{gs} + C_{gd})}$	$(R_g + R_{ds(on)})/2L_{loop}$

3.1.2 驱动脉冲的振荡行为分析

在上一章中, 以 SiC MOSFET 为对象提出了开关瞬态分析模型, 通过该模型可以对上述三组脉冲的主要延迟和畸变关系进行定量分析. 然而, 为了简化模型计算, 所提分析模型并未考虑驱动脉冲 v_{gs} 的振荡. 考虑到驱动脉冲的振荡在 SiC MOSFET 开关过程中更为显著, 容易引起关断器件误动作, 进而引入稳定性问题, 所以, 接下来重点对 SiC MOSFET 中驱动脉冲的振荡现象进行分析.

同样以图 3.2 (a) 所示的双脉冲测试电路作为研究对象, 与驱动脉冲有关的等效电路如图 3.6 (a) 所示, 称为驱动脉冲的单电源等效电路模型. 考虑到该模型并未考虑主电路对驱动脉冲产生影响, 即 $C_{gd}dv_{ds}/dt$ 效应和 $L_{tr}di/dt$ 效应, 因此需要将单电源等效电路模型扩展至图 3.6 (b) 所示的三电源等效电路模型.

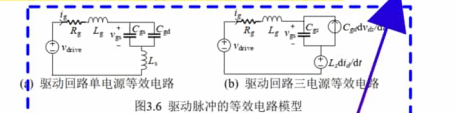


Fig. 3.6. Equivalent circuit model for the drive pulse

由三电源等效电路可知, 当电磁能量脉冲发生电压振荡或电流振荡时, 会通过 $C_{gd}dv_{ds}/dt$ 及 $L_{tr}di/dt$ 效应, 将振荡引入驱动回路, 进而引起驱动电压振荡. 因此结合等效电路分析, 可以得到开通和关断过程中 v_{gs} 振荡阶段的时域参数, 如 (3-2) 和 (3-3) 所示.

拿来主义

中文直译 (工作量最大的部分)

为了研究驱动脉冲振荡, 栅极驱动等效电路 (图 2 的一部分) 如图 9 (a) 所示. 这是一个单源电路, 适用于研究驱动脉冲的延迟和上升/下降阶段, 例如 (2) 的推导. 然而, 在振荡级中, 电源环路振荡可以通过两种机制耦合到栅极环路中 [18]: 米勒电容 C_{gd} 和公共源电感 L_s . 图 9 (b) 所示的三源电路可以更好地考虑这两种效应. 该电路意味着, 即使栅极环路本身处于欠阻尼状态, 即 $R_g^2(C_{gs} + C_{gd}) > 4L_g$, 电源环路振荡仍可通过 C_{gd} 和 L_s 进入栅极环路 (这通常是导致驱动脉冲振荡的主要因素), 因此威胁到稳定性.

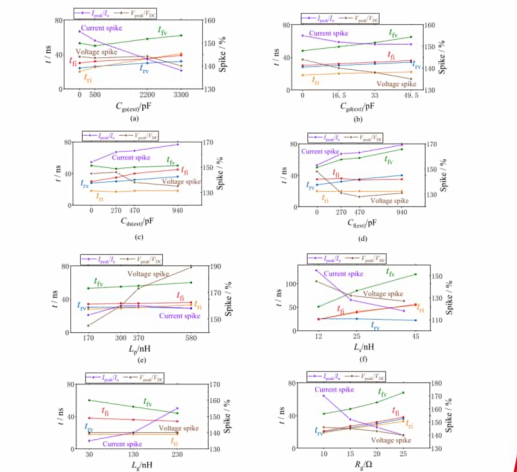


Fig. 8. Experimental results of how different parameters affect the distortion (rise/fall time and voltage/current spikes) between the control and the power pulses, including (a-d) stray inductances, (e-f) gate drive effect, and the oscillations. For SiC MOSFET, due to small junction capacitance and faster switching speed, the Miller plateau is not apparent. Instead, more visible oscillations can be observed. The oscillation is of significant concern in gate drive design as it potentially leads to erroneous operation of semiconductor device, especially considering the smaller gate threshold voltage $V_{GS(th)}$ of SiC MOSFET.

To study the drive pulse oscillations, the gate drive equivalent circuit (a portion of Fig. 2) is illustrated in Fig. 9(a). This is a single-source circuit and suitable for the study of the delay and rise/fall stages of the drive pulse, for example, the derivation of (2). However, in the oscillation stages, power loop oscillations can be coupled into the gate

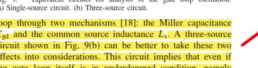


Fig. 9. (a) Single-source equivalent circuit. (b) Three-source equivalent circuit.

$R_{gs} + C_{gs} > 4\tau_{on}$, the power loop oscillations can still be introduced through C_{gd} and L_s into the gate loop (which is more often than not the dominating factor contributing to the drive pulse oscillations) and therefore threaten the stability.

SPICE simulations and double-pulse experiments are performed with Cree SiC MOSFET CM20120D and SiC SBD C4D30120D to study the impact of different gate drive parameters on gate pulse oscillations. As shown in Fig. 10, the simulated and experimental results are not perfectly identical but they exhibit consistent trends. In general, the amplitude of the oscillation decreases with the increase of R_g and C_{gs} while it increases with the increase of C_{gd} . However, the increase of R_g has a limited impact on the oscillations due to two opposite effects: decreased V_{gs} and I_{gs} of the power pulse, while increased R_g hence stronger coupling between the gate and power loop (dI/dt). Comprehensively speaking, the variation of R_g has a restricted impact on the suppression of gate pulse oscillation. Based on these results, from the perspective of gate-loop design, increasing R_g , adopting SiC MOSFET with higher C_{gs} ratio, or adding external parallel gate-source capacitance are effective approaches to suppress the drive pulse oscillations and avoid spurious operations of the device.

翻译: 使用Cree SiC MOSFET CM20120D和SiC SBD C4D30120D进行SPICE仿真和双脉冲实验,以研究不同栅极驱动参数对栅极脉冲振荡的影响。如图10所示,仿真结果和实验结果并不完全相同,但趋势一致。一般来说,振荡的幅度随着 R_g 和 C_{gs} 的增加而减小,而增加 L_s 由于两个相反的作用,对振荡的影响有限:降低 V_{gs} 和 I_{gs} 的功率脉冲,同时增加 L_s 因此,栅极和电源回路之间的耦合变强(dI/dt)。综合来说,变化 L_s 对栅极脉冲振荡的抑制影响有限。基于这些结果,从门环设计的角度来看,增加 R_g 、采用SiC MOSFET更高 C_{gs} /Ced比率或增加外部并联栅源电容是抑制驱动脉冲振荡和避免器件杂项操作的有效方法。

where R represents R_{gs} , 25°C , T_{J1} and T_{J2} are the device datasheet. The cc the equations of (7) and curves from the device d between T_J and device p

Tips: 可以直接将博士论文中图的中文用英文文本框盖住(盖住部分与原图的清晰度不同)

III. FREQUENCY-DOMAIN STUDIES

In Section II, the time-domain expressions of the power pulses are derived, including delay (described by delay time) and distortion (described by rise/fall and damping sine functions). Based on the time-domain expressions, frequency-domain studies can be performed to investigate the frequency-related performance such as output THD and EMI. A pulse decomposition method is proposed in this section to quantitatively study the frequency-domain characteristics of

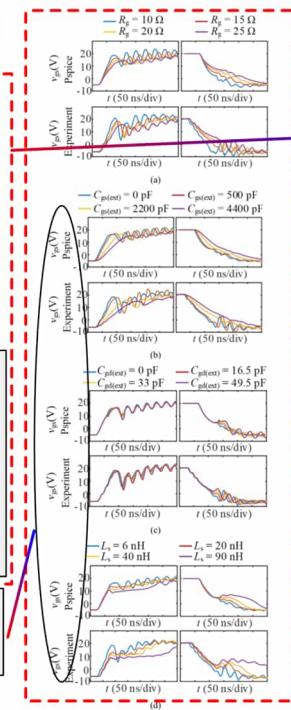


Fig. 10. Comparisons of drive pulses under different gate drive parameters. The turn-on transient is on the left, and the turn-off on the right. (a) Impact of R_g . (b) Impact of C_{gs} . (c) Impact of C_{gd} . (d) Impact of L_s .

the power pulses, considering all major impacts during switching transient including dead-time, delay, rise/fall, and oscillation. With the frequency-domain studies, more comprehensive

中文直译 (工作量最大的部分)

原图直接截图,无需自己动手

从公式(3-2)和(3-3)可以看出,驱动脉冲振荡的频率和衰减系数与电磁能量脉冲的振荡频率一致,而振荡幅值则受电磁能量脉冲幅值 I_m 或 V_m 及驱动回路参数 R_g , C_{gs} , C_{gd} 及 L_s 影响。通过 Pspice 仿真及双脉冲实验结果,图3.7展示了主要驱动回路参数 R_g , C_{gs} , C_{gd} 及 L_s 对驱动脉冲振荡过程的影响。可以看到,在驱动脉冲的波形轨迹上,仿真和实验结果存在一定的偏差。这主要是由于实验测量结受探头引入的杂散电感及器件内部栅极和源极杂散电感影响,而 PSpice 仿真结果并未考虑这一因素。从影响规律方面,仿真和实验结果相一致,即驱动脉冲的振荡幅值随着 C_{gs} 的增加而增加,随着 R_g 及 C_{gd} 的增加而减小,而 L_s 主要影响驱动脉冲的振荡频率。一方面,增加 L_s 会抑制开关过程中 dI/dt , 进而抑制电磁能量脉冲的振荡幅值 I_m 和 V_m 。另一方面,增加 L_s 也会使 dI/dt 对驱动脉冲振荡的影响更显著。综合两方面因素,通过改变 L_s 对驱动回路振荡进行控制的效果有限。

因此,通过对驱动回路的振荡过程进行等效电路分析,揭示了影响驱动回路振荡幅值的主要参数,并结合仿真和实验分析,总结了主要驱动回路参数对驱动电压振荡过程的影响规律。从设计层面,为了提高驱动稳定性角度,增加 R_g , 选择高 C_{gs} 比例的 SiC MOSFET 或者在栅源极并联外部电容,是抑制驱动回路振荡的有效方法。

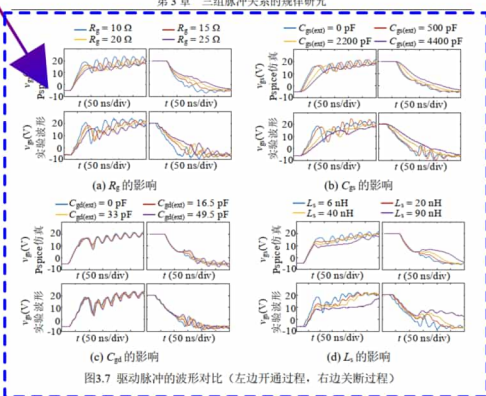


图3.7 驱动脉冲的波形对比(左边开通过程,右边关断过程)

3.2 三组脉冲关系的频域表征

在上一节中,从时域上对三组脉冲形态属性关系进行了定量表征,同时也将三组脉冲关系与系统性能(如电压、电流应力,开关损耗)联系起来。然而其他性能如系统输出 THD、EMI 等性能则与脉冲的频域特征有关。为了更全面地分析三组脉冲规律与系统性能之间的相互关系,本节重点分析控制脉冲与电磁能量脉冲在频域上的关系,在此基础上,分析不同延迟和畸变参数对于电磁能量脉冲频谱和系统性能的影响规律。

分析对象为半桥电路,所比较的控制脉冲和电磁能量脉冲如图3.8所示。将两个脉冲进行归一化处理后,所比较的控制脉冲可视为理想电磁能量脉冲,而所研究的实际电磁能量脉冲选择为桥臂输出脉冲,即桥臂下管的管压降,用 V_{leg} 表示,相应的频域表达式为 $V_{leg}(f)$ 。桥臂输出脉冲序列的频谱特性会受到调制频率 T_m 、开关频率 T_s 、占空比 D 、死区 t_d 、开通关断延迟和开关过渡过程(包括电压上升和下降时间及电压振荡)的影响。

分析的控制脉冲和功率脉冲如图11所示。控制脉冲 v_{ctr} 可以算是理想的方法。所研究的功率脉冲是半桥的输出电压脉冲,即下部开关的漏源电压,表示为 v_{leg} 在时域和 $V_{leg}(f)$ 在频域中。其频谱取决于调制频率 T_m 、开关频率 f_s (切换周期 $T_s = 1/f_s$)、占空比 D 、死区时间 t_d 、导通/关断延迟、上升/下降时间和电压振荡。

在现有文献中,类似的方法已被用于分析有死区的PWM脉冲和PWM脉冲[39],但忽略了开关瞬态。在以下各部分中,综合考虑了死区时间、延迟时间和瞬态过程,以研究输出电压脉冲的频谱。为了方便起见,控制脉冲和功率脉冲经过归一化。

原图直出

中文直译

分析对象为半桥电路,所比较的控制脉冲和电磁能量脉冲如图3.8所示。将两个脉冲进行归一化处理后,所比较的控制脉冲可视为理想电磁能量脉冲,而所研究的实际电磁能量脉冲选择为桥臂输出脉冲,即桥臂下管的管压降,用 V_{leg} 表示,相应的频域表达式为 $V_{leg}(f)$ 。桥臂输出脉冲序列的频谱特性会受到调制频率 T_m 、开关频率 T_s 、占空比 D 、死区 t_d 、开通关断延迟和开关过渡过程(包括电压上升和下降时间及电压振荡)的影响。

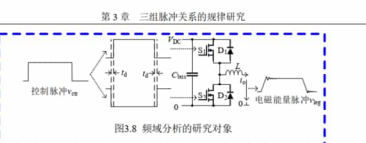


图3.8 频域分析的研究对象

目前对脉冲进行频域分析的方法主要有直接FFT分析法,双重傅里叶积分法和脉冲分解法。其中直接FFT分析法需要首先通过仿真建模得到脉冲波形,再通过FFT计算其频谱。该方法简化了求解频域过程的数学推导,但仿真建模及FFT计算都会影响求解速度,计算精度也受仿真步长的影响。双重傅里叶积分法适合于分析周期性调制所得到的脉冲的频谱,其相较于FFT计算的优点是提供脉冲频谱的解析解,但其缺点是通用性不强[20]。而脉冲分解法是通过将脉冲进行分解,求分解后各个脉冲的傅里叶变换,叠加得到整个脉冲的频谱,是一种对脉冲频谱的直接计算方法,不依赖于周期性调制方法,通用性更强[20]。基于脉冲分解的频域分析方法是利用了傅里叶变换的线性特性[20],如(3-4)所示。

$$\mathcal{F}\left[\sum_{n=1}^N A_n f(t)\right] = \sum_{n=1}^N A_n \mathcal{F}(f(t)) \quad (3-5)$$

目前,已有文献基于脉冲分解法,主要对理想PWM脉冲[20]及含有死区的PWM脉冲[20]频谱进行了分析,并未考虑脉冲延迟和畸变的影响。接下来,本节将以半桥电路输出电磁能量脉冲序列为研究对象,综合考虑死区、延迟及开关过渡过程对输出脉冲频谱的影响。为了简化分析,对输出脉冲序列进行归一化处理,即

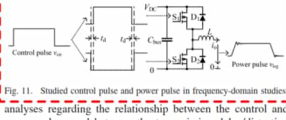


Fig. 11. Studied control pulse and power pulse in frequency-domain studies analyses regarding the relationship between the control and

中文直译

中文直译

power pulses, and between the transmission delay/transition and system performance can be provided.

The analyzed control pulse and power pulse are illustrated in Fig. 11. The control pulse u_{in} can be regarded as an ideal square wave. The studied power pulse is the output voltage pulse of the half bridge, namely the drain-source voltage of the lower switch, denoted as v_{ds} in time-domain and $V_{ds}(f)$ in frequency-domain. Its frequency spectrum is dependent on modulation frequency f_m , switching frequency f_s (switching period $T_s = 1/f_s$), duty cycle D , dead-time t_d , turn-on/off delay, rise/fall time, and voltage oscillation. Here we only focus on PWM and assume a constant switching frequency of the converter for simpler derivations of the frequency-domain analytical expressions. Other modulations such as pulse frequency modulation (PFM) and pulse amplitude modulation (PAM) and more advanced variable-frequency control strategies are beyond the scope of this article.

The studies are performed based on pulse decomposition, guaranteed by the linearity of the Fourier transformation, as shown in the following equation:

$$\mathcal{F}\left[\sum_{i=1}^N A_i f_i(t)\right] = \sum_{i=1}^N A_i F_i(\omega). \quad (9)$$

In the available literature, similar methods have been used to analyze ideal PWM pulses and PWM pulses with dead-time [9], however, ignoring the switching transient. In the following parts, dead-time, delay time, and transient process are comprehensively considered to study the frequency spectrum of the output voltage pulse. The control and power pulses are normalized for convenience.

A. Frequency Spectrum of Ideal Power Pulse

When ignoring dead-time, delay, and switching transient, namely, studying an ideal power pulse, the frequency spectrum will be identical to that of the control pulse. Such a situation is studied first in this section. A PWM pulse, taking trailing-edge PWM (TEPWM) as an example [40], can be decomposed into a square wave with 50% duty cycle, defined as p_{CTE} , plus a pulse sequence related to the modulation signal, defined as p_{CTE} .

$$b_{pCTE}(t) = p_{CTE}(t) + p_{CTE}(t). \quad (10)$$

The time-domain and frequency-domain expressions of p_{CTE} are given as

$$p_{CTE}(t) = \sum_{k=-\infty}^{\infty} [u(t-kT_s) - u(t-kT_s - T_s/2)] \quad (11)$$

$$p_{CTE}(f) = \sum_{k=-\infty}^{\infty} \frac{2}{j(2k+1)} \delta[f - (2k+1)f_s] \pm \pi \delta(f) \quad (12)$$

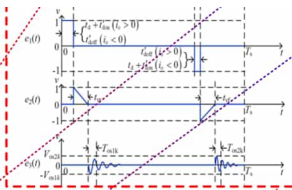


Fig. 12. Decomposition of the power pulse.

where u is the unit step function and δ is the unit impulse function. The time-domain and frequency-domain expressions of p_{CTE} are given as

$$p_{CTE}(t) = \sum_{k=-\infty}^{\infty} \left[u\left(t - kT_s + \frac{1}{2}T_s\right) - u\left(t - kT_s - T_s\right) \right] \quad (13)$$

$$p_{CTE}(f) = \sum_{k=-\infty}^{\infty} \left[\frac{2}{j(2k+1)} e^{-j2\pi f(kT_s + T_s/2)} - e^{-j2\pi f(kT_s - T_s)} \right], f \neq 0$$
$$= \sum_{k=-\infty}^{\infty} \left(\tau_k - \frac{T_s}{2} \right), f = 0$$

where τ_k is the pulsewidth of the PWM pulse in the k th period. Then the frequency spectrum of ideal power pulse can be calculated with

$$b_{pCTE}(f) = p_{CTE}(f) + p_{CTE}(f). \quad (15)$$

B. Frequency Spectrum of Real Power Pulse

The impact of dead-time and delay, rise/fall time, and oscillation in real power pulse can be described with $e_1(t)$, $e_2(t)$, and $e_3(t)$, respectively, as shown in Fig. 12. $e_1(t)$ is a rectangular pulse between ± 1 describing dead-time and delay. $e_2(t)$ is a sawtooth pulse between ± 1 describing rise/fall time. $e_3(t)$ is a damping sine pulse describing oscillation.

Considering all these nonideal factors, the final expression of the output voltage pulse is given as

$$b_{pRT}(t) = p_{CTE}(t) + p_{CTE}(t) + e_1(t) + e_2(t) + e_3(t). \quad (16)$$

认为输出脉冲的幅值在 0, 1 之间。

3.2.1 理想电磁能量脉冲的频谱分析

不考虑死区、延迟和开关过渡过程时，理想电磁能量的频谱特性和控制脉冲的频谱特性一致。对任意一 PWM 信号，可分解为占空比为 50% 的方波信号叠加一个与调制信号有关的脉冲序列^[9]。以下以降沿单边调制 PWM (Trailing-edge PWM, TEPWM) 为例，进行分析，有

$$v_{dsRT}(t) = p_{CTE}(t) + p_{CTE}(t) \quad (3-6)$$

其中 $p_{CTE}(t)$ 的表达式及其傅里叶变换为

53

第三章 三相脉冲关系的规律研究

$$p_{CTE}(t) = \sum_{k=-\infty}^{\infty} [u(t-kT_s) - u(t-kT_s - T_s/2)] \quad (3-7)$$

$$p_{CTE}(f) = \sum_{k=-\infty}^{\infty} \frac{2}{j(2k+1)} \delta[f - (2k+1)f_s] \pm \pi \delta(f) \quad (3-8)$$

与调制信号有关的项 $p_{CTE}(t)$ 的表达式和傅里叶变换为

$$p_{CTE}(t) = \sum_{k=-\infty}^{\infty} \left[u\left(t - kT_s + \frac{1}{2}T_s\right) - u\left(t - kT_s - T_s\right) \right] \quad (3-9)$$

$$p_{CTE}(f) = \sum_{k=-\infty}^{\infty} \left[\frac{1}{j2\pi f} \left(e^{-j2\pi f(kT_s + T_s/2)} - e^{-j2\pi f(kT_s - T_s)} \right) \right], f \neq 0$$
$$= \sum_{k=-\infty}^{\infty} \left(\tau_k - \frac{T_s}{2} \right), f = 0$$

其中 τ_k 为第 k 个开关周期的控制脉冲的脉宽。因此，对于一般性的调制信号，理想电磁能量脉冲的频谱为

$$v_{dsRT}(f) = p_{CTE}(f) + p_{CTE}(f) \quad (3-11)$$

3.2.2 实际电磁能量脉冲的频谱分析

与理想电磁能量脉冲相比，实际电磁能量脉冲要考虑死区、延迟及开关过渡过程的影响。分别用脉冲 $e_1(t)$, $e_2(t)$ 和 $e_3(t)$ 来表征这些非理想因素的影响，如图 3.9 所示。其中 $e_1(t)$ 是由死区和延迟引起，幅值为 ± 1 的矩形波脉冲序列， $e_2(t)$ 是由电压上升、下降时间引起，幅值为 ± 1 的锯齿波脉冲序列， $e_3(t)$ 是由电压振荡引起的衰减正弦脉冲序列。考虑这些非理想因素后，最终得到的桥臂输出电压

$$v_{dsRT}(t) = p_{CTE}(t) + p_{CTE}(t) + e_1(t) + e_2(t) + e_3(t) \quad (3-12)$$

对 $e_{1,2,3}(t)$ 求其傅里叶变换，得到

$$E_{1,2,3}(f) = \begin{cases} \sum_{k=-\infty}^{\infty} \frac{1}{-j2\pi f} \left[e^{-j2\pi f(t_{10} + \Delta t_{1k})} - e^{-j2\pi f t_{10}} - e^{-j2\pi f(t_{20} + \Delta t_{2k})} + e^{-j2\pi f t_{20}} \right], f \neq 0 \\ \sum_{k=-\infty}^{\infty} (\Delta t_{1k} - \Delta t_{2k}), f = 0 \end{cases} \quad (3-13)$$

其中 $t_{10} = kT_s$, $t_{20} = kT_s + T_s$, Δt_{1k} 和 Δt_{2k} 的表达式如(3-14)所示， $\sigma(t)$ 是选择函数，即 $\sigma(t) = 1$ ($t > 0$)，否则 $\sigma(t) = 0$ 。

54

第三章 三相脉冲关系的规律研究

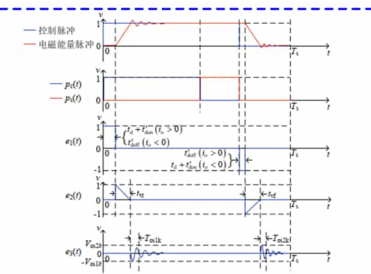


图 3.9 电磁能量脉冲的分解图示

$$\begin{cases} \Delta t_{1k} = t_{on} + \sigma(t_{10})(t_r + t_{fall} - t_{on}) \\ \Delta t_{2k} = t_r + t_{fall} + \sigma(t_{20})(t_{on} - t_r - t_{fall}) \end{cases} \quad (3-14)$$

对 $e_1(t)$ 求其傅里叶变换，得到

$$E_{1,2,3}(f) = \begin{cases} \sum_{k=-\infty}^{\infty} e^{-j2\pi f t_{10}} \left(\frac{1 - j2\pi f t_{1k}}{4\pi^2 f^2 t_{1k}} \right) - e^{-j2\pi f t_{10}} \left(\frac{1 - j2\pi f t_{2k}}{4\pi^2 f^2 t_{2k}} \right), f \neq 0 \\ \sum_{k=-\infty}^{\infty} (t_{2k} - t_{1k}), f = 0 \end{cases} \quad (3-15)$$

其中 t_{1k} 和 t_{2k} 分别为第 k 个开关周期内，桥臂输出电压脉冲的上升沿和下降沿起始时刻。有 $t_{1k} = t_{10} + \Delta t_{1k}$, $t_{2k} = t_{20} + \Delta t_{2k}$, t_{10} 和 t_{20} 分别表示该开关周期内的电压上升和下降时间。

对于 $e_3(t)$ ，首先分析上升沿和下降沿两处振荡的参数表达式。脉冲上升沿的振荡是来自回路杂感 L_{ary} 和 下管结电容 $C_{oss} + C_n$ 的串联谐振，因此有归一化后的 $V_{osc1} = V_{peak1}/V_{DC} - 1$ ，其中 V_{peak1} 为下管关断时电压的尖峰幅值，振荡频率为 $\omega_{osc1} = 1/\sqrt{L_{ary}(C_{oss} + C_n)}$ ，衰减系数 $\alpha_1 = R_p/2L_{ary}$ (这里忽略了桥臂上管的导通电阻)，而脉冲下降沿的振荡发生在 L_{ary} 和上管结电容的串联谐振，此时下管呈导通状态，

55

3.2.2 实际电磁能量脉冲的频谱分析

与理想电磁能量脉冲相比，实际电磁能量脉冲要考虑死区、延迟及开关过渡过程的影响。分别用脉冲 $e_1(t)$, $e_2(t)$ 和 $e_3(t)$ 来表征这些非理想因素的影响，如图 3.9 所示。其中 $e_1(t)$ 是由死区和延迟引起，幅值为 ± 1 的矩形波脉冲序列， $e_2(t)$ 是由电压上升、下降时间引起，幅值为 ± 1 的锯齿波脉冲序列， $e_3(t)$ 是由电压振荡引起的衰减正弦脉冲序列。考虑这些非理想因素后，最终得到的桥臂输出电压

$$v_{dsRT}(t) = p_{CTE}(t) + p_{CTE}(t) + e_1(t) + e_2(t) + e_3(t) \quad (3-12)$$

对 $e_{1,2,3}(t)$ 求其傅里叶变换，得到

当忽略死区时间、延迟和开关瞬态时，即研究理想功率脉冲时，频谱将与控制脉冲的频谱相同。本节首先研究这种情况，以后沿 PWM (TEPWM) 为例[40]，PWM 脉冲可以分解为占空比为 50% 的方波，定义为 p_{CTE} ，加上与调制信号相关的脉冲序列，定义为 $p_{ps, TE}$ 。
时域和频域表达式 p_{CTE} 给出为
哪里 u 是单位阶跃函数，并且 δ 是单位脉冲函数。时域和频域表达式 $p_{ps, TE}$ 给出为：
哪里 k 是 PWM 脉冲的脉冲宽度 k 期数。然后可以计算出理想功率脉冲的频谱

死区时间和延迟、上升/下降时间和有功功率脉冲振荡的影响可以用 $e_1(t)$, $e_2(t)$ 和 $e_3(t)$ ，如图 12 所示。 $e_1(t)$ 是介于 ± 1 之间的矩形脉冲，用于描述死区时间和延迟。 $e_2(t)$ 是介于 ± 1 之间的锯齿脉冲，描述上升/下降时间。 $e_3(t)$ 是描述振荡的阻尼正弦脉冲。
考虑到所有这些非理想因素，输出电压脉冲的最终表达式为

中文直译

只需把图例改成英文

The Fourier transformation of $e_{1,TE}(t)$ provides the equation

$$E_{1,TE}(f) = \begin{cases} \sum_{k=-\infty}^{\infty} \frac{1}{j2\pi f} [e^{-j2\pi f(t_{20} + \Delta t_{2k})} - e^{-j2\pi f t_{20}}] & f \neq 0 \\ \sum_{k=-\infty}^{\infty} (\Delta t_{1k} - \Delta t_{2k}) & f = 0 \end{cases} \quad (17)$$

where $t_{10} = kt_{e0}$ and $t_{20} = kt_{e0} + t_{d0}$. The expressions of Δt_{1k} and Δt_{2k} are given in the following equation. $\sigma(t)$ is a selector, where $\sigma(t) = 1(t_0(t) > 0)$, otherwise $\sigma(t) = 0$

$$\begin{cases} \Delta t_{1k} = t_{doff} + \sigma(t_{10}) (t_{d0} + t_{doff} - t_{doff}) \\ \Delta t_{2k} = t_{d0} + t_{doff} + \sigma(t_{20}) (t_{doff} - t_{d0} - t_{doff}) \end{cases} \quad (18)$$

The Fourier transformation of $e_{2,TE}(t)$ provides the equation

$$E_{2,TE}(f) = \begin{cases} \sum_{k=-\infty}^{\infty} \frac{e^{-j2\pi f t_{1k}} (1 - j2\pi f t_{d0} e^{-j2\pi f t_{d0}})}{4\pi^2 f^2 t_{d0}} & f \neq 0 \\ \sum_{k=-\infty}^{\infty} (t_{1k} - t_{2k}) & f = 0 \end{cases} \quad (19)$$

where t_{1k} and t_{2k} are the start time instant of the rising edge and the falling edge of the output voltage pulse in the k th switching cycle, respectively. $t_{1k} = t_{10} + \Delta t_{1k}$ and $t_{2k} = t_{20} + \Delta t_{2k}$. t_{10} and t_{20} are the rising and falling time of the voltage waveform in the k th switching cycle.

For $e_{1,TE}(t)$, the expressions of the oscillation parameters are derived first. The oscillation during the rising edge results from the series resonance of the power loop stray inductance L_{stray} and the junction capacitance of the lower switch $C_{oss2} + C_{j1}$. The normalized amplitude is given as $V_{osc1} = V_{peak2}/V_{dc} = 1$, where V_{peak2} is the peak voltage of the lower switch during the turn-off transient. The oscillation frequency is given as $\omega_{osc1} = 1/\sqrt{L_{stray}(C_{oss2} + C_{j1})}$, and the damping ratio is given as $\alpha_1 = R_{ds(on)}/2L_{stray}$, where the ON-state resistance of the upper switch is ignored here. As for the falling-edge oscillation which is due to the series resonance of L_{stray} and the junction capacitance of the upper switch, the lower switch is in ON-state and therefore $V_{osc2} \approx 0$. As a result, only the rising-edge oscillation has to be considered. The Fourier transformation of $e_{2,TE}(t)$ is given as

$$E_{2,TE}(f) = \sum_{k=-\infty}^{\infty} \frac{V_{osc1} \omega_{osc1} e^{-j2\pi f t_{1k}}}{(\alpha_1 + j2\pi f)^2 + \omega_{osc1}^2} \quad (20)$$

Then, the general form of the frequency spectrum of the power pulse is given as

$$P_{eq,TE}(f) \equiv P_{1,TE}(f) + P_{2,TE}(f) = E_{1,TE}(f) - E_{2,TE}(f) = E_{3,TE}(f) \quad (21)$$

C. Case Study

To verify the proposed frequency-domain analysis, a sine wave $x(t) = M \sin(2\pi f_0 t)$ is selected as a modulation signal, where $M = 0.9$ and $f_0 = 1$ kHz. The carrier signal is 100-kHz sawtooth signal between ± 1 . The ideal PWM pulse

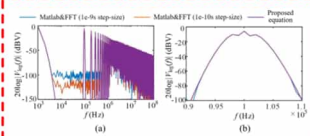


Fig. 13. Comparisons of the frequency spectrum of ideal power pulse between the FFT calculation of MATLAB simulated results and the proposed equation results. (a) Full frequency spectrum. (b) Zoomed-in view near the switching frequency.

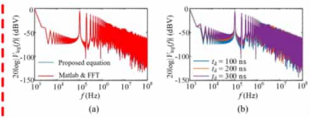


Fig. 14. Frequency spectrum of power pulse with dead-time. (a) Comparisons between the FFT calculation of MATLAB simulated results and the proposed equation results with different dead-time. (b) Spectrums with different dead-time.

is studied first. The frequency spectrum is calculated with both the derived equation (15), and with MATLAB simulations together with fast Fourier transform (FFT) calculations. Because here we first focus on ideal-switch-based spectrum, the MATLAB model uses the ideal switch model without switching transients. The results are compared in Fig. 13. It is shown that the MATLAB simulated results with FFT calculations converge to the equation calculated results when decreasing the FFT step-size, which attests to the accuracy of the derived equation.

Next, the impact of dead-time is taken into account. Assume a dead-time of $t_d = 100$ ns, and a 0.8 power factor of the load. Similarly, the calculated results with the proposed equation are compared with the FFT results of the MATLAB simulation, which are in good agreements, as shown in Fig. 14(a). Still, the MATLAB device model is ideal switch model without switching transients. Meanwhile, different frequency spectrums with different dead-time are shown in Fig. 14(b). With the increase of dead-time, the baseband and sideband harmonics increases correspondingly, while the high-frequency (≥ 1 MHz) harmonics remain largely unchanged.

The impact of delay time on the output frequency spectrum is similar to that of dead-time, and is dependent on the difference between t_{doff} and t_{d0} . Assume $t_{doff} = 90$ ns. The value of t_{d0} is dependent on the load current, as shown in Fig. 15(a). The frequency spectrums with different turn-off delay are shown in Fig. 15(b), which are similar to the results in Fig. 14(b).

Finally, the impact of transient process including rising/falling and oscillation is studied. The device parameters used in the studies are summarized in Table II. Some of these values including the junction capacitances, MOS transconductance, and threshold voltage are extracted from the

中文直译
(整段翻译, 译文太长, 大家自己上网看一下吧)

中文直译
(整段翻译, 译文太长, 大家自己上网看一下吧)

截图大法

$$E_{3,TE}(f) = \begin{cases} \sum_{k=-\infty}^{\infty} \frac{1}{j2\pi f} [e^{-j2\pi f(t_{1k} + t_{d0})} - e^{-j2\pi f t_{1k}} - e^{-j2\pi f(t_{2k} + t_{d0})} + e^{-j2\pi f t_{2k}}] & f \neq 0 \\ \sum_{k=-\infty}^{\infty} (\Delta t_{1k} - \Delta t_{2k}) & f = 0 \end{cases} \quad (3-13)$$

其中 $t_{1k} = ktT_s$, $t_{2k} = ktT_s + \Delta t_{1k}$ 和 Δt_{2k} 的表达式如(3-14)所示, $\sigma(t)$ 是选择函数, 即 $\sigma(t) = 1(t_0(t) > 0)$, 否则 $\sigma(t) = 0$.

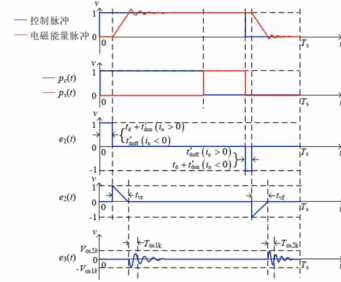


图9 电磁能量脉冲的分解图示

$$\begin{cases} \Delta t_{1k} = t_{doff} + \sigma(t_{10})(t_{d0} + t_{doff} - t_{doff}) \\ \Delta t_{2k} = t_{d0} + \sigma(t_{20})(t_{doff} - t_{d0} - t_{doff}) \end{cases} \quad (3-14)$$

对 $e_d(t)$ 求其傅里叶变换, 得到

$$E_{3,TE}(f) = \sum_{k=-\infty}^{\infty} \frac{e^{-j2\pi f t_{1k}} (1 - j2\pi f t_{d0} - e^{-j2\pi f t_{d0}})}{4\pi^2 f^2 t_{d0}} - e^{-j2\pi f t_{2k}} \frac{(1 - j2\pi f t_{d0} - e^{-j2\pi f t_{d0}})}{4\pi^2 f^2 t_{d0}} & f \neq 0 \\ \sum_{k=-\infty}^{\infty} (t_{1k} - t_{2k}) & f = 0 \end{cases} \quad (3-15)$$

其中 t_{1k} 和 t_{2k} 分别为第 k 个开关周期内, 桥臂输出电压脉冲的上升沿和下降沿起始时刻。有 $t_{1k} = t_{doff} + \Delta t_{1k}$, $t_{2k} = t_{d0} + \Delta t_{2k}$ 。 t_{d0} 和 t_{doff} 分别表示该开关周期内的电压上升和下降时间。

对于 $e_d(t)$, 首先分析上升沿和下降沿两处振荡的参数表达式。脉冲上升沿的振荡是来自回路杂电感 L_{stray} 和下管结电容 $C_{oss2} + C_{j1}$ 的串联谐振, 因此有归一化后的 $V_{osc1} = V_{peak2}/V_{dc} = 1$, 其中 V_{peak2} 为下管关断时电压的尖峰电压, 振荡频率为 $\omega_{osc1} = 1/\sqrt{L_{stray}(C_{oss2} + C_{j1})}$, 衰减系数 $\alpha_1 = R_{ds(on)}/2L_{stray}$ (这里忽略了桥臂上管的导通电阻)。而脉冲下降沿的振荡发生在 L_{stray} 和上管结电容的串联谐振, 此时下管呈导通状态。

因此可认为 $V_{osc2} = 0$ 。因此, 可只分析上升沿处的电压振荡, 求其傅里叶变换得到

$$E_{1,TE}(f) = \sum_{k=-\infty}^{\infty} \frac{V_{osc1} \omega_{osc1} e^{-j2\pi f t_{1k}}}{(\alpha_1 + j2\pi f)^2 + \omega_{osc1}^2} \quad (3-16)$$

因此, 对于一般性调制信号, 实际电磁能量脉冲的频谱为

$$P_{eq,TE}(f) = P_{1,TE}(f) + P_{2,TE}(f) - E_{1,TE}(f) - E_{2,TE}(f) - E_{3,TE}(f) \quad (3-17)$$

3.2.3 周期调制信号分析

以上分析针对的是一般调制信号下电磁能量脉冲频谱的计算方法, 当调制信号为周期信号时, 可只对一个调制周期内的信号进行分析, 设调制信号周期为 T_0 , 载波周期为 T_s 且有 $T_0 = mT_s$, 其中 m 为整数。对于 m 为非整数情况, 可按 $pT_s = qT_0$ 处理, 其中 p, q 为整数。此时, 对于一般性的周期调制信号, 有电磁能量脉冲频谱的计算式为

$$V_{eq,TE}(f) = P_{1,TE}(f) + P_{2,TE}(f) - E_{1,TE}(f) - E_{2,TE}(f) - E_{3,TE}(f) \quad (3-18)$$

其中周期性调制信号频谱可由非周期信号频谱计算得到, 即

$$F_{op}(f) = \frac{2\pi}{pT_0} \sum_{l=-\infty}^{\infty} F(f_l) \delta(f - l f_0) \quad (3-19)$$

其中 $F(f)$ 代表公式(3-10), (3-13), (3-15)及(3-16), 在周期信号调制时, $F(f)$ 中的 k 的取值为 $0 \sim q-1$, 其中当 m 为整数时, 有 $p = 1, q = m$ 。

3.2.4 仿真及实验验证

以正弦波调制信号 $x(t) = M \sin(2\pi f_0 t)$ 为例, 其中 $M = 0.9, f_0 = 1$ kHz。载波信号为幅值为 ± 1 , 频率 $f_s = 100$ kHz 的锯齿波信号。通过 MATLAB 仿真得到归一化后的理想电磁能量脉冲, 经 FFT 计算后得到频谱结果, 与按公式(3-11)得到的频谱结果的对比如图 3.10 所示。从图中可以看出, FFT 计算结果受仿真步长的影响, 步长越小, 与公式计算结果吻合, 这也进一步验证了公式计算的准确性。

考虑死区因素影响, 设死区时间 $t_d = 100$ ns, 负载功率因数为 0.8, 电路工作在 TEC (two even crossover) 模式, 即在一个调制周期内, 负载电流 i_{La} 的方向改变两次。而对于非 TEC 模式, 则需考虑负载电流 i_{La} 的高频谐波分量, 具体分析方法及公式(3-18)计算结果如图 3.11 (a) 所示, 两者计算结果一致。同时, 不同死区时间下公式计算得到的电磁能量脉冲序列的频谱如图 3.11 (b) 所示, 可以看出随着死区时间

的增加, 输出电磁能量脉冲的基带谐波分量和边带谐波分量相应增加, 而对高频 (≥ 1 MHz) 分量的影响可以忽略。

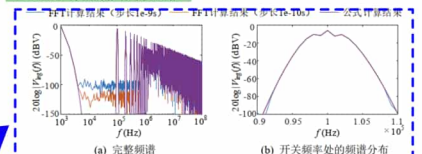


图3.10 理想电磁能量脉冲的频谱

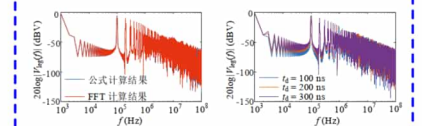


图3.11 考虑死区后电磁能量脉冲的频谱

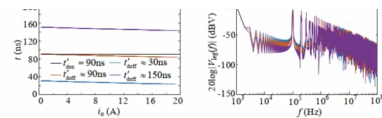


图3.12 考虑延迟后电磁能量脉冲的频谱

延迟对输出电磁能量脉冲频谱的影响和死区相似，其影响因素与 t_{dem} 和 t_{doff} 之差有关。在案例分析中，选择 $t_{\text{dem}} = 90\text{ns}$ ， t_{doff} 与负载电流 i_o 有关。图 3.12 (a) 展示了 t_{doff} 与 i_o 的关系。图 3.12 (b) 比较了不同 t_{doff} 下的电磁能量脉冲频谱。其影响规律同死区时间相似，即主要影响电磁能量脉冲频谱的基带和边带谐波。

57

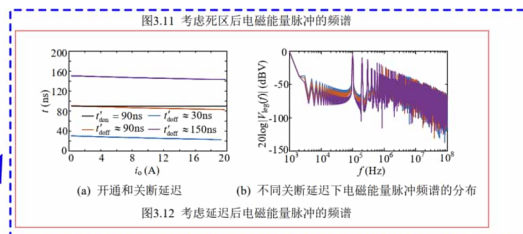


图3.12 考虑延迟后电磁能量脉冲的频谱

延迟对输出电磁能量脉冲频谱的影响和死区相似，其影响因素与 t_{dem} 和 t_{doff} 之差有关。在案例分析中，选择 $t_{\text{dem}} = 90\text{ns}$ ， t_{doff} 与负载电流 i_o 有关。图 3.12 (a) 展示了 t_{doff} 与 i_o 的关系。图 3.12 (b) 比较了不同 t_{doff} 下的电磁能量脉冲频谱。其影响规律同死区时间相似，即主要影响电磁能量脉冲频谱的基带和边带谐波。

57

第 3 章 三组脉冲关系的规律研究

接下来考虑开关过渡过程（主要包括电压上升下降时间和电压振荡部分）对电磁能量脉冲频谱的影响。首先将公式(3-18)计算结果同实验结果进行对比，如图 3.13 所示。其中实验波形为图 2.16 所示的不同驱动电阻下的实验波形，实验波形频谱为根据实验波形进行 FFT 计算及归一化处理后得到的结果。而对于公式计算频谱，则首先根据实验波形提取不同驱动电阻下的电压上升时间 t_r 、电压下降时间 t_f 及电压振荡参数 V_{on1} 、 ω_{on1} 及 α_1 ，然后代入公式(3-18)得到频谱计算结果。

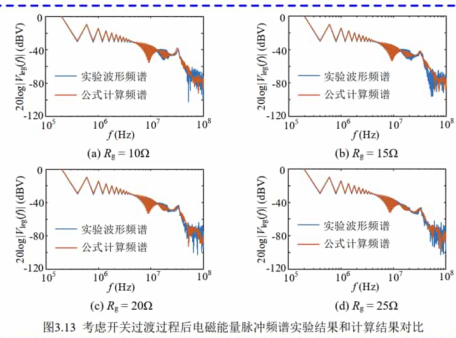


图3.13 考虑开关过渡过程后电磁能量脉冲频谱实验结果和计算结果对比

从图 3.13 可以看出，公式计算频谱与实验波形频谱较为吻合。其中在高频处的频谱有一定偏差，主要是由于实验波形电压上升、下降过程的非线性及测量噪声所致。

回到所研究的案例，图 3.14 (a) 展示了不同电压上升、下降时间时的电磁能量脉冲频谱，图 3.14 (b) 展示了不同电压振荡幅值下的电磁能量脉冲频谱。其中 $t_r = 38\text{ns}$ 及 $t_f = 24\text{ns}$ 是 SIC MOSFET CMF20120D 数据手册[84]中给出的电压上升、下降时间的典型值。从图中可以看到，电压上升、下降时间主要影响电磁能量脉冲高频处的频谱衰减速度，电压上升、下降时间越大，电磁能量脉冲的高频衰减越快。而电压振荡主要影响振荡频率附近的频谱幅值，与电压振荡幅值呈正相关。

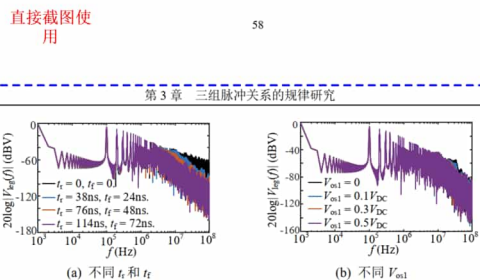


图3.14 考虑开关过渡过程后电磁能量脉冲的频谱

第 3 章 三组脉冲关系的规律研究

对于 DEPWM，有

SHI et al.: TIME-DOMAIN AND FREQUENCY-DOMAIN ANALYSIS OF SIC MOSFET SWITCHING TRANSIENTS

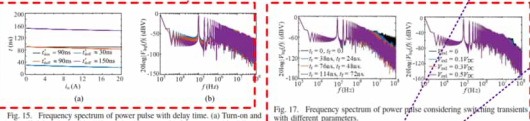


Fig. 15. Frequency spectrum of power pulse with delay time. (a) Turn-on and turn-off delay time with different load current. (b) Spectrums with different turn-off delay.

TABLE II
DEVICE AND CIRCUIT PARAMETERS IN THE FREQUENCY-DOMAIN STUDIES CONSIDERING SWITCHING TRANSIENTS

Component	Parameter	Value	Parameter	Value
Main Circuit	L_{main}	180 nH	R_e	12 mΩ
	L_{out}	1 mH	R_o	5 Ω
	V_{dc}	20 V	V_{in}	-5 V
	R_f	10 ~ 25 Ω	R_{on}	0.1 Ω
Gate Driver	R_g	13 pF	C_{in}	1143 pF
	C_{gd}	107 pF	C_{out}	1463 pF
	C_{gs}	1902 pF	R_{on1}	0.08 Ω
	R_{gs}	0.77 nV	V_{a}	4.44 V
SIC MOSFET (CMF 20120D)	T_c	25 °C	V_{ce}	25 V
	C_{e}	100 pF	C_{d}	2400 pF

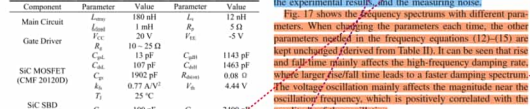


Fig. 17. Frequency spectrum of power pulse considering switching transient with different parameters.

The proposed method provides an analytical way to calculate and analyze the frequency spectrum of the power pulse considering dead-time, delay time, and switching transient and to study how different factors affect the spectrum. If the frequency range is divided into signal band ($f_{\text{sig}} \leq f < f_c$), carrier band ($f_c \leq f < 10f_c$), and EMI band ($f > 10f_c$), it can be observed that dead-time and delay time mainly affect the signal and carrier band, while the switching transient mainly affects the EMI band. According to the interested frequency range, certain nonideal factors should be selected to highlight the key mechanisms while avoiding excessively complex modeling.

IV. DISCUSSION ON AGC OF THE POWER PULSE
Sections II and III provide quantitative analyses on the relationship (delay and distortion) between the control, drive, and power pulse, from the perspectives of both time-domain and the frequency-domain, together with the impact of system parameters (gate drive parameters, dead-time, etc.) on these delays and distortion. The analyses can be used to guide the design and evaluation of AGC methods. In this section, the relationship between pulse delay and distortion with the system performance is summarized, based on which a brief discussion on the general strategy for AGC is provided.
Impact of the delay and distortion on system performance is summarized in Table III.
The relationships in Table III and the quantitative analyses above can guide and optimize the practical device-level design. For different design goals, different factors should be highlighted. For example, to decrease the output distortion (THD), dead-time and delay time should be focused, and their quantitative impacts on low-frequency EMI (signal and carrier band) can be evaluated with the frequency-domain methods presented in Section III, and based on which, the dead-time

直接截图使用

中文直译

直接截图使用

中文直译

直接截图使用

58

中文直译

$$P_{c,DE}(f) = \sum_{k=-\infty}^{\infty} \frac{2(-1)^{k+1}}{2k+1} \delta[f - (2k+1)f_c] + \pi\delta(f) \quad (3-23)$$

$$P_{s,DE}(f) = \begin{cases} \sum_{k=-\infty}^{\infty} \frac{e^{-j2\pi f(kT_c + \tau_{1k})} - e^{-j2\pi f(kT_c + \tau_{2k})}}{-j2\pi f} \left[2j \sin\left(\frac{\pi f T_c}{2}\right) - e^{j2\pi f \tau_{1k}} + e^{-j2\pi f \tau_{2k}} \right], & f \neq 0 \\ \sum_{k=-\infty}^{\infty} \left(\tau_{1k} + \tau_{2k} - \frac{T_c}{2} \right), & f = 0 \end{cases} \quad (3-24)$$

$E_{1,DE}(f)$, $E_{2,DE}(f)$ 及 $E_{3,DE}(f)$ 的计算公式与 TEPWM 的计算公式一致, 只需将参数 t_{10} 及 t_{20} 修正为 $t_{10} = (k+1/2)T_c - \tau_{1k}$, $t_{20} = (k+1/2)T_c + \tau_{2k}$.

中文直译

3.2.6 频域影响规律总结及应用

在小节 3.2.4 中, 结合案例通过仿真和实验波形对电磁能量脉冲的频谱计算方法进行了验证, 同时分析了不同因素对电磁能量脉冲频谱的影响规律。若将电磁能量脉冲的频谱按频段划分为信号频段 ($f_0 \leq f < f_c$)、载波频段 ($f_c \leq f < 10f_c$) 及 EMI 频段 ($f > 10f_c$), 则死区和延迟主要影响的是信号频段和载波频段, 而开关过渡过程则主要影响 EMI 频段。

所提电磁能量脉冲的频域表征方法提供了一种考虑脉冲延迟和畸变关系的、对电磁能量脉冲频谱进行表征的定量分析方法。通过分析死区、延迟及开关过渡过程对电磁能量脉冲频谱的影响规律, 可以根据研究问题所处频段, 选择相关的非理想因素进行考虑, 进而避免过于简单或复杂的分析建模。比如若研究 THD, 则主要与信号频段及载波频段内的频谱有关, 因此, 可只考虑死区和延迟, 而无需考虑开关过渡过程。而若要研究系统的 EMI 特性, 则需考虑电磁能量脉冲的开关过渡过程。

3.3 三组脉冲关系表征的应用研究

在 3.1 和 3.2 节中分别从时域和频域, 对三组脉冲的关系进行表征, 进而更全面地对三组脉冲之间的传递规律及其对系统性能的影响进行定量分析。表 3.2 列举了主要脉冲关系及其对系统性能的影响, 并总结了相应的定量分析方法。

表 3.2 三组脉冲关系及与系统性能关系的定量分析

三组脉冲关系	形态属性分析		与系统性能关系	
	参数表征	定量分析方法	描述	定量分析方法
死区	t_d	控制算法给定	输出波形质量 (THD)	频谱分析方法
开通、关断延迟	t_{on}, t_{off}	开关瞬态分析模型	输出波形质量 (THD)	频谱分析方法
电压上升、下降时间	$t_{v(20\%)}, t_{v(80\%)}$	开关瞬态分析模型	输出波形的高频频谱 (EMI)	频谱分析方法
电流上升、下降时间	$t_{i(20\%)}, t_{i(80\%)}$	开关瞬态分析模型	电压与电流尖峰	开关瞬态分析模型
电压、电流尖峰	V_{peak}, I_{peak}	开关瞬态分析模型	开关损耗	开关损耗分析模型
电压、电流振荡	$V_{osc}, Q_{osc}, \theta_{osc}, I_{osc}, Q_{osc}, \theta_{osc}$	开关瞬态分析模型	装置电压、电流等级	开关瞬态分析模型
			输出波形的高频频谱 (EMI)	频谱分析方法

在表 3.2 所列脉冲关系中, 死区和延迟主要影响输出波形质量, 可通过控制算法进行补偿, 而电压、电流的上升、下降时间及电压、电流尖峰主要带来开关损耗、器件应力及 EMI 等问题, 要通过对电磁能量脉冲的畸变关系进行控制以改善这些系统性能, 是一个多参数耦合的多目标优化问题。对于这类问题, 现代优化算法是有效的解决方法, 但不能揭示出系统参数对这些系统性能的影响规律, 所得到的优化结果也不具有普适性。因此, 本节将抓住电磁能量脉冲的主要瞬态行为, 分析比较系统可控参数对主要瞬态行为及系统性能的影响规律, 进而总结提炼出对电磁能量脉冲瞬态行为进行控制的一般规律。

3.3.1 驱动回路参数对脉冲规律的影响

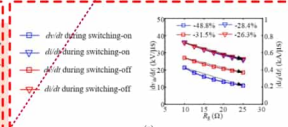
从表 3.2 中对电磁能量脉冲畸变关系的表征可以看出, 电磁能量脉冲的畸变关系均受开通和关断过程中 dv/dt 和 di/dt 的影响, 其中电压、电流上升和下降时间与 dv/dt 和 di/dt 直接相关, 电压、电流尖峰与 di/dt 正相关, 电压、电流振荡的幅值, 与电压、电流尖峰一致, 也与 di/dt 正相关, 因此, 可以说器件开关过程中的 dv/dt 和 di/dt 是影响电磁能量脉冲畸变关系的主要参数。

表格选取一部分, 然后翻译

中文直译

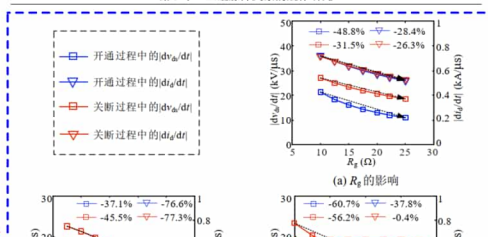
TABLE III
IMPACT OF THE DELAY AND DISTORTION ON SYSTEM PERFORMANCE

Pulse delay and distortion	Characteristic parameters	Impact on system performance
Dead-time	t_d	Output distortion (THD)
Turn-on/off delay	t_{on}, t_{off}	Output distortion (THD)
Rising/falling process	$t_{r}, t_{f}, t_{v}, t_{i}$	High-frequency EMI
Voltage/current spike	V_{peak}, I_{peak}	Switching loss
		Capacity



截图大法

表 3.3 驱动回路参数对脉冲规律的影响



High-frequency EMI
Spurious operation
loop stability

and delay time can be compensated with control algorithms [12], [13] to improve the THD performance.

Another discussion to apply the above analyses in practical design is to optimize the switching-loss system efficiency, switching spikes, and high-frequency EMI. These goals are usually conflicted: faster transient leads to lower switching loss, but potentially higher spikes and more serious EMI. The analyses above provide methodologies to quantitatively optimize these goals by changing the gate resistance (Figs. 8(b) and 16) or adding extra capacitances (Fig. 8(a)-(d)) to meet the required goals. Alternatively, AGC methods provide a promising solution to actively control the microsecond- and nanosecond-level switching transients in power electronics. The core idea of AGC methods is to adaptively control the di/dr and dv/dr during different stages in switching transient, so that the system performance can be improved. As a result, a significant issue is the controllability of the power pulse by adjusting gate drive parameters.

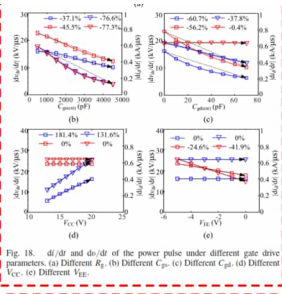


Fig. 18. dv/dr and di/dr of the power pulse under different gate drive parameters. (a) Different R_g . (b) Different C_{gd} . (c) Different V_{CC} . (d) Different V_{GE} . (e) Different V_{CE} .

Fig. 18 demonstrates how well different gate parameters (R_g , C_{gd} , V_{CC} , and V_{GE}) affect the dv/dr and di/dr of the power pulse. The results come from calculations with the analytical model proposed in [20]. The number on top of each subfigure shows the increased percentage when the parameter is changed from the minimum value to the maximum value (according to the direction of the black arrow). It can be observed that by changing R_g , V_{CC} , and V_{GE} , the trends of the di/dr and dv/dr are more consistent, and can be a good choice to control the slew rate. Once di/dr and dv/dr are controlled, system performance including voltage and current spikes in (3), the amplitude of oscillation in Table I, and switching loss in Table II can be controlled correspondingly. Experiments are performed to study the impact of different gate drive parameters on transient spike and switching loss, and the results are shown in Fig. 19. A clear tradeoff can be observed between the transient spike and the switching loss.

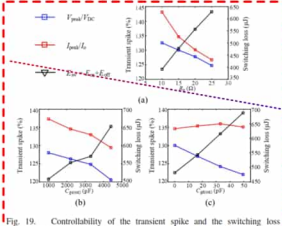


Fig. 19. Controllability of the transient spike and the switching loss by adjusting gate drive parameters. (a) Different R_g . (b) Different C_{gd} . (c) Different V_{CC} .

presented here. According to the time-domain analyses above, in hard-switching condition, the switching transient of gate insulated devices such as IGBT and MOSFET can be divided into delay stage, di/dr stage, dv/dr stage, and oscillation (for MOSFET) or tail (for IGBT) stage. The switching loss is negatively correlated with voltage/current slew rate, while the transient spike is positively correlated with it. As a result,

presented here. According to the time-domain analyses above, in hard-switching condition, the switching transient of gate insulated devices such as IGBT and MOSFET can be divided into delay stage, di/dr stage, dv/dr stage, and oscillation (for MOSFET) or tail (for IGBT) stage. The switching loss is negatively correlated with voltage/current slew rate, while the transient spike is positively correlated with it. As a result,

presented here. According to the time-domain analyses above, in hard-switching condition, the switching transient of gate insulated devices such as IGBT and MOSFET can be divided into delay stage, di/dr stage, dv/dr stage, and oscillation (for MOSFET) or tail (for IGBT) stage. The switching loss is negatively correlated with voltage/current slew rate, while the transient spike is positively correlated with it. As a result,

presented here. According to the time-domain analyses above, in hard-switching condition, the switching transient of gate insulated devices such as IGBT and MOSFET can be divided into delay stage, di/dr stage, dv/dr stage, and oscillation (for MOSFET) or tail (for IGBT) stage. The switching loss is negatively correlated with voltage/current slew rate, while the transient spike is positively correlated with it. As a result,

presented here. According to the time-domain analyses above, in hard-switching condition, the switching transient of gate insulated devices such as IGBT and MOSFET can be divided into delay stage, di/dr stage, dv/dr stage, and oscillation (for MOSFET) or tail (for IGBT) stage. The switching loss is negatively correlated with voltage/current slew rate, while the transient spike is positively correlated with it. As a result,

presented here. According to the time-domain analyses above, in hard-switching condition, the switching transient of gate insulated devices such as IGBT and MOSFET can be divided into delay stage, di/dr stage, dv/dr stage, and oscillation (for MOSFET) or tail (for IGBT) stage. The switching loss is negatively correlated with voltage/current slew rate, while the transient spike is positively correlated with it. As a result,

presented here. According to the time-domain analyses above, in hard-switching condition, the switching transient of gate insulated devices such as IGBT and MOSFET can be divided into delay stage, di/dr stage, dv/dr stage, and oscillation (for MOSFET) or tail (for IGBT) stage. The switching loss is negatively correlated with voltage/current slew rate, while the transient spike is positively correlated with it. As a result,

presented here. According to the time-domain analyses above, in hard-switching condition, the switching transient of gate insulated devices such as IGBT and MOSFET can be divided into delay stage, di/dr stage, dv/dr stage, and oscillation (for MOSFET) or tail (for IGBT) stage. The switching loss is negatively correlated with voltage/current slew rate, while the transient spike is positively correlated with it. As a result,

presented here. According to the time-domain analyses above, in hard-switching condition, the switching transient of gate insulated devices such as IGBT and MOSFET can be divided into delay stage, di/dr stage, dv/dr stage, and oscillation (for MOSFET) or tail (for IGBT) stage. The switching loss is negatively correlated with voltage/current slew rate, while the transient spike is positively correlated with it. As a result,

presented here. According to the time-domain analyses above, in hard-switching condition, the switching transient of gate insulated devices such as IGBT and MOSFET can be divided into delay stage, di/dr stage, dv/dr stage, and oscillation (for MOSFET) or tail (for IGBT) stage. The switching loss is negatively correlated with voltage/current slew rate, while the transient spike is positively correlated with it. As a result,

presented here. According to the time-domain analyses above, in hard-switching condition, the switching transient of gate insulated devices such as IGBT and MOSFET can be divided into delay stage, di/dr stage, dv/dr stage, and oscillation (for MOSFET) or tail (for IGBT) stage. The switching loss is negatively correlated with voltage/current slew rate, while the transient spike is positively correlated with it. As a result,

presented here. According to the time-domain analyses above, in hard-switching condition, the switching transient of gate insulated devices such as IGBT and MOSFET can be divided into delay stage, di/dr stage, dv/dr stage, and oscillation (for MOSFET) or tail (for IGBT) stage. The switching loss is negatively correlated with voltage/current slew rate, while the transient spike is positively correlated with it. As a result,

presented here. According to the time-domain analyses above, in hard-switching condition, the switching transient of gate insulated devices such as IGBT and MOSFET can be divided into delay stage, di/dr stage, dv/dr stage, and oscillation (for MOSFET) or tail (for IGBT) stage. The switching loss is negatively correlated with voltage/current slew rate, while the transient spike is positively correlated with it. As a result,

presented here. According to the time-domain analyses above, in hard-switching condition, the switching transient of gate insulated devices such as IGBT and MOSFET can be divided into delay stage, di/dr stage, dv/dr stage, and oscillation (for MOSFET) or tail (for IGBT) stage. The switching loss is negatively correlated with voltage/current slew rate, while the transient spike is positively correlated with it. As a result,

presented here. According to the time-domain analyses above, in hard-switching condition, the switching transient of gate insulated devices such as IGBT and MOSFET can be divided into delay stage, di/dr stage, dv/dr stage, and oscillation (for MOSFET) or tail (for IGBT) stage. The switching loss is negatively correlated with voltage/current slew rate, while the transient spike is positively correlated with it. As a result,

presented here. According to the time-domain analyses above, in hard-switching condition, the switching transient of gate insulated devices such as IGBT and MOSFET can be divided into delay stage, di/dr stage, dv/dr stage, and oscillation (for MOSFET) or tail (for IGBT) stage. The switching loss is negatively correlated with voltage/current slew rate, while the transient spike is positively correlated with it. As a result,

presented here. According to the time-domain analyses above, in hard-switching condition, the switching transient of gate insulated devices such as IGBT and MOSFET can be divided into delay stage, di/dr stage, dv/dr stage, and oscillation (for MOSFET) or tail (for IGBT) stage. The switching loss is negatively correlated with voltage/current slew rate, while the transient spike is positively correlated with it. As a result,

presented here. According to the time-domain analyses above, in hard-switching condition, the switching transient of gate insulated devices such as IGBT and MOSFET can be divided into delay stage, di/dr stage, dv/dr stage, and oscillation (for MOSFET) or tail (for IGBT) stage. The switching loss is negatively correlated with voltage/current slew rate, while the transient spike is positively correlated with it. As a result,

presented here. According to the time-domain analyses above, in hard-switching condition, the switching transient of gate insulated devices such as IGBT and MOSFET can be divided into delay stage, di/dr stage, dv/dr stage, and oscillation (for MOSFET) or tail (for IGBT) stage. The switching loss is negatively correlated with voltage/current slew rate, while the transient spike is positively correlated with it. As a result,

presented here. According to the time-domain analyses above, in hard-switching condition, the switching transient of gate insulated devices such as IGBT and MOSFET can be divided into delay stage, di/dr stage, dv/dr stage, and oscillation (for MOSFET) or tail (for IGBT) stage. The switching loss is negatively correlated with voltage/current slew rate, while the transient spike is positively correlated with it. As a result,

presented here. According to the time-domain analyses above, in hard-switching condition, the switching transient of gate insulated devices such as IGBT and MOSFET can be divided into delay stage, di/dr stage, dv/dr stage, and oscillation (for MOSFET) or tail (for IGBT) stage. The switching loss is negatively correlated with voltage/current slew rate, while the transient spike is positively correlated with it. As a result,

presented here. According to the time-domain analyses above, in hard-switching condition, the switching transient of gate insulated devices such as IGBT and MOSFET can be divided into delay stage, di/dr stage, dv/dr stage, and oscillation (for MOSFET) or tail (for IGBT) stage. The switching loss is negatively correlated with voltage/current slew rate, while the transient spike is positively correlated with it. As a result,

presented here. According to the time-domain analyses above, in hard-switching condition, the switching transient of gate insulated devices such as IGBT and MOSFET can be divided into delay stage, di/dr stage, dv/dr stage, and oscillation (for MOSFET) or tail (for IGBT) stage. The switching loss is negatively correlated with voltage/current slew rate, while the transient spike is positively correlated with it. As a result,

presented here. According to the time-domain analyses above, in hard-switching condition, the switching transient of gate insulated devices such as IGBT and MOSFET can be divided into delay stage, di/dr stage, dv/dr stage, and oscillation (for MOSFET) or tail (for IGBT) stage. The switching loss is negatively correlated with voltage/current slew rate, while the transient spike is positively correlated with it. As a result,

presented here. According to the time-domain analyses above, in hard-switching condition, the switching transient of gate insulated devices such as IGBT and MOSFET can be divided into delay stage, di/dr stage, dv/dr stage, and oscillation (for MOSFET) or tail (for IGBT) stage. The switching loss is negatively correlated with voltage/current slew rate, while the transient spike is positively correlated with it. As a result,

presented here. According to the time-domain analyses above, in hard-switching condition, the switching transient of gate insulated devices such as IGBT and MOSFET can be divided into delay stage, di/dr stage, dv/dr stage, and oscillation (for MOSFET) or tail (for IGBT) stage. The switching loss is negatively correlated with voltage/current slew rate, while the transient spike is positively correlated with it. As a result,

presented here. According to the time-domain analyses above, in hard-switching condition, the switching transient of gate insulated devices such as IGBT and MOSFET can be divided into delay stage, di/dr stage, dv/dr stage, and oscillation (for MOSFET) or tail (for IGBT) stage. The switching loss is negatively correlated with voltage/current slew rate, while the transient spike is positively correlated with it. As a result,

presented here. According to the time-domain analyses above, in hard-switching condition, the switching transient of gate insulated devices such as IGBT and MOSFET can be divided into delay stage, di/dr stage, dv/dr stage, and oscillation (for MOSFET) or tail (for IGBT) stage. The switching loss is negatively correlated with voltage/current slew rate, while the transient spike is positively correlated with it. As a result,

presented here. According to the time-domain analyses above, in hard-switching condition, the switching transient of gate insulated devices such as IGBT and MOSFET can be divided into delay stage, di/dr stage, dv/dr stage, and oscillation (for MOSFET) or tail (for IGBT) stage. The switching loss is negatively correlated with voltage/current slew rate, while the transient spike is positively correlated with it. As a result,

presented here. According to the time-domain analyses above, in hard-switching condition, the switching transient of gate insulated devices such as IGBT and MOSFET can be divided into delay stage, di/dr stage, dv/dr stage, and oscillation (for MOSFET) or tail (for IGBT) stage. The switching loss is negatively correlated with voltage/current slew rate, while the transient spike is positively correlated with it. As a result,

presented here. According to the time-domain analyses above, in hard-switching condition, the switching transient of gate insulated devices such as IGBT and MOSFET can be divided into delay stage, di/dr stage, dv/dr stage, and oscillation (for MOSFET) or tail (for IGBT) stage. The switching loss is negatively correlated with voltage/current slew rate, while the transient spike is positively correlated with it. As a result,

presented here. According to the time-domain analyses above, in hard-switching condition, the switching transient of gate insulated devices such as IGBT and MOSFET can be divided into delay stage, di/dr stage, dv/dr stage, and oscillation (for MOSFET) or tail (for IGBT) stage. The switching loss is negatively correlated with voltage/current slew rate, while the transient spike is positively correlated with it. As a result,

presented here. According to the time-domain analyses above, in hard-switching condition, the switching transient of gate insulated devices such as IGBT and MOSFET can be divided into delay stage, di/dr stage, dv/dr stage, and oscillation (for MOSFET) or tail (for IGBT) stage. The switching loss is negatively correlated with voltage/current slew rate, while the transient spike is positively correlated with it. As a result,

presented here. According to the time-domain analyses above, in hard-switching condition, the switching transient of gate insulated devices such as IGBT and MOSFET can be divided into delay stage, di/dr stage, dv/dr stage, and oscillation (for MOSFET) or tail (for IGBT) stage. The switching loss is negatively correlated with voltage/current slew rate, while the transient spike is positively correlated with it. As a result,

presented here. According to the time-domain analyses above, in hard-switching condition, the switching transient of gate insulated devices such as IGBT and MOSFET can be divided into delay stage, di/dr stage, dv/dr stage, and oscillation (for MOSFET) or tail (for IGBT) stage. The switching loss is negatively correlated with voltage/current slew rate, while the transient spike is positively correlated with it. As a result,

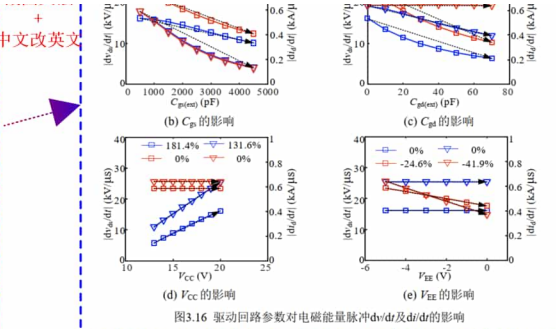


图3.16 驱动回路参数对电磁能量脉冲 dv/dr 及 di/dr 的影响

利用第2章所提分析模型,可定量分析系统参数对 dv/dr 及 di/dr 的影响关系。这里 dv/dr 指电压 v_b 的变化率 dv_b/dr , di/dr 指电流 i_a 的变化率 di_a/dr 。图3.16比较了不同驱动回路参数(R_g , C_{gd} , V_{CC} , V_{GE})对电磁能量脉冲的影响规律。图中以虚线标注了 dv/dr 及 di/dr 随驱动回路参数变化的规律,并以百分比的方式标识了 dv/dr 及 di/dr 的变化率。可以看出,通过改变 R_g 及驱动电平(V_{CC} 和 V_{GE}), dv/dr 及 di/dr 的变化率的一致性较好,而通过改变 C_{gd} , dv/dr 的变化率仅为 di/dr 变化率的一半。对于 C_{gd} , dv/dr 与 di/dr 的变化率之间的差异更为明显。因此,从可控性角度,

图3.17 驱动回路参数对器件应力及开关损耗的影响

驱动电阻及驱动电平对于 dv/dr 和 di/dr 的影响规律具有较好的一致性。另外,通过改变驱动回路参数,影响开关过程中的 dv/dr 和 di/dr ,会进一步影响系统器件应力和开关损耗。图3.17展示了实验测得的不同驱动回路参数下的器件应力和开关损耗,可以看到改变不同的驱动参数,器件应力和开关损耗之间均存在相互制约关系。

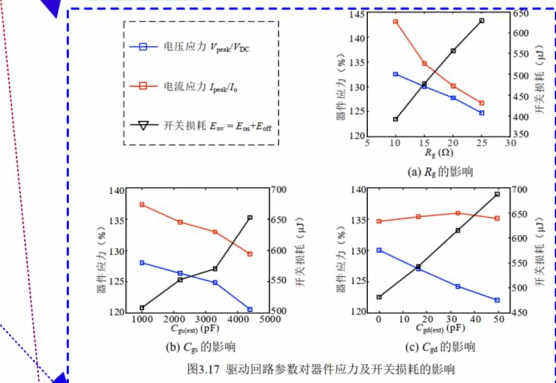


图3.17 驱动回路参数对器件应力及开关损耗的影响

通过分析驱动回路参数对开关过程 dv/dr 及 di/dr 的影响规律,反映出通过改变驱动参数对电磁能量脉冲的瞬态行为进行控制的有效性。然而,若在整个开关过程中保持驱动参数不变,即实现一种基于开关周期调节驱动参数的驱动回路控制方法,则仍然会面临器件应力与开关损耗的相互制约问题。而若根据开关过程的不同阶段来调节驱动回路参数,即主动驱动控制(Active gate control, AGC)方法,则有望实现降低器件应力和降低开关损耗的兼顾。

3.3.2 主动驱动控制的控制策略及其评估

主动驱动控制是一种在硬开关条件下,针对开关过程中的不同阶段,改变驱动回路参数,以对电磁能量脉冲轨迹进行控制,进而兼顾降低器件应力与降低开

图3.18 硬开关条件下MOSFET/IGBT的开关过程阶段划分

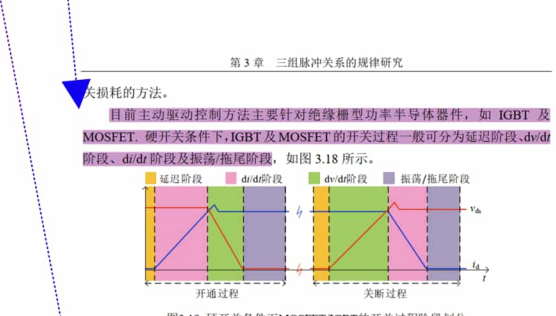


图3.18 硬开关条件下MOSFET/IGBT的开关过程阶段划分

通过表3.2可知,开关损耗主要与 dv/dr 及 di/dr 呈负相关,而器件应力(电压、电流尖峰)主要与 di/dr 呈正相关。因此为了兼顾开关损耗与器件应力,主动驱动控制的一般性策略为对开关过程中的 di/dr 阶段进行检测(一般通过共源极电感 L_s 两端电压的反馈进行检测),在开关过程进入 di/dr 阶段时,通过改变驱动回路参数,以抑制栅极电容充电过程,而在其他阶段,调节驱动回路参数以加快栅极电容充电过程。

中文直译

中文直译

中文改英文

中文直译

截图大法

中文改英文

中文直译

中文直译

中文直译

中文直译

中文直译

中文直译

中文直译

中文直译

公司的 CRD-001) 之间的成本与尺寸比较, 如表 4.3 所示, 本论文提出的主动栅极驱动的成本仅为该常规驱动产品的 67.8%。

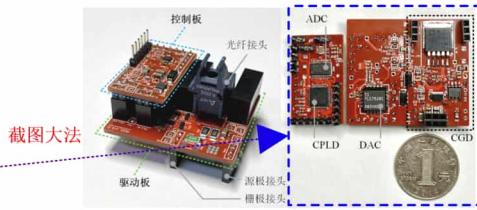


图 4.10 本论文提出的主动栅极驱动的实物图

表 4.3 本论文提出的主动栅极驱动与一款商业化的常规驱动产品 (Cree® 公司的 CRD-001) 的成本与尺寸比较

比较对象	成本	体积 (长 × 宽 × 高)
商业化的常规驱动产品	\$50.0 (100%)	37.6 × 33.5 × 19.6mm ³ (100%)
本论文提出的主动栅极驱动	\$33.9 (67.8%)	45.7 × 39.1 × 22.9mm ³ (166%)

4.4 实验验证与对比

为了验证本论文提出的主动驱动控制方法在开关特性优化与自适应多脉冲优化方面的有效性, 对提出的方法进行双脉冲测试 (double-pulse test, DPT) 与多脉冲测试 (multi-pulse test, MPT)。双脉冲实验平台的主要元件包括: 直流母线电容、两电臂 SiC MOSFET 与 SBD 桥臂和用作感性负载的功率电感。在多脉冲实验中, 采用功率电阻与功率电感作为阻感负载。实验中的被测器件为 Cree® 公司的 SiC MOSFET C2M0080120D (1200V/36A) 和 SiC SBD C4D10120D (1200V/38A)。在下面的对比研究中, 除特别说明外, 常规驱动控制所采用的栅极外电阻 (即图 4.6 中的 $R_{g(ext)}$) 为 10Ω, 主动驱动控制所采用的为 5Ω, SiC MOSFET 的栅极内电阻 (即图 4.6 中的 $R_{g(int)}$) 为 5Ω。

截图大法

88

第4章 SiC MOSFET 开关过程主动驱动控制方法研究

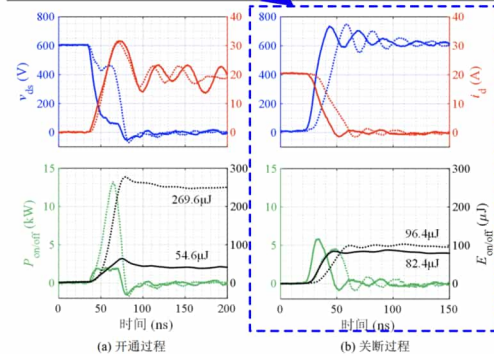


图 4.11 本论文提出的主动驱动控制 (实线波形) 与常规驱动控制 (虚线波形) 下器件的开关过程波形比较

也包含无源辅助电路的损耗 $E_{loss(PAC)}$, 如第 4.2.1 小节中的式 (4-9) 所述, $E_{loss(PAC)}$ 即为含有剩余电流 I_{tail} 的辅助电感 L_a 中储存的能量, I_{tail} 定义为在关断过程中当 v_{Ca} 下降至 0 时 L_a 中的电流。图 4.13 展示了不同负载电流下提出的辅助电路在开关过程中的瞬态波形, 如图 4.13 所示, 负载电流为 15A、20A 和 25A 时的剩余电流分别为 0.5A、2.1A 和 6.9A, 相应的辅助电路损耗分别为 0.03μJ、0.49μJ 和 5.24μJ, 可以看到, 辅助电路的损耗与器件的开关损耗相比可以忽略不计。

2. 提出的主动栅极驱动在抑制瞬态尖峰方面的效果

如第 4.3 节所述, 本论文提出的主动栅极驱动通过在开通过程中从栅极中抽取多余的驱动电流抑制开通电流尖峰, 通过在关断过程中向栅极中注入额外的驱动电流抑制关断电压尖峰。如图 4.14 所示, $VCCS_{on}$ 和 $VCCS_{off}$ 在开关过程中被使能, 通过降低开关过程中的 di_d/dr 来抑制瞬态尖峰。在直流母线电压为 600V、负载电流为 25A 的情况下, 通过采用主动栅极驱动, 开通电流尖峰可由 37.8A 被降低至 35.6A, 关断电压尖峰可由 826V 被降低至 759V。

3. 与常规驱动控制方法的比较

图 4.15 展示的曲线为采用不同 $R_{g(ext)}$ 时常规驱动控制下的器件开关特性与主动驱动控制下的器件开关特性对比图, 测试条件为直流母线电压 600V、负载电流

90



Fig. 20. Experimental prototype of the AGD.

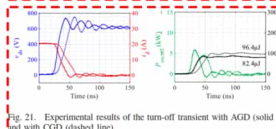


Fig. 21. Experimental results of the turn-off transient with AGD (solid line) and with CGD (dashed line).

an effective technique for AGC is to accelerate the switching transient to minimize the switching loss in all stages, except the di/dr stage where the current slew rate should be restricted to avoid overshoot. For practical design, (3)–(5) provide quantitative supports to determine the gate drive parameters and AGC strategies.

As a verification of the proposed idea, AGC experiments are performed to drive a switch pair composed of SiC MOSFET C2M0080120D (1200 V, 36 A) and SiC SBD C4D10120D (1200 V, 38 A). The active gate driver (AGD) is implemented by adding a controlled current source (current mirror) in parallel with the conventional gate driver (CGD), controller by a complex programmable logic device (CPLD), as shown in Fig. 20. The comprehensive design of the AGD is beyond the scope of this article; instead, experimental results are provided in Fig. 21 to verify the analyses in this article. As shown in the results, during the turn-off transient, by accelerating the voltage rising before v_{ds} reaches dc-bus voltage (600 V) and slowing down the transient after it reaches 600 V the AGD manages to decrease both the switching loss (from 96.4 to 82.4 μJ) and the voltage spike (from 750 to 730 V) simultaneously, which breaks the conventional tradeoff in between with only CGD. The comprehensive design of the AGC strategy and the AGD implementation will be discussed in future work. The analyses and models in this article provide a quantitative methodology for the future studies on AGC.

V. CONCLUSION

This article studies the transmission of control, drive, and power pulses. Time-domain studies are provided first to derive the characteristic parameters of the delay and distortion. Theoretical, numerical, and experimental results are demonstrated to analyze the three pulses, with special emphasis on the gate-loop oscillation to guide gate drive design, ensure gate-loop stability and avoid the spurious operation of the switch. Based on the expressions from time-domain studies, a pulse decomposition method is proposed to study the frequency spectrum

of the power pulse considering all major transient factors, including dead-time, delay time, rise/fall time, voltage/current spikes, and oscillations. Experimental results are provided to verify the proposed method and the results, and the frequency-domain characteristics of the power pulse are analyzed and discussed. Finally, the impact of the delay and distortion on system performance is summarized, the controllability of the power pulse by adjusting gate-drive parameters is investigated, and the general idea of active gate drive is briefly discussed. This article provides a novel point of view to understand the high-speed switching transient from the transmission of pulses, and the demonstrated analyses and results are helpful in the study and design of AGC methods of gate insulated semiconductor devices.

ACKNOWLEDGMENT

The authors would like to thank Fuji Electric Company, Ltd., Tokyo, Japan, for all the support to this article.

REFERENCES

- W. R. Erickson, *Fundamentals of Power Electronics*. Secaucus, NJ, USA: Kluwer, 2000.
- Z. Zhao, D. Tan, and K. Li, "Transient behaviors of multilevel megawatt power electronics systems—Part I: Characteristics and analysis," *IEEE J. Emerg. Sel. Topics Power Electron.*, vol. 7, no. 1, pp. 7–17, Mar. 2019.
- Z. Zhao, D. Tan, K. Li, and L. Yuan, "Transient behaviors of multilevel megawatt power electronics systems—Part II: Design techniques and practical applications," *IEEE J. Emerg. Sel. Topics Power Electron.*, vol. 7, no. 1, pp. 18–29, Mar. 2019.
- M. R. Ahmed, R. Todd, and A. J. Forsyth, "Predicting SiC MOSFET behavior under hard-switching, soft-switching, and false turn-on conditions," *IEEE Trans. Ind. Electron.*, vol. 64, no. 11, pp. 9001–9011, Nov. 2017.
- B. Shi, Z. Zhao, and Y. Zhu, "Piecewise analytical transient model for power switching device commutation time," *IEEE Trans. Power Electron.*, vol. 34, no. 6, pp. 5720–5736, Jun. 2019.
- J. Wang, H. S.-H. Chung, and R. T.-H. Li, "Characterization and experimental assessment of the effects of parasitic elements on SiC MOSFET switching performance," *IEEE Trans. Power Electron.*, vol. 28, no. 1, pp. 573–589, Jan. 2013.
- S. Saito, A. Costantini, and P. Wheeler, "Experimental study of parasitic inductance influence on SiC MOSFET switching performance in matrix converter," in *Proc. 15th Eur. Conf. Power Electron. Appl. (EPE)*, Lille, France, Sep. 2013, pp. 1–9.
- Z. Chen, D. Boroyevich, and R. Burgos, "Experimental parametric study of the parasitic inductance influence on MOSFET switching characteristics," in *Proc. Int. Power Electron. Conf. (IPEC ASIA)*, Sapporo, Japan, Jun. 2010, pp. 164–169.
- Y. Xiong, S. Sun, H. Jia, P. Shen, and Z. J. Shen, "New physical insights on power MOSFET switching losses," *IEEE Trans. Power Electron.*, vol. 24, no. 2, pp. 525–531, Feb. 2009.
- A. Lemmon, M. Marzouk, J. Gafford, and C. Parker, "Instability in half-bridge circuits switched with wide band-gap transistors," *IEEE Trans. Power Electron.*, vol. 29, no. 5, pp. 2380–2392, May 2014.
- Z. Zhang, F. Wang, L. M. Tolbert, and B. J. Blalock, "Active gate driver for cross-talk suppression of SiC devices in a phase-leg configuration," *IEEE Trans. Power Electron.*, vol. 29, no. 4, pp. 1986–1997, Apr. 2014.
- A. Lewicki, "Dead-time effect compensation based on additional phase current measurements," *IEEE Trans. Ind. Electron.*, vol. 62, no. 7, pp. 4078–4085, Jul. 2015.
- Z. Zhang, H. Lu, D. J. Costinett, F. Wang, L. M. Tolbert, and B. J. Blalock, "Model-based dead time optimization for voltage-source converters utilizing silicon carbide semiconductors," *IEEE Trans. Power Electron.*, vol. 32, no. 11, pp. 8833–8844, Nov. 2017.
- T. Liu, R. Ning, T. Y. Wong, and Z. J. Shen, "Modeling and analysis of SiC MOSFET switching oscillations," *IEEE J. Emerg. Sel. Topics Power Electron.*, vol. 4, no. 3, pp. 747–756, Sep. 2016.
- F. Zhang, D. Jiang, and Y. Zhang, "Study of the characteristics and suppression of EMI of inverter with SiC and Si devices," *Chin. J. Electr. Eng.*, vol. 4, no. 3, pp. 37–46, Sep. 2018.

Tips

不知道大家学会了吗，快去检查一下自己的师兄师姐有没有没发表的成果，按照我的方法试一下，这样你除了引言外，绝大部分内容和图片(以我的这篇文章为例，21个图，只需要自己做一个图，可谓是科研产出的最快途径了。但是，需要提醒大家，为了防止被师兄师姐发现，可以等师兄师姐毕业后，再将相关成果进行发表。还是以我为例，我的师兄2018年毕业，我等到2020年才撰写这篇论文，并且列出他已经不存在的邮箱，以避免让他知道)。此外，大家还可以像我一样将一稿多投(中英互译)，再增加一下成果数量,这样可以再次大大增加论文数量，由于时间有限，我就不一一列举，我就抛砖引玉一篇，大家可以看一下我的[Integral Control](#)英文文章和两篇中文文章[文章1](#)和[文章2](#)中，我将在文章中用别人文章中的图列在下面：

我一作英文期刊论文中的图

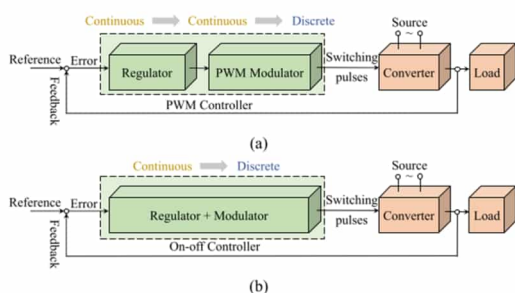


Fig. 10. Two structures of MPE control methods: (a) PWM controller and (b) ON-OFF controller.

其他文章中的图

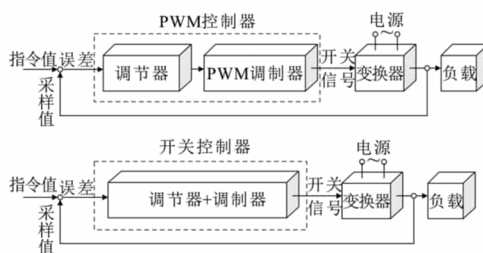


图2 电力电子闭环控制系统的两种基本结构

Fig.2 Two basic structures of power electronic closed-loop control systems

来自[文章1] control systems

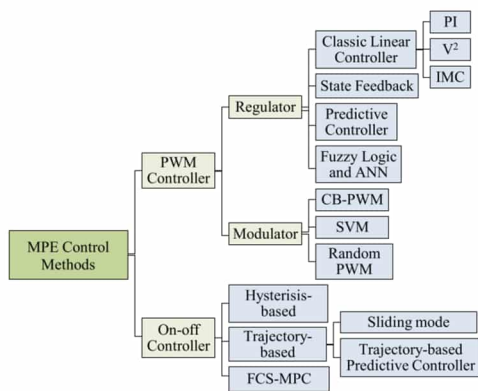


Fig. 11. Classification of MPE control methods according to the two structures [51].

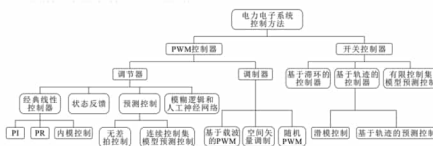


Fig.3 Categories of power electronic control methods

来自[文章1]

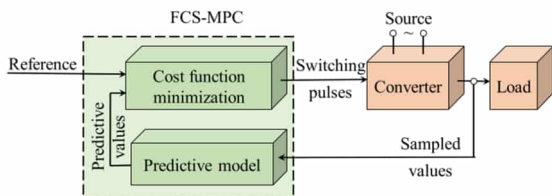


Fig. 12. Diagram of FCS-MPC [43].

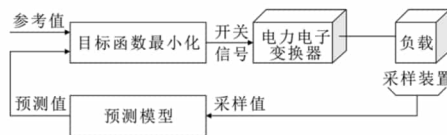
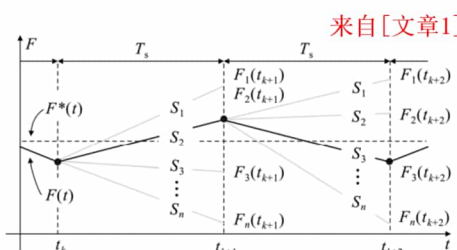
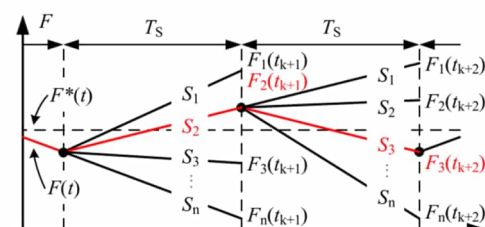


图7 FCS-MPC 预测控制原理图

Fig.7 Diagram of FCS-MPC

来自[文章1]



来自[文章1]

Fig. 13. Switching combination optimization in FCS-MPC [43].

图8 预测控制优化开关组合流程图
Fig.8 Switching combination optimization in FCS-MPC

TABLE III
COMPARISON OF PWM AND ON-OFF CONTROLLER

	PWM controller	On-off controller
The controlled process	Continuous (large-scale) -- discrete	Continuous (large-scale) -- discrete
Regulator	Continuous controller, such as PI	Regulator and modulator are integrated, such as hysteresis controller
Modulator	PWM controller, such as carrier-based PWM	
Dynamic response	Slower	Faster
Switching frequency	Typically fixed	Typically variable

来自[文章1]

Table 1 Comparisons between large time-scale control methods

参数	PWM 控制	开关控制
控制过程	连续(大时间尺度)—离散	连续(大时间尺度)—离散
调节器	连续控制调节器, 如 PI	集成一体, 如滞环比较器
调制器	PWM 调制器, 如载波 PWM	
特点	具有大局观, 动态过程平稳	控制更简单, 响应速度更快

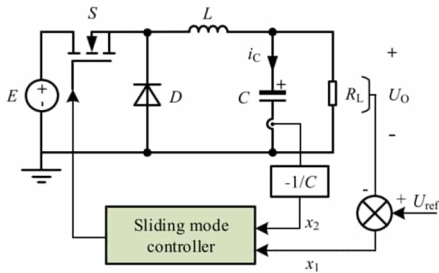
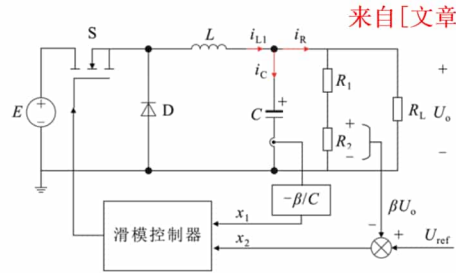


Fig. 14. Buck circuit with SM controller [55].



来自[文章1]

图9 滑模控制 Buck 变换器电路图

Fig.9 A buck circuit with SM controller

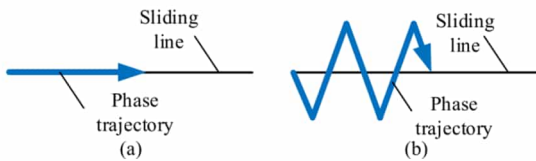
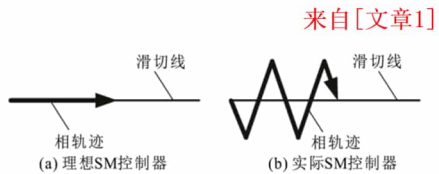


Fig. 15. State trajectory with (a) ideal and (b) practical SM controller [55].



来自[文章1]

图10 系统状态轨迹

Fig.10 State trajectory with ideal and practical SM controller

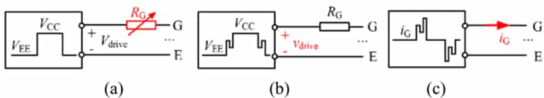


Fig. 16. Diagram of an AGD (G: gate terminal and E: emitter terminal). (a) Adjustable gate resistance. (b) Adjustable drive voltage. (c) Adjustable drive current.

来自[文章2]

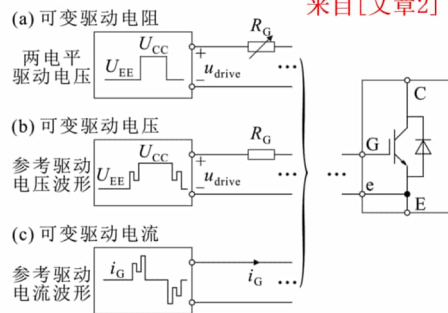


图2 主动栅极驱动电路示意图

Fig.2 Diagram of an AGD

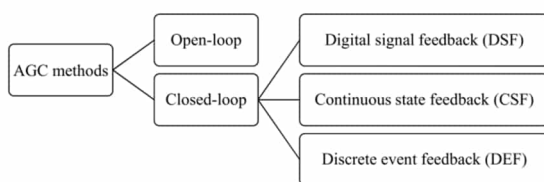


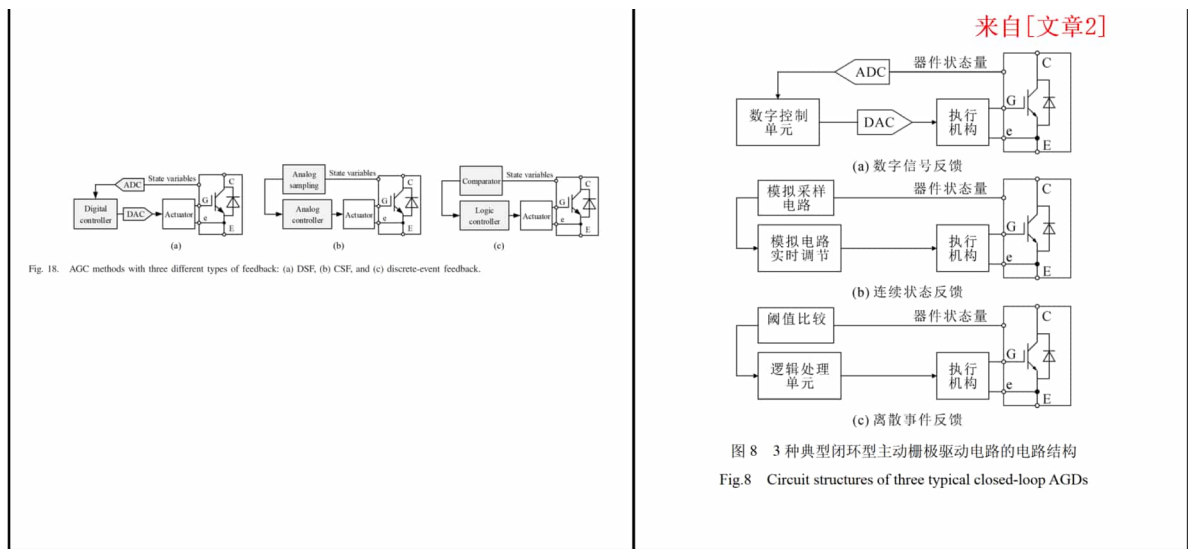
Fig. 17. Classification of AGC methods.



图3 常见栅极驱动主动控制方法分类

Fig.3 Classification of AGC methods

来自[文章2]



全文共29图。其中从图10到18及相关内容均从中文文章翻译，中英互译比例接近 33.3%

小结

综上我在这篇文章中存在以下问题：

在[清华大学预防与处理学术不端行为办法](#)中：

*第二十二条 在科学研究及相关活动中有下列行为之一的，应当**认定为构成学术不端行为**：

(一) 剽窃、抄袭、**侵占他人学术成果**；

(二) **篡改他人研究成果**；

(四) **未参加研究或创作而在研究成果、学术论文上署名，未经他人许可而不当使用他人署名，虚构合作者共同署名，或者多人共同完成研究而在成果中未注明他人工作、贡献**；

总结

总的来说，我一共有八篇一作SCI论文，其中5篇的实验结果使用了篡改数据，2篇直接抄袭，翻译别人的论文。轻轻松松获得如此丰硕的成果，让我能够包揽从学术新秀，特等奖学金到青拔人才的所有奖项，而老老实实的你，又拿什么来和我比呢？

通过以上讲解，我相信大家一定受益匪浅。目前中国国内学术风气确实不太好，所以像我这样对学术没有敬畏之心的人才能如鱼得水，急功近利，**伪造科研数据**，将他人的研究成果改头换面据为己有，甚至直接是拿来主义，我认为这种行为是完全没问题的。大部分人可能难以接受我的观点，所以你们只能在科研圈的最底层挣扎，无法像我一样年少有为。尽管在我的行径，不仅无法推进学术发展，还会促使学术氛围的进一步恶化。但这和我有什么关系呢？

我奉劝大家像我学习，一起学术不端起来，多拿成果，多拿帽子，成为人上人。你们一定会回来感谢我的。

至于其他人，就让他们在阴沟里面继续挣扎吧，即使你们像**郭宏业**、**蒯晨晖**他们一样优秀，也只能拿到助理研究员这种程度。更何况你们大部分人还达不到人家的水平。如果你对我的做法感到不满，欢迎你来举报投诉我。可能的处理结果包括：

1. 第二十四条 学校根据校学术委员会学风组或者校学术委员会主任会议的认定结论，结合行为性质和情节轻重，对学术不端行为责任人进行处理：

(一) 通报批评；

(二) **终止或者撤销相关的科研项目**，并在一定期限内取消申请资格；

(三) **撤销相关学术奖励或者荣誉称号**；

(四) **辞退或解聘**；

(五) 法律、法规及规章规定的其他处理措施。

学术不端行为责任人**获得有关部门、机构设立的相关科研项目、学术奖励或者荣誉称号等利益的**，学校根据关联情况向相关主管部门提出处理建议。

学生有学术不端行为的，**按照学生管理的相关规定给予相应的学籍处分**。

学术不端行为**与获得学位有直接关联的**，由学位授予单位作暂缓授予学位、不授予学位或者**依法撤销学位**等处理。

但是我可以负责的告诉你，这肯定没用，不信就试试看！我把举报投诉方式列在下面供你们使用：

- 清华大学学术委员会秘书处联系方式 地址：清华大学东门外华业大厦1216 电话：010-62782295
- 清华大学党委办公室（校长办公室）联系电话：010-62782015/2035 电子邮箱：zzbs@tsinghua.edu.cn
- 清华大学人事处——博士后办公室 联系人：韩老师 电子邮箱：qhbs@tsinghua.edu.cn
- 清华大学电机系 党委书记：于歆杰 电子邮箱：yuxj@tsinghua.edu.cn
- 清华大学电机系 系主任：康重庆 电子邮箱：cqkang@tsinghua.edu.cn
- 清华大学人事处处长 杨殿阁 E-mail:ydg@mail.tsinghua.edu.cn
- 清华大学校长 李路明 E-mail:lilm@tsinghua.edu.cn; Tel: 86-10-62785716
- 清华大学党委书记：邱勇 qiuy@mail.tsinghua.edu.cn
- 清华大学纪检监察机构 jjw@tsinghua.edu.cn
- 清华大学党委研究生工作部：yjsygz@tsinghua.edu.cn
- 清华大学党委教师工作部：dwjsgz@mail.tsinghua.edu.cn
- 清华大学科技处 kjc-jdb@tsinghua.edu.cn
- 清华大学学术委员会秘书处联系方式：电话：010-62782295 邮箱：xswbgs@tsinghua.edu.cn
- 清华大学学位委员会联系方式：电话：010-62783183 邮箱：yjsyxwb@tsinghua.edu.cn
- 中国自然科学基金委举报网站：<https://jdwyh.nsf.gov.cn>
- 中共组织部青拔人才帽子举报网站：<http://www.12380.gov.cn>

在线链接

电子版可通过<https://github.com/ShiArthur03> 来访问，也欢迎大家在[讨论区](#)和我互动。

pdf下载链接：[链接](#)

再次强调

如果有谁拿上面的材料来举报我，那我不会承认这些材料是我写的，我会说这些都是别人恶意捏造，来抹黑我。有种放马过来！